International Journal of Aerospace Engineering

Recent Advances in the Application of Advanced Algorithms in Computational Fluid Dynamics Technology

Lead Guest Editor: Feng Qu
Guest Editors: Chao Yan, Shahid Mughal, and Di Sun

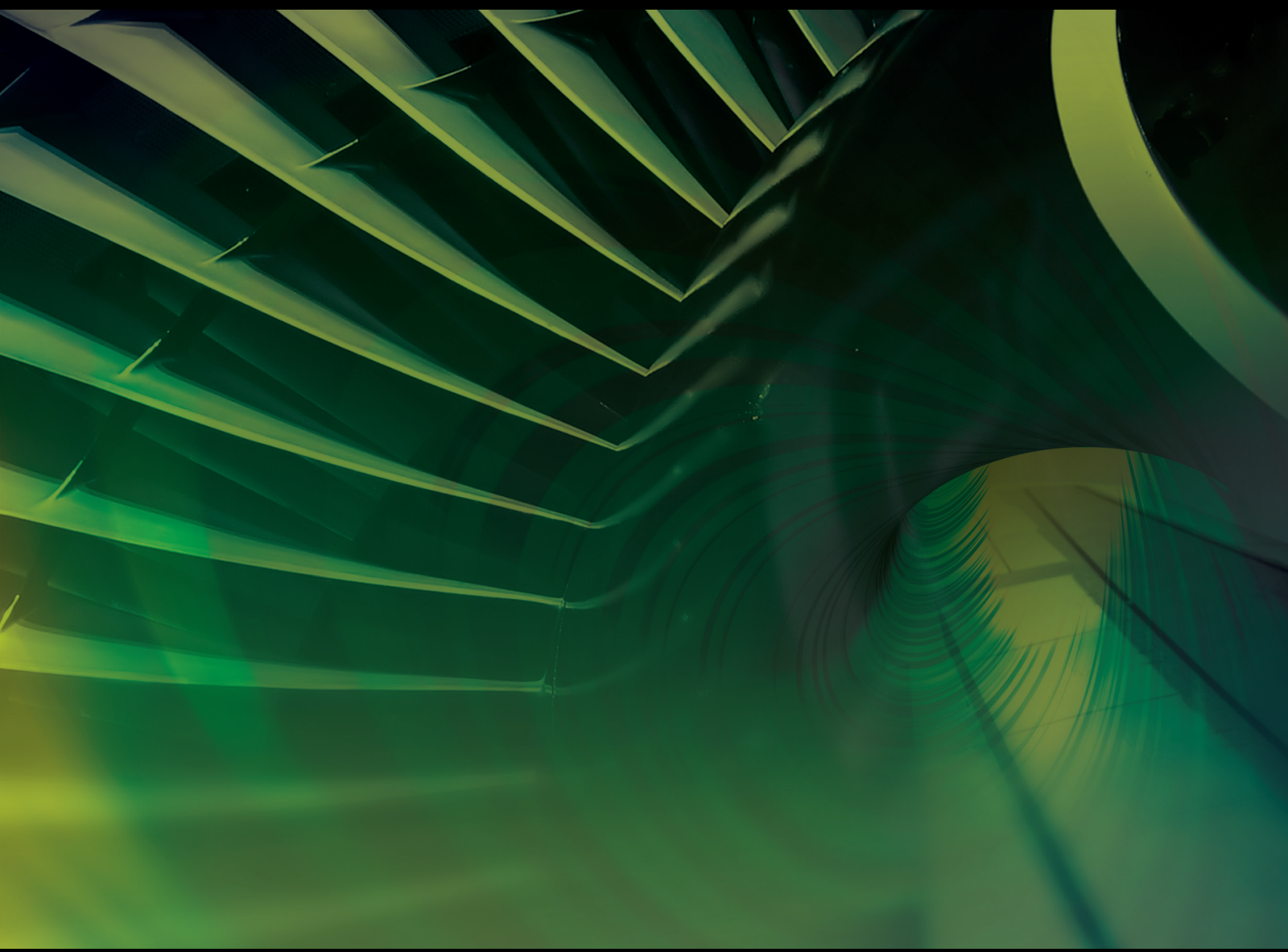

Recent Advances in the Application of Advanced Algorithms in Computational Fluid Dynamics Technology

International Journal of Aerospace Engineering

Recent Advances in the Application of Advanced Algorithms in Computational Fluid Dynamics Technology

Lead Guest Editor: Feng Qu
Guest Editors: Chao Yan, Shahid Mughal, and Di Sun

Contents

Hindawi
International Journal of Aerospace Engineering
Volume 2020, Article ID 8825445, 13 pages
https://doi.org/10.1155/2020/8825445

Research Article

High-Order Hybrid WCNS-CPR Scheme for Shock Capturing of Conservation Laws

Jia Guo,[1,2] Huajun Zhu,[2] Zhen-Guo Yan,[2] Lingyan Tang,[1] and Songhe Song[1]

[1]*College of Liberal Arts and Sciences, National University of Defense Technology, Changsha, Hunan 410073, China*
[2]*State Key Laboratory of Aerodynamics, China Aerodynamics Research and Development Center, Mianyang, Sichuan 621000, China*

Correspondence should be addressed to Zhen-Guo Yan; zgyan@skla.cardc.cn

Received 23 July 2020; Revised 1 September 2020; Accepted 16 September 2020; Published 14 October 2020

Academic Editor: Feng Qu

By introducing hybrid technique into high-order CPR (correction procedure via reconstruction) scheme, a novel hybrid WCNS-CPR scheme is developed for efficient supersonic simulations. Firstly, a shock detector based on nonlinear weights is used to identify grid cells with high gradients or discontinuities throughout the whole flow field. Then, WCNS (weighted compact nonlinear scheme) is adopted to capture shocks in these areas, while the smooth area is calculated by CPR. A strategy to treat the interfaces of the two schemes is developed, which maintains high-order accuracy. Convergent order of accuracy and shock-capturing ability are tested in several numerical experiments; the results of which show that this hybrid scheme achieves expected high-order accuracy and high resolution, is robust in shock capturing, and has less computational cost compared to the WCNS.

1. Introduction

In computational fluid dynamics (CFD), numerical schemes greatly influence the computational accuracy, efficiency, and robustness. Despite the extra complexity of high-order schemes [1], they can provide more accurate results in delicate simulations compared with traditional second-order schemes. With the increasing demand for delicate simulations, such as large-eddy simulation (LES) of turbulent flows, computational aeroacoustics (CAA), and shock-induced separation flows, high-order schemes have attracted remarkable research attentions in recent years [1–6].

Among these high-order schemes, the CPR scheme has several good properties. It is compact, efficient, and applicable to complex unstructured meshes [1, 6, 7]. It was firstly proposed by Huynh [8] and was generalized to unstructured meshes by Wang and Gao [9], which is now widely applied in scientific researches and engineering predictions [6, 10–12]. With specific correction functions, the CPR methods are equivalent to specific discontinuous Galerkin (DG) methods, while their calculation cost is relatively lower because they are based on a differential formulation and avoid expensive integration calculations [8].

However, the shock-capturing techniques of high-order finite element methods, including CPR and DG methods, still can not meet the need of many simulations [1, 13]. Shu et al. [14] employed a WENO nonlinear limiter on the CPR scheme, which can maintain high-order accuracy in smooth regions and control spurious numerical oscillations near discontinuities. A parameter-free gradient-based limiter for the CPR scheme on mixed unstructured meshes was developed by Lu et al. [15]. By proposing a p-weighted procedure, new smoothness indicators are developed in the DG methods, which obviously improve the shock-capturing ability [16]. However, obvious oscillations can still be observed near discontinuities. Artificial viscosity methods with subcell shock capturing and cross cell smoothness have been proposed for shock capturing [17, 18]. However, they are dependent on some user-defined parameters. Great progress has been made; however, the compact polynomial

approximations of solutions in a high-order finite element cell are by design not a good approximation of discontinuities, which easily leads to spurious numerical oscillations near discontinuities.

A way around this problem is to develop a hybrid scheme of high-order finite element methods (CPR or DG) and finite difference (FD) or finite volume (FV) methods, which provide better shock-capturing abilities locally near shocks. In this way, high-order finite element methods are adopted in smooth regions, which maintain compactness and high resolution. Meanwhile, FD or FV schemes are adopted to provide robust shock-capturing abilities. Dumbser et al. [19] developed hybrid DG-FV methods and utilized second-order FV to capture shocks. Cheng et al. developed multidomain hybrid RKDG and WENO methods [20, 21] with good geometry flexibility and low computational costs. These methods show good shock-capturing ability because they avoid using high-order finite element methods to capture shocks directly, but utilize schemes with better shock-capturing abilities instead.

A hybrid shock-capturing scheme is developed based on the zonal hybrid WCNS-CPR scheme proposed in [7]. In [7], some fundamental problems of the WCNS-CPR schemes, such as spatial accuracy and geometric conservation laws, have been studied, which makes the scheme efficient and applicable to complex curved meshes. In this paper, a shock detector and a nonlinear weighted interpolation are introduced to the hybrid WCNS-CPR scheme for simulating problems with discontinuities. The nonlinear weighted approach of WCNS is introduced to the hybrid scheme for both the shock detection and the shock capturing. Considering the robust shock-capturing ability of WCNS, we intend to develop a hybrid shock-capturing scheme to combine merits of two schemes. Different from the zonal hybrid strategy in [7], the two schemes are switched dynamically based on the smoothness of the local flow field. The main contributions of this paper are as follows:

(1) Nonlinear mechanisms, including shock detection and shock capturing, are introduced into the hybrid scheme and a hybrid scheme with good shock-capturing ability is a developed

(2) A hybrid WCNS-CPR scheme with dynamical switching strategy between the two schemes is proposed, in which the strategy of dynamical scheme switching and interface treatment methods are addressed

(3) Numerical experiments are conducted to show the good properties in accuracy, efficiency, and shock-capturing ability of the hybrid WCNS-CPR scheme.

The rest of this paper is organized as follows. In Section 2, high-order WCNS and CPR schemes are briefly reviewed. The hybrid WCNS-CPR scheme is constructed in Section 3, where the interface treatments are discussed in detail. Section 4 presents several numerical tests to show the performance of the proposed hybrid method. Finally, concluding remarks are given in Section 5.

2. Brief Review of WCNS and CPR

In this section, a brief review of WCNS and CPR is presented based on two-dimensional hyperbolic conservation laws

$$U_t + F(U)_x + G(U)_y = 0, \tag{1}$$

where U is a conservative variable vector and F and G are the flux vectors.

2.1. Brief Review of Third-Order WCNS. Equation (1) is discretized by a finite difference scheme at every node (x_i, y_j)

$$(U_t)_{i,j} = E'_{i,j} = -(F_x)_{i,j} - (G_y)_{i,j}, \tag{2}$$

where $E'_{i,j}$ is the approximation of the spatial derivatives. The following fourth-order flux difference operators are used

$$\begin{aligned}(F_x)_{i,j} &= \frac{4}{3h}\left(\widehat{F}_{i+1/2,j} - \widehat{F}_{i-1/2,j}\right) - \frac{1}{6h}\left(F_{i+1,j} - F_{i-1,j}\right),\\ (G_y)_{i,j} &= \frac{4}{3h}\left(\widehat{G}_{i,j+1/2} - \widehat{G}_{i,j-1/2}\right) - \frac{1}{6h}\left(G_{i,j+1} - G_{i,j-1}\right),\end{aligned} \tag{3}$$

where h is the grid spacing. Here, $\widehat{F}_{i-1/2,j} = \widehat{F}_{i-1/2}(U^L_{i-1/2,j}, U^R_{i-1/2,j})$, $\widehat{G}_{i,j-1/2} = \widehat{G}_{j-1/2}(U^L_{i,j-1/2}, U^R_{i,j-1/2})$ are the Riemann fluxes at cell edges, as shown in Figure 1. Riemann solvers can be used to compute numerical fluxes, such as Lax Friedrichs, Roe, Osher, AUSM, HLL, and their modifications. We refer to papers [3, 4, 22] and references therein.

To capture discontinuities, the conservative variables at cell edges $U^R_{i-(1/2),j}$ are obtained by the weighted nonlinear interpolation proposed in [23]. The third-order WCNS interpolation has the following steps:

Step 1. Divide the third-order three-point stencil $S_i = \{U_{i-1,j}, U_{i,j}, U_{i+1,j}\}$ into two smaller substencils $S_i^{(1)} = \{U_{i-1,j}, U_{i,j}\}$ and $S_i^{(2)} = \{U_{i,j}, U_{i+1,j}\}$.

Step 2. Construct an interpolation polynomial $p^{(m)}(x)$ in each substencil $S_i^{(m)}$, $m = 1, 2$, which satisfies $p^{(m)}(x_i) = U_{i,j}$. We have

$$\begin{aligned}p^{(1)}\left(x_{i-(1/2)}\right) &= \frac{1}{2}U_{i-1,j} + \frac{1}{2}U_{i,j},\\ p^{(2)}\left(x_{i-(1/2)}\right) &= \frac{3}{2}U_{i,j} - \frac{1}{2}U_{i+1,j}.\end{aligned} \tag{4}$$

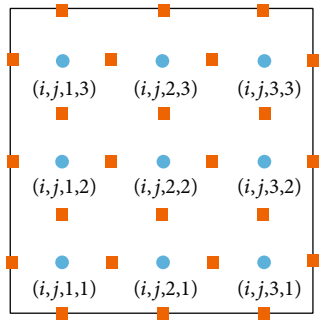

Figure 1: Distribution of solution points and flux points of 2D WCNS in (i, j)-th cell. Solution points are marked in blue dot and flux points in orange square.

Step 3. Calculate the nonlinear weights ω_k based on linear weights d_m and a smoothness indicator IS_k for each substencil $S_i^{(m)}$, $m = 1, 2$. The linear weights are

$$d_1 = \frac{3}{4}, \quad d_2 = \frac{1}{4}. \tag{5}$$

The improved Z-type nonlinear weights [24, 25] are defined by

$$\omega_k = \frac{\beta_k}{\sum_{m=1}^{2} \beta_m}, \tag{6}$$

$$\beta_k = d_k \left[C_q + \left(\frac{\tau_5}{\varepsilon + IS_k} \right)^{p_z} \right], \tag{7}$$

$$k = 1, 2, \tag{8}$$

where $\varepsilon = 10^{-6}$ is a small number, IS_k is a smoothness indicator, $\tau_5 = |IS_0 - IS_1|$, and C_q and p_z are parameters. We use $p_z = 2$ and $C_q = 4$ to improve the performance of the nonlinear weights.

An improved smoothness indicator [25] is employed.

$$IS_0 = \frac{1}{4}\left(3U_{i,j} - 4U_{i-1,j} + U_{i-2,j}\right)^2 + \left(U_{i,j} - 2U_{i-1,j} + U_{i-2,j}\right)^2,$$

$$IS_1 = \frac{1}{4}\left(3U_{i+2,j} - 4U_{i+1,j} + 3U_{i,j}\right)^2 + \left(U_{i+2,j} - 2U_{i+1,j} + U_{i,j}\right)^2. \tag{9}$$

Step 4. Get weighted interpolation value at $x_{i-(1/2)}$.

$$U^R_{i-(1/2),j} = \sum_{m=1}^{2} \omega_m p^{(m)}\left(x_{i-(1/2)}\right). \tag{10}$$

The formulations of $U^L_{i-(1/2),j}$ is symmetric with $U^R_{i-(1/2),j}$ by i.

2.2. Review of Third-Order CPR. For the third-order CPR framework, there are 3^2 solution points (i, j, l, m), $l = 1, 2, 3$, $m = 1, 2, 3$, in the (i, j)-th cell, as shown in Figure 2. The nodal values of the conservative variable U at solution points are updated by the following differential equation

$$\frac{\partial U_{i,j}}{\partial t} + \frac{\partial \tilde{F}_{i,j}(\xi,\eta)}{\partial \xi} + \frac{\partial \tilde{G}_{i,j}(\xi,\eta)}{\partial \eta} = 0, \ (\xi,\eta) \in [-1,1] \times [-1,1]. \tag{11}$$

The reconstructed flux $\tilde{F}_{i,j}(\xi,\eta)$ and $\tilde{G}_{i,j}(\xi,\eta)$ are expressed as

$$\tilde{F}_{i,j}(\xi,\eta) = F_{i,j}(\xi,\eta) + \sigma^1_{i,j}(\xi,\eta),$$
$$\tilde{G}_{i,j}(\xi,\eta) = G_{i,j}(\xi,\eta) + \sigma^2_{i,j}(\xi,\eta), \tag{12}$$

where $\sigma^1_{i,j}(\xi,\eta)$ and $\sigma^2_{i,j}(\xi,\eta)$ are flux correction polynomials

$$\sigma^1_{i,j}(\xi_l,\eta_m) = \left[\hat{F}(-1,\eta_m) - F_{i,j}(-1,\eta_m)\right] g_L(\xi_l) + \left[\hat{F}(1,\eta_m) - F_{i,j}(1,\eta_m)\right] g_R(\xi_l),$$
$$\sigma^2_{i,j}(\xi_l,\eta_m) = \left[\hat{G}(\xi_l,-1) - G_{i,j}(\xi_l,-1)\right] g_L(\eta_m) + \left[\hat{G}(\xi_l,1) - G_{i,j}(\xi_l,1)\right] g_R(\eta_m). \tag{13}$$

Here, correction functions $g_L(\xi)$, $g_R(\xi)$, $g_L(\eta)$, and $g_R(\eta)$ are all cubic polynomials, and $\hat{F}$ and $\hat{G}$ are Riemann fluxes corresponding to F and G, respectively.

$$\hat{F}(-1,\eta) = \hat{F}\left(U_{i-1,j}(1,\eta), U_{i,j}(-1,\eta)\right),$$
$$\hat{F}(1,\eta) = \hat{F}\left(U_{i,j}(1,\eta), U_{i+1,j}(-1,\eta)\right). \tag{14}$$

Moreover, the solution polynomial is

$$U_{i,j}(\xi,\eta) = \sum_{l=1}^{3}\sum_{m=1}^{3} U_{i,j,l,m} L_l(\xi) L_m(\eta) \tag{15}$$

where $L_l(\xi)$ and $L_m(\eta)$ are the 1D Lagrange polynomials in the ξ and η directions.

The flux polynomial is

$$F_{i,j}(\xi,\eta) = \sum_{l=1}^{3}\sum_{m=1}^{3} F_{i,j,l,m} L_l(\xi) \cdot L_m(\eta), \ G_{i,j}(\xi,\eta) = \sum_{l=1}^{3}\sum_{m=1}^{3} G_{i,j,l,m} L_l(\xi) \cdot L_m(\eta). \tag{16}$$

Remark 1. In this paper, solution points are the Gauss points, which are positioned at $\xi_1 = -\sqrt{15}/5, \xi_2 = 0, \xi_3 = \sqrt{15}/5$ for $K = 3$. Correction function for g_{DG} scheme is used, which is expressed as $g_{DG,L} = (-1)^k/2(L_K - L_{K-1})$, $g_{DG,R} = (1/2)(L_K +$

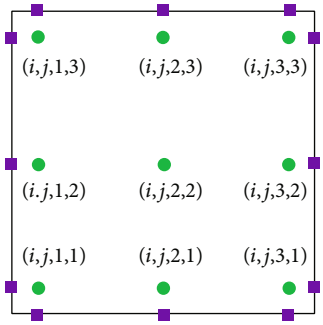

Figure 2: Distribution of solution points and flux points of 2D CPR in (i, j)-th cell. Solution points are marked in green dot and flux points on element boundary in purple square. The flux points inside the CPR cell coincide with the solution points.

L_{K-1}), where L_K is Legendre polynomials. More specifically, $L_3(\xi) = (1/2)(5\xi^3 - 3\xi)$ and $L_2(\xi) = (1/2)(3\xi^2 - 1)$.

3. Hybrid Schemes Based on WCNS and CPR

3.1. Strategy of Scheme Switching. The hybrid scheme adopts the nonlinear WCNS with shock-capturing ability in non-smooth regions and the CPR scheme with high computational efficiency in smooth regions. Thus, a shock detector is needed to judge the location of shocks. Recently, many shock detectors with good properties have been developed [26–28]. In this paper, we use the NI (nonlinear indicator) [28] to detect which cells probably contain shocks and then mark them as troubled cells. The formula of the NI shock detector is as follows:

$$\mathrm{NI} = \frac{1}{(r(r+1))^{1/2}} \left[\sum_{k=0}^{r} \left(\frac{[1/(r+1)] - [(\omega_k/d_k)/\sum_{k=0}^{r}(\omega_k/d_k)]}{[1/(r+1)]} \right)^2 \right]^{1/2}, \tag{17}$$

where $r+1$ represents the number of candidate stencils in WCNS with $r = 1$ for the third-order WCNS. To maintain that discontinuities do not move out of the troubled cells during the time integration, buffer cells are introduced around the troubled cells, which are also calculated using WCNS. As shown in Figure 3, the direct neighbors of troubled cells are defined as buffer cells, and other cells are called smooth cells.

Above all, the strategy of scheme switching is as follows. When the NI shock detector detects shocks, in the cells near shocks (namely, in troubled cells and buffer cells), CPR scheme is switched to WCNS. And when shocks leave the cells, these cells are calculated by the CPR scheme again. That is to say, the shock detector judges three types of cells, and we use WCNS in troubled cells and buffer cells and the CPR scheme in other cells.

3.2. Interface Treatment. The interface treatment influences the accuracy and stability of the overall scheme and should be discussed carefully. The main difficulty is at the WCNS-CPR interface. We denote the solution points of the CPR scheme by c and the solution points of WCNS by w.

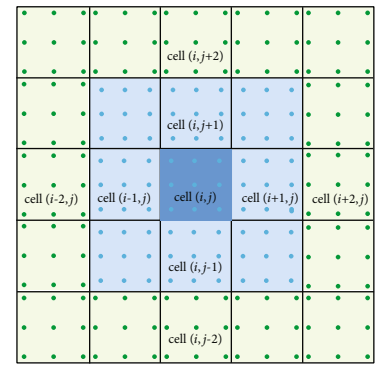

Figure 3: Three different types of cells. Troubled cells are marked in dark blue; buffer cells are in light blue; and smooth cells are in green.

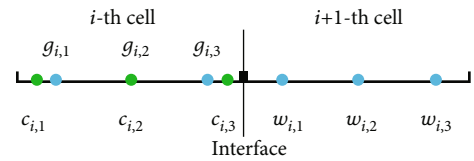

Figure 4: 1D grid, different solution points and ghost points.

3.2.1. 1D Interface Treatment. First, WCNS in the $i+1$-th cell needs information of ghost points $\{g_{i,k}, k = 1, 2, 3\}$ from the neighboring i-th CPR cell, as shown in Figure 4. The solution values of ghost points of WCNS cell are calculated via CPR interpolation using data at $\{c_{i,k}, k = 1, 2, 3\}$. That is,

$$u(g_{i,k}) = \sum_{k=1}^{3} u(c_{i,k}) L_k. \tag{18}$$

Second, we apply $u^{-(\mathrm{CPR})}_{i+(1/2),\mathrm{interface}}$ provided by i-th CPR cell and $u^{+(\mathrm{WCNS})}_{i+(1/2),\mathrm{interface}}$ computed in $i+1$-th WCNS cell with the values of ghost points to calculate the numerical fluxes at interface:

$$\widehat{f}_{i+(1/2),\mathrm{interface}} = f\left(u^{-(\mathrm{CPR})}_{i+(1/2),\mathrm{interface}}, u^{+(\mathrm{WCNS})}_{i+(1/2),\mathrm{interface}}\right). \tag{19}$$

In addition, information exchange of switching strategy at different moments should also be considered. When i-th cell is a smooth cell at the n-th time step and it is judged as a buffer cell or a troubled cell in the next time step, information of solution points of WCNS can be obtained by Lagrange interpolation via information of CPR. Now, we consider the opposite situation: the cell is a buffer cell or a troubled cell at n-th time step and it is switched to a smooth cell at the next time step, information should be transmitted from WCNS to CPR. The procedure involves nonlinear interpolation cross cells. We take the $(i, 1)$-th solution point as an example.

Step 1. Divide the stencil $S = \{w_{i-1,3}, w_{i,1}, w_{i,2}\}$ into two sub-stencils $S_1 = \{w_{i-1,3}, w_{i,1}\}$, $S_2 = \{w_{i,1}, w_{i,2}\}$.

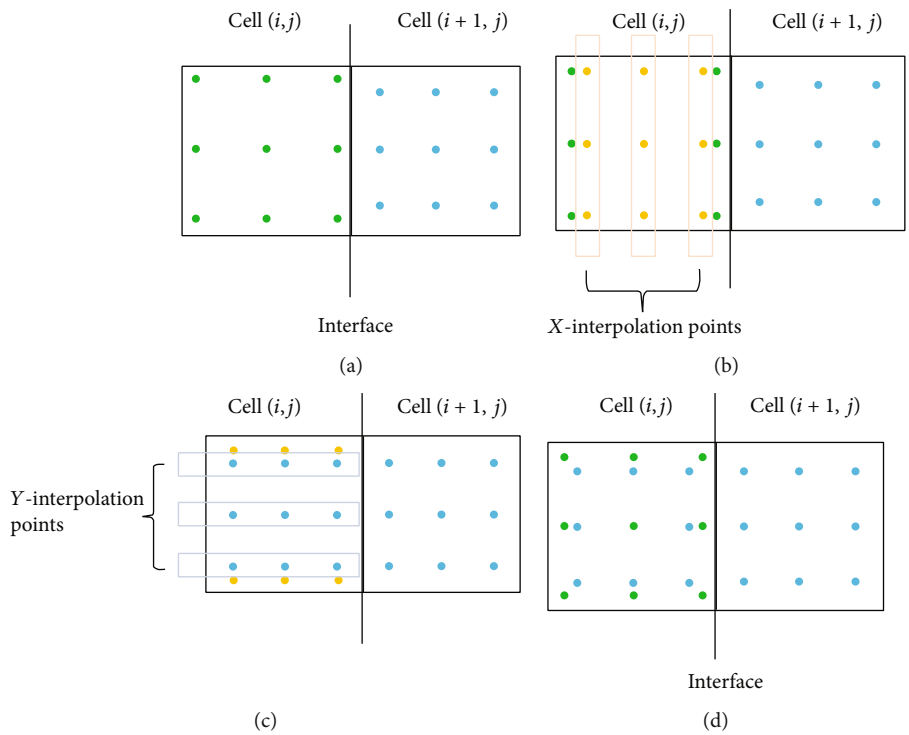

FIGURE 5: 2D different points near the interface of hybrid scheme. (a) 2D grid and different solution points. (b) 2D x direction interpolation. (c) 2D y direction interpolation. (d) 2D ghost points.

Step 2. Construct interpolation polynomials $u_1(c_{i,1})$ and $u_2(c_{i,1})$ in S_1 and S_2, respectively, we have

$$u_1(c_{i,1}) = u(w_{i-1,3})l_1(c_{i,1}) + u(w_{i,1})l_2(c_{i,1}),$$
$$u_2(c_{i,1}) = u(w_{i,1})l_1(c_{i,1}) + u(w_{i,2})l_2(c_{i,1}), \tag{20}$$

where l_1 and l_2 are linear Lagrange polynomials.

Step 3. Calculate the nonlinear weights based on linear weights d_1 and d_2. The linear weights can be obtained by solving the following equations:

$$d_1u_1(c_{i,1}) + d_2u_2(c_{i,1}) = u(w_{i-1,3})L_1(c_{i,1}) + u(w_{i,1})L_2(c_{i,1}) + u(w_{i,2})L_3(c_{i,1}). \tag{21}$$

Then, nonlinear weights can be calculated by equation (6).

Step 4. Get the interpolation value $u(c_{i,1}) = \omega_1u_1(c_{i,1}) + \omega_2u_2(c_{i,1})$.

3.2.2. 2D Interface Treatment. In this subsection, we consider the interface treatment between (i,j)-th CPR cell and $(i+1,j)$-th WCNS cell in 2D computational domain in Figure 5(a).

Similarly, WCNS needs information of ghost points $\{g_{i,j,i_0,j_0}, i_0 = 1,2,3; j_0 = 1,2,3\}$ from the (i,j)-th CPR cell. The solution values at ghost points of WCNS in the CPR cell

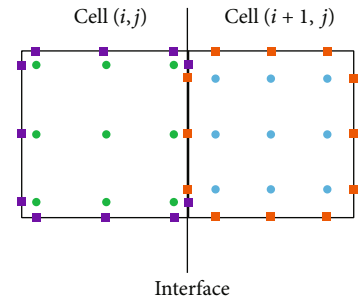

FIGURE 6: Distribution of different flux points on cell interfaces. Flux points of CPR are marked in purple square and those of WCNS in orange square.

are calculated via CPR interpolation using data at $\{(c_{i,j,i_0,j_0}), i_0 = 1,2,3; j_0 = 1,2,3\}$. Using dimension by dimension interpolation strategy, we do the Lagrange interpolation in the x direction first, as shown in Figure 5(b), and then in the y direction, as shown in Figure 5(c). Using solution polynomial equation (15) of CPR, we have

$$u\left(g_{i,j,i_1,j_1}\right) = \sum_{i_0=1}^{3}\sum_{j_0=1}^{3} u\left(c_{i,j,i_0,j_0}\right)L_{i_0}(\xi_m)L_{j_0}(\eta_m), \tag{22}$$

at the ghost points $\{g_{i,j,i_1,j_1}, i_1 = 1,2,3; j_1 = 1,2,3\}$.

Then, we calculate the numerical fluxes at cell interface. As shown in Figure 6, two types of flux points, fp_k^{WCNS} and fp_k^{CPR}, do not coincide with each other. Thus, $u^-_{fp_k^{\mathrm{WCNS}}}$ and $u^+_{fp_k^{\mathrm{CPR}}}$ need to be interpolated before calculating numerical

Table 1: Test of single schemes and hybrid WCNS-CPR scheme in $[-6, 6]$ for 1D linear equation.

Norm	DOFs	WCNS		CPR		Hybrid WCNS-CPR	
		Error	Order	Error	Order	Error	Order
L_∞	120	$3.00E-4$	—	$1.28E-4$	—	$3.00E-4$	—
	240	$3.76E-5$	3.00	$1.61E-5$	2.99	$3.40E-5$	3.14
	480	$4.70E-6$	3.00	$2.02E-6$	2.99	$2.02E-6$	4.07
L_2	120	$2.12E-4$	—	$7.99E-5$	—	$2.07E-4$	—
	240	$2.66E-5$	2.99	$9.96E-6$	3.00	$1.60E-5$	3.69
	480	$3.32E-6$	3.00	$1.24E-6$	3.01	$1.24E-6$	3.69

fluxes. $u^-_{fp_k^{\mathrm{WCNS}}}$ is obtained by CPR linear interpolation using equation (15) based on values in (i, j)-th cell, while $u^+_{fp_k^{\mathrm{CPR}}}$ is obtained through WCNS nonlinear interpolation dimension by dimension. The interpolated values of $u^-_{fp_k^{\mathrm{WCNS}}}$ and $u^+_{fp_k^{\mathrm{CPR}}}$ are denoted by $u^{-(\mathrm{CPR,interp})}_{fp_k^{\mathrm{WCNS}}}$ and $u^{+(\mathrm{WCNS,interp})}_{fp_k^{\mathrm{CPR}}}$ correspondingly.

Therefore, for the CPR scheme, the numerical flux at fp_k^{CPR} is

$$\widehat{f}_{fp_k^{\mathrm{CPR}}} = f\left(u^-_{fp_k^{\mathrm{CPR}}}, u^{+(\mathrm{WCNS,interp})}_{fp_k^{\mathrm{CPR}}}\right). \tag{23}$$

Meanwhile, the numerical flux at fp_k^{WCNS} for WCNS is

$$\widehat{f}_{fp_k^{\mathrm{WCNS}}} = f\left(u^{-(\mathrm{CPR,interp})}_{fp_k^{\mathrm{WCNS}}}, u^+_{fp_k^{\mathrm{WCNS}}}\right). \tag{24}$$

The 2D information exchange of switching strategy at different moments is similar with the 1D situation. The Nonlinear interpolation is used from information in WCNS to CPR, while the linear interpolation from CPR to WCNS. They are not presented here for clarity.

4. Numerical Investigation

In this section, we will test spatial accuracy, shock-capturing performance, and computational efficiency of the hybrid WCNS-CPR scheme. Comparisons with the WCNS are also investigated. We firstly take 1D linear wave equation to compare numerical errors of single and the hybrid scheme. 1D shock-tube problems are solved to demonstrate the shock-capturing ability of the hybrid scheme. Then, 2D isentropic vortex problem in Euler equation systems is solved for testing spatial accuracy and computational efficiency of WCNS and CPR. At last, 2D Riemann problem and double Mach reflection problem are simulated to test the shock-capturing performance of the hybrid scheme and comparison of computational efficiency is conducted in the double Mach reflection problem. In this paper, Riemann fluxes are computed by the Lax Friedrichs solver. The explicit third-order TVD Runge-Kutta scheme is used for time integration.

The L_∞ error and L_2 error are computed to measure local solution quality and global solution quality, respectively. The L_2 error is estimated by

$$\mathrm{Error}_{L_2} = \sqrt{\frac{\sum_{i=1}^{N}\left(U_i^h - U(r_i)\right)^2}{N}}, \tag{25}$$

where U_i^h and $U(r_i)$ are the numerical solution and the exact solution at the i-th solution point. Here, N is the total number of solution points.

4.1. 1D Linear Wave Equation. Consider the 1D linear wave equation

$$u_t + u_x = 0, \tag{26}$$

with the initial condition

$$u(x, 0) = \sin\left(\frac{\pi}{L}x\right), x \in [-L, L] \tag{27}$$

and periodic boundary conditions. $L = 6$ and time step $\Delta T = 0.0001$ is used to solve the problem till $T = 3.0$ by different schemes.

Firstly, we compare numerical errors of WCNS and CPR on the uniform grid. It can be seen from Table 1 that both WCNS and CPR achieve desired third-order accuracy. In addition, CPR has smaller error than WCNS under the same degrees of freedom (DOFs).

Secondly, the performance of the hybrid WCNS-CPR scheme is studied. To study the convergence accuracy of the hybrid scheme, a very small $\delta_{\mathrm{NI}} = 2.0 \times 10^{-8}$ is used to avoid that purely CPR scheme is used in this smooth problem. As shown in Figures 7(c)–7(e), the gray line with light blue dots represents values of NI at each solution point. The value of cell indicator (in dark blue line) represents the scheme used in every cell. When the indicator is 1, WCNS is employed. Indicator of value 0 means the cell is smooth, and it is calculated by CPR. As the number of DOFs gets larger, the percentage of WCNS cells decreases. When the number of DOFs becomes 480, the solution is smooth enough and CPR is used in all the cells. From numerical errors in Table 1, we can see that the hybrid scheme achieves expected third-order accuracy.

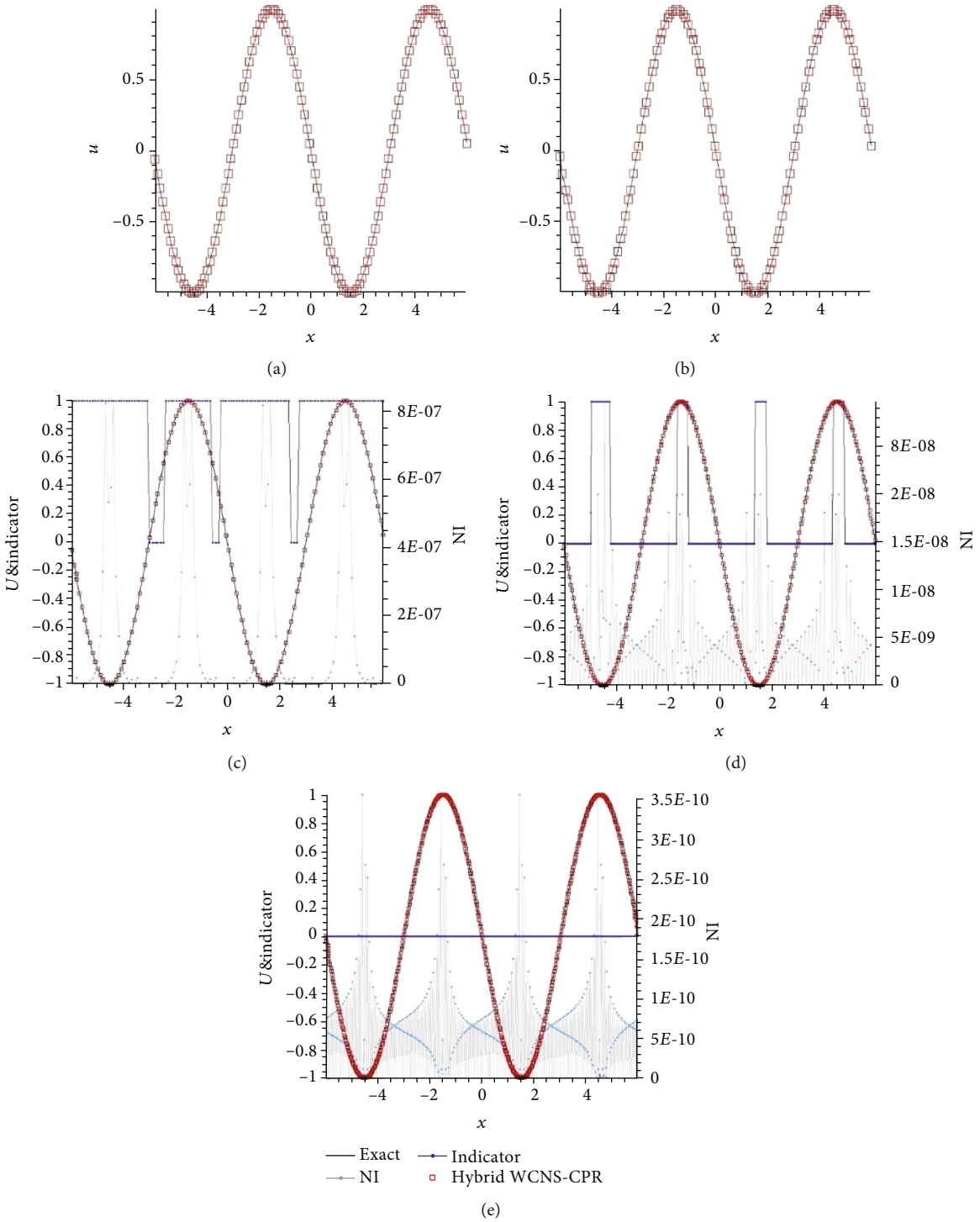

Figure 7: Numerical results of third-order single scheme and hybrid WCNS-CPR scheme. (a) WCNS in [−6, 6] with DOFs = 120. (b) CPR in [−6, 6] with DOFs = 120. (c) Hybrid WCNS-CPR scheme in [−6, 6] with DOFs = 120. (d) Hybrid WCNS-CPR scheme in [−6, 6] with DOFs = 240. (e) Hybrid WCNS-CPR scheme in [−6, 6] with DOFs = 480.

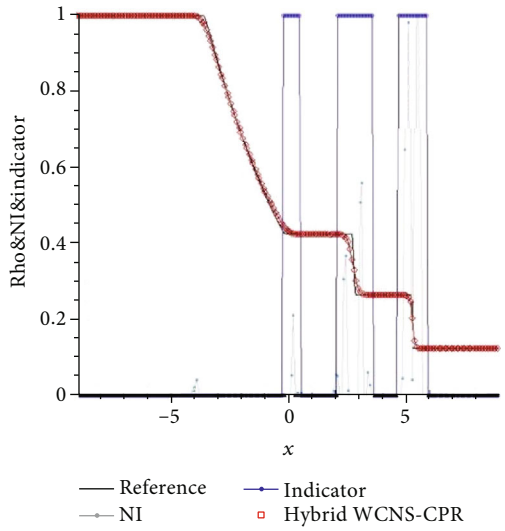

Figure 8: Density numerical solution and shock detection result of the hybrid WCNS-CPR scheme for the 1D Sod problem.

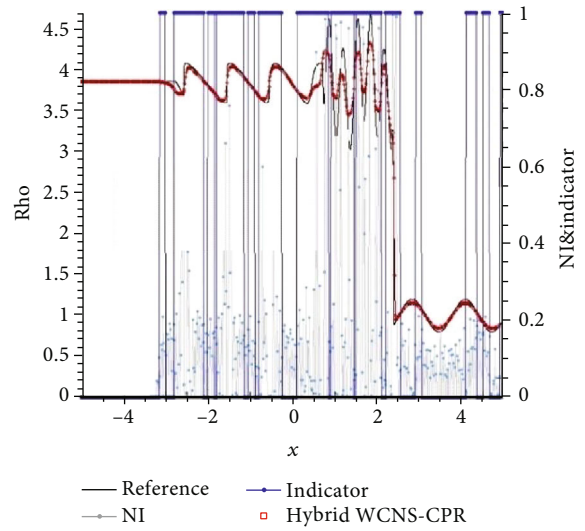

Figure 9: Density numerical solution and shock detection result of the hybrid WCNS-CPR scheme for the 1D Shu-Osher problem.

4.2. 1D Euler Equations. Consider 1D Euler equations

$$u_t + f(u)_x = 0, \tag{28}$$

where

$$u = \begin{pmatrix} \rho \\ \rho v \\ E \end{pmatrix}, \quad f(u) = \begin{pmatrix} \rho v \\ \rho v^2 + p \\ v(E+p) \end{pmatrix}, \tag{29}$$

where ρ is the density, v is the velocity, E is the total energy, and p is the pressure, which is related to the total energy by $E = (p/(\gamma - 1)) + (1/2)\rho v^2$ with $\gamma = 1.4$. Three kinds of shock-tube problems are considered in this subsection.

4.2.1. Shock-Tube Problem of Sod. Consider the Sod problem with initial conditions [29]

$$(\rho, u, p) = \begin{cases} (0.125, 0, 0.1), & -5 \le x < 0, \\ (1.0, 0, 1.0), & 0 \le x \le 5, \end{cases} \tag{30}$$

and Dirichlet boundary conditions. Time step $\Delta T = 0.0001$, DOFs = 210, and $\delta_{NI} = 0.2$ are used to solve the problem till $T = 3.0$ by the hybrid WCNS-CPR scheme. The reference solution is obtained by the WCNS3 scheme with DOFs = 2100. As shown in Figure 8, shocks and contact discontinuities can be well captured. Near the contact discontinuity ($x \approx 3$) and the shock ($x \approx 5$), no obvious oscillation is observed, which shows the good shock-capturing ability of the hybrid scheme. In addition, the CPR scheme is adopted in the main computational domain. The use of CPR scheme helps save computational cost since the linear CPR scheme is more efficient than the nonlinear WCNS scheme as will be shown in Section 4.3.1.

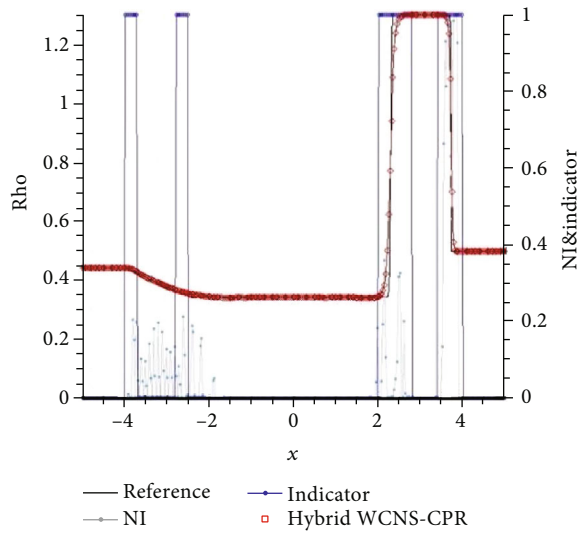

Figure 10: Density numerical solution and shock detection result of the hybrid WCNS-CPR scheme for the 1D Lax problem.

4.2.2. Shu-Osher Problem. Consider the Shu-Osher problem with initial conditions [30]

$$(\rho, u, p) = \begin{cases} (3.857143, 2.629369, 10.33333), & x < 4, \\ (1.0 + 0.2 \sin(5x), 0, 1.0), & x \ge 4, \end{cases} \tag{31}$$

and Dirichlet boundary conditions. Time step $\Delta T = 0.0001$, DOFs = 600, and $\delta_{NI} = 0.2$ are used to solve the problem till $T = 1.8$ by the hybrid WCNS-CPR scheme.

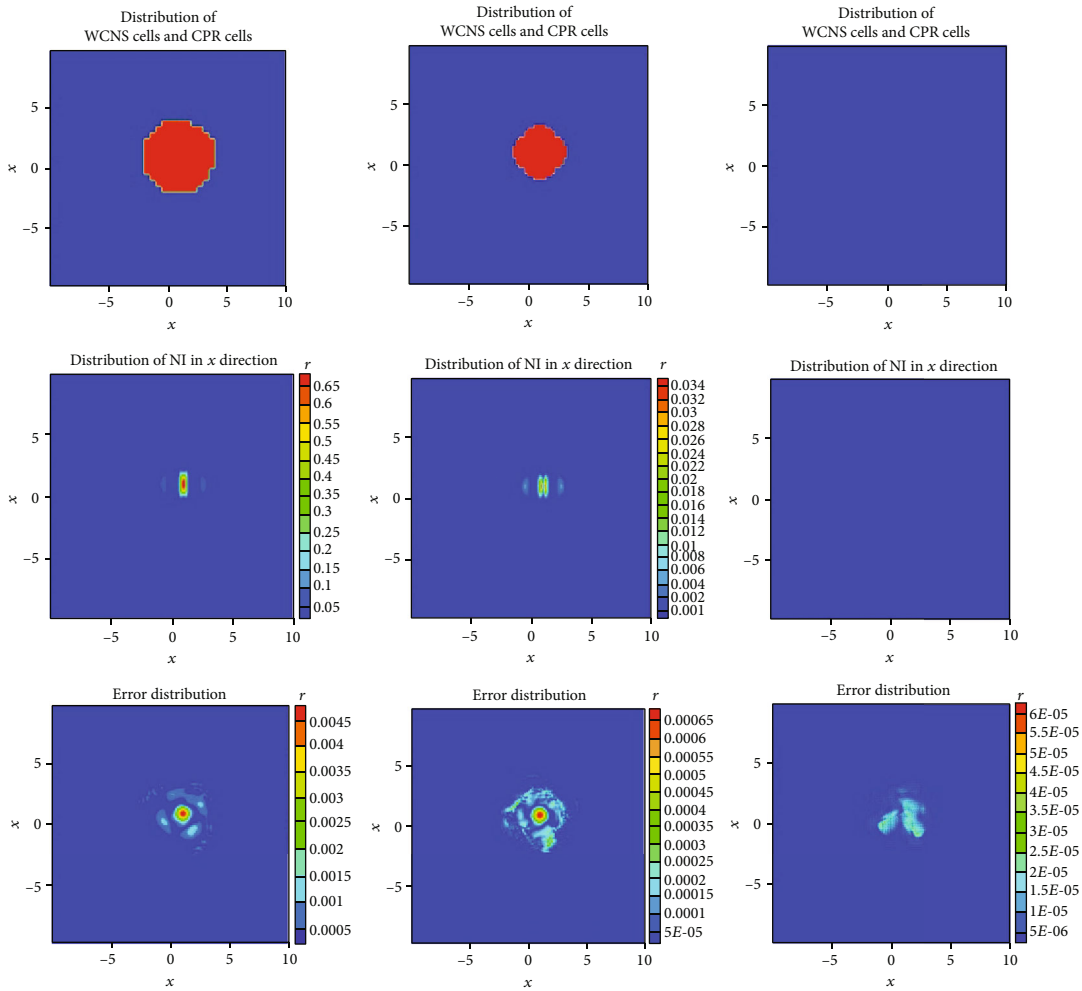

Figure 11: Distribution of different cells, errors, and NI in the x direction at $T = 1.0$ for DOFs = 120,240,480 (from left to right).

The reference solution is obtained by the WCNS3 scheme with DOFs = 9000. As shown in Figure 9, CPR is employed in the smooth area. Moreover, the hybrid scheme can capture shocks and discontinuities well. The numerical result of density obtained by the hybrid scheme is in good agreement to the reference, which illustrates the high-resolution property of the hybrid scheme.

4.2.3. Shock-Tube Problem of Lax. Consider the Lax problem with initial condition [31]

$$(\rho, u, p) = \begin{cases} (0.445, 0.698, 3.528), & -5 \le x < 0, \\ (0.5, \quad 0, \quad 0.571), & 0 \le x \le 5, \end{cases} \tag{32}$$

and Dirichlet boundary conditions. Time step $\Delta T = 0.0001$, DOFs = 300, and $\delta_{\mathrm{NI}} = 0.2$ are adopted to solve the problem till $T = 1.5$ by the hybrid WCNS-CPR scheme. The reference solution is obtained by the WCNS3 scheme with DOFs = 2100. We know from Figure 10 that at $x \approx 2.3$ and $x \approx 3.8$, shocks and discontinuities are all captured without obvious oscillations.

4.3. 2D Euler Equations. Let us consider the 2D Euler equations of gas dynamics:

$$\frac{\partial}{\partial t}\begin{bmatrix} \rho \\ \rho u \\ \rho v \\ E \end{bmatrix} + \frac{\partial}{\partial x}\begin{bmatrix} \rho u \\ \rho u^2 + p \\ \rho uv \\ u(E+p) \end{bmatrix} + \frac{\partial}{\partial y}\begin{bmatrix} \rho v \\ \rho uv \\ \rho v^2 + p \\ v(E+p) \end{bmatrix} = 0, \tag{33}$$

$$p = (\gamma - 1) \cdot \left[E - \frac{\rho}{2}\left(u^2 + v^2\right) \right]. \tag{34}$$

For an ideal gas, $\gamma = 1.4$. Here, ρ,u,v,p, and E are the density, the x direction velocity, the y direction velocity, the pressure, and the total energy, respectively.

4.3.1. 2D Isentropic Vortex Problem. In this subsection, the hybrid WCNS-CPR scheme is adopted to solve the isentropic vortex problem [32]. The initial condition is a mean flow, $\{\rho, u, v, p\} = \{1, 1, 1, 1\}$, with the isotropic vortex perturbations added to the mean flow. There are

Table 2: Accuracy test of single scheme and hybrid WCNS-CPR scheme for the Euler equations.

Norm	DOFs	WCNS		CPR		Hybrid WCNS-CPR	
		Error	Order	Error	Order	Error	Order
L_∞	120	$4.86E-3$	—	$2.14E-3$	—	$4.86E-3$	—
	240	$6.87E-4$	2.82	$3.17E-4$	2.76	$6.86E-4$	2.82
	480	$8.70E-5$	2.98	$6.48E-5$	2.29	$6.48E-5$	3.40
L_2	120	$2.21E-4$	—	$1.04E-4$	—	$2.34E-4$	—
	240	$3.18E-5$	2.80	$1.95E-5$	2.42	$4.20E-5$	2.48
	480	$4.02E-6$	2.98	$3.76E-6$	2.37	$3.76E-6$	3.48

perturbations in u, v and $T = p/\rho$ and no perturbation in entropy $S = p/\rho^\gamma$:

$$(\Delta u, \Delta v) = \frac{\varepsilon}{2\pi} e^{0.5(1-r^2)}(-y, x),$$
$$\Delta T = -\frac{(\gamma-1)\varepsilon^2}{8\gamma\pi^2} e^{(1-r^2)}, \tag{35}$$

where $r = \sqrt{x^2+y^2}$ and the vortex strength $\varepsilon = 5$. The computational domain is $[-10, 10] \times [-10, 10]$ with periodic boundary conditions. The problem is solved till $T = 1$ with time step $\Delta T = 0.0001$ for accuracy test. The parameter is $\delta_{\mathrm{NI}} = 0.001$ in this test.

Figure 11 shows distribution of different cells, NI in the x direction (NI in the y direction is central symmetric with it), and error distribution. When DOFs are 120 and 240, the central parts of the computational domain (which are in red) are calculated by WCNS. However, when DOFs = 480, all cells are calculated by CPR. This is because that, as the number of DOFs gets larger, NI gets smaller in this smooth problem. When parameter δ_{NI} is lower than the smallest NI in the computational domain, the whole domain is judged as smooth area and only CPR is employed.

From Table 2, we can see that the numerical errors of CPR alone are smaller than those of WCNS under the same DOFs. In addition, the WCNS scheme achieves third-order accuracy, while the order of accuracy of CPR is about 2.5. The hybrid WCNS-CPR scheme achieves third-order accuracy.

From Table 3, we can see that the computational cost of WCNS with characteristic projection is more than twice than that of CPR under the same DOFs. Considering that the errors of CPR are smaller than those of WCNS as shown in Table 2, the efficiency of CPR is even higher than that of WCNS under the same error.

Table 3: The comparison of CPU time in isentropic vortex problem.

DOFs	WCNS*		CPR
	Time (min)	Ratio	Time (min)
120×120	45	2.37	19
240×240	181	2.13	85
480×480	729	2.01	363

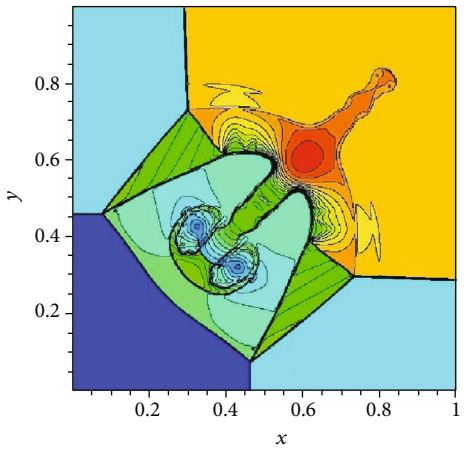

Figure 12: Result calculated by WCNS. DOFs = 960×960. Density from 0.13 to 1.78 with 25 contours.

Remark 2. WCNS∗ represents WCNS with characteristic projection. Ratio = (time of WCNS*)/(time of CPR).

4.3.2. 2D Riemann Problem. We solve the Riemann problem for equation (33) on the computational domain of $(x, y) \in [0, 1] \times [0, 1]$ with initial conditions

$$(\rho, u, v, p)(x, y, 0) = \begin{cases} (1.5, 0, 0, 1.5), & \text{if } 0.8 < x < 1.0 \text{ and } 0.8 < y < 1.0, \\ (0.5323, 1.206, 0, 0.3), & \text{if } 0 < x < 0.8 \text{ and } 0.8 < y < 1.0, \\ (0.138, 1.206, 1.206, 0.029), & \text{if } 0 < x < 0.8 \text{ and } 0 < y < 0.8, \\ (0.5323, 0, 1.206, 0.3), & \text{if } 0.8 < x < 1.0 \text{ and } 0 < y < 0.8, \end{cases} \tag{36}$$

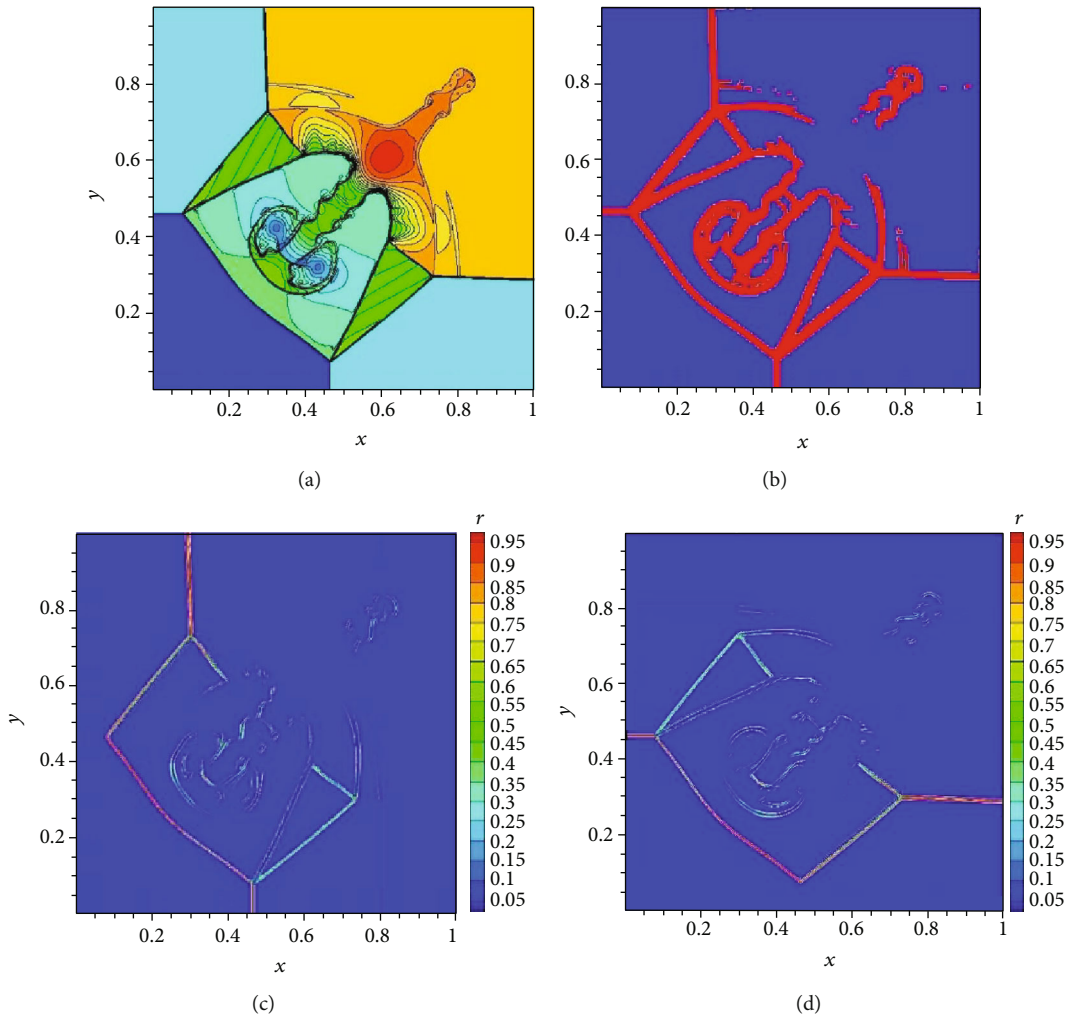

Figure 13: Results calculated by the hybrid WCNS-CPR scheme. NI = 0.1. DOFs = 960 × 960. (a) Density from 0.13 to 1.78 with 25 contours. (b) Distribution of different cells: red represents WCNS, blue represents CPR. (c) NI in the x direction. (d) NI in the y direction.

and Dirichlet boundary conditions until $T = 0.8$. The parameter is $\delta_{\mathrm{NI}} = 0.1$ in this test.

Compared with the results of WCNS in Figure 12, the results of the hybrid scheme in Figure 13(a) capture the flow field accurately with no obvious oscillation. In addition, small-scale structures are better captured by the hybrid scheme. We can see in Figure 13(b) that most of the computational domain is calculated by CPR, which contributes to the high efficiency of the hybrid scheme.

4.3.3. Double Mach Reflection Problem. This test is first described by Woodward and Colella [33]. It is aimed at testing the robustness of the high-resolution schemes. A Mach 10 oblique shock is initially set up at $x = 1/6$ on the lower boundary, and its direction is 60° from the x-axis. Inflow and slip wall boundary conditions are specified at the bottom boundary for $x = [0, 1/6]$ and $x > 1/6$, respectively. For the upper boundary ($y = 1$), a time-dependent boundary based on the analytical propagation speed of the oblique shock is imposed.

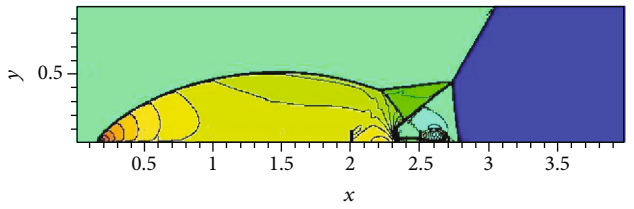

Figure 14: Density counters from 1.5 to 21.7 with 30 contours of double Mach reflection problem calculated by single WCNS. DOFs = 1200 × 300.

The initial condition is

$$(\rho, u, v, p) = \begin{cases} (1.4, 0.0, 0.0, 1.0), & \text{if } y < \sqrt{3}\left(x - \dfrac{1}{6}\right), \\ (8.0, 7.145, -4.125, 116.5), & \text{if } y \geq \sqrt{3}\left(x - \dfrac{1}{6}\right). \end{cases} \tag{37}$$

The simulation is run until $T = 0.2$ using time step $\Delta T = 0.0001$.

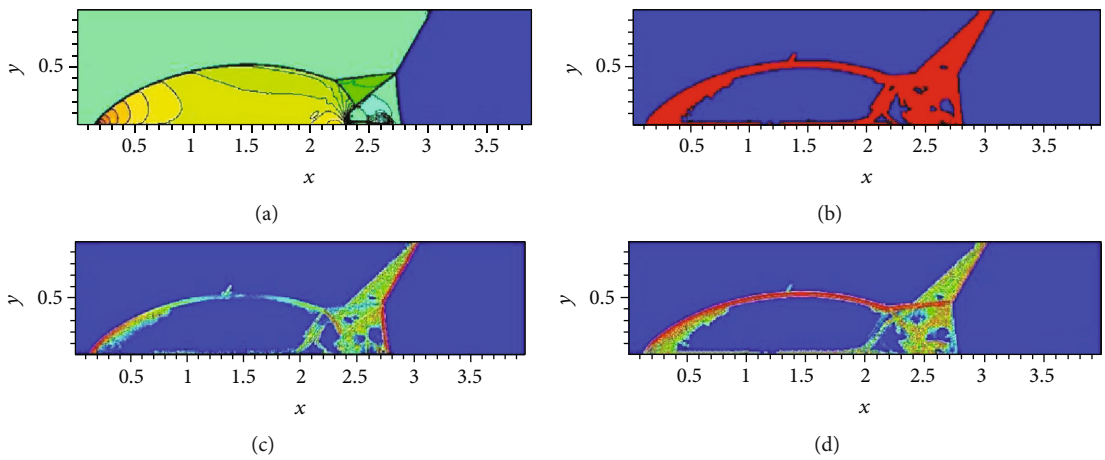

Figure 15: Results of the hybrid scheme. $\delta_{NI} = 0.9$. DOFs = 1200×300. Density from 1.5 to 21.7 with 30 contours. (a) Density contours from 1.5 to 21.7 with 30 contours. (b) Distribution of different cells: the red area represents WCNS cells, and the blue area represents CPR cells. (c) Distribution of NI in the x direction. (d) Distribution of NI in the y direction.

Table 4: CPU time comparison on solving the double Mach reflection problem.

DOFs	WCNS	Hybrid WCNS-CPR scheme		
		$\delta_{NI} = 0.1$	$\delta_{NI} = 0.5$	$\delta_{NI} = 0.9$
600×150	63 min	60 min	58 min	56 min
1200×300	314 min	217 min	207 min	202 min

As shown in Figures 15(a) and 15(b), essential small- and large-scale structures of the flow field are well captured compared with the results of WCNS in Figure 14. The remaining area is accurately calculated by the CPR method as well. Moreover, the total number of cells using CPR is much more than that using WCNS. As a result, the computational efficiency of the hybrid scheme is higher than that of WCNS as shown in Table 4. For DOFs = 600×150 and $\delta_{NI} = 0.9$, the hybrid scheme is slightly more efficient than WCNS. However, for DOFs = 1200×300 and $\delta_{NI} = 0.9$, the hybrid time is about 1.6 times more efficient than the WCNS scheme.

5. Concluding Remarks

In this paper, a new hybrid WCNS-CPR scheme for simulating conservation laws with discontinuities is proposed by introducing nonlinear weighted approach of WCNS to the linear hybrid scheme. Shock detector based on nonlinear weights is used to detect nonsmooth troubled cells and buffer cells. In these cells, WCNS is employed in order to capture shocks, while in smooth cells CPR is used to maintain high computational efficiency. By introducing buffer cells, the scheme interfaces are by design placed in relatively smooth regions and a linear interpolation method is used for the CPR to provide information for the WCNS scheme. Accuracy tests, shock-capturing tests, and computational efficiency tests are conducted. Accuracy tests in 1D and 2D show that the hybrid scheme achieves designed high-order accuracy. Shock-capturing tests illustrate that the hybrid scheme captures discontinuities without obvious oscillations. Computational efficiency tests show that the CPU cost of the hybrid WCNS-CPR scheme is relatively lower than that of WCNS.

In the future, the hybrid scheme will be generalized to three-dimensional cases and to Navier-Stokes equations.

Data Availability

The data used to support the findings of this study are available from the corresponding author upon request.

Conflicts of Interest

The authors declare that they have no conflicts of interest.

Acknowledgments

This study was supported by the National Natural Science Foundation of China (Grant Nos. 11902344 and 11971481), the Basic Research Foundation of National Numerical Wind Tunnel Project (No. NNW2018-ZT4A08), and the foundation of State Key Laboratory of Aerodynamics (Grant No. SKLA2019010101). The authors would like to thank assistant researcher Chen Li from the State Key Laboratory of Aerodynamics for his valuable suggestions.

References

[1] H. T. Huynh, Z. J. Wang, and P. E. Vincent, "High-order methods for computational fluid dynamics: a brief review of compact differential formulations on unstructured grids," *Computers and Fluids*, vol. 98, pp. 209–220, 2014.

[2] X. G. Deng, M. L. Mao, G. H. Tu, H. X. Zhang, and Y. F. Zhang, "High-order and high accurate CFD methods and their applications for complex grid problems," *Communications in Computational Physics*, vol. 11, no. 4, pp. 1081–1102, 2012.

[3] F. Qu, J. J. Chen, D. Sun, J. Q. Bai, and C. Yan, "A new all-speed flux scheme for the Euler equations," *Computers and Mathematic with Applications*, vol. 77, no. 4, pp. 1216–1231, 2019.

[4] F. Qu, D. Sun, B. Zhou, and J. Bai, "Self-similar structures based genuinely two-dimensional Riemann solvers in curvilinear coordinates," *Journal of Computational Physics*, vol. 420, article 109668, 2020.

[5] D. Sun, F. Qu, and C. Yan, "An efficient adaptive high-order scheme based on the WENO process," *Computers and Fluids*, vol. 140, pp. 81–96, 2016.

[6] Z. J. Wang, Y. Li, F. Jia et al., "Towards industrial large eddy simulation using the FR/CPR method," *Computers and Fluids*, vol. 156, pp. 579–589, 2017.

[7] H. J. Zhu, Z. G. Yan, H. Y. Liu, M. L. Mao, and X. G. Deng, "High-order hybrid WCNS-CPR schemes on hybrid meshes with curved edges for conservation laws I: spatial accuracy and geometric conservation laws," *Communications in Computational Physics*, vol. 23, no. 5, pp. 1355–1392, 2018.

[8] H. T. Huynh, "A flux reconstruction approach to high-order schemes including discontinuous Galerkin methods," in *18th AIAA Computational Fluid Dynamics Conference*, p. 4079, Miami, FL, June 2007.

[9] Z. Wang and H. Gao, "A unifying lifting collocation penalty formulation including the discontinuous Galerkin, spectral volume/difference methods for conservation laws on mixed grids," *Journal of Computational Physics*, vol. 228, no. 21, pp. 8161–8186, 2009.

[10] Y. Abe, T. Haga, T. Nonomura, and K. Fujii, "Conservative high-order flux-reconstruction schemes on moving and deforming grids," *Computers and Fluids*, vol. 139, pp. 2–16, 2016.

[11] J. J. Yang, B. Zhang, C. L. Liang, and Y. W. Rong, "A high-order flux reconstruction method with adaptive mesh refinement and artificial diffusivity on unstructured moving/deforming mesh for shock capturing," *Computers and Fluids*, vol. 139, pp. 17–35, 2016.

[12] C. Zhang, Q. B. Li, S. Fu, and Z. J. Wang, "A third-order gas-kinetic CPR method for the Euler and Navier–Stokes equations on triangular meshes," *Journal of Computational Physics*, vol. 363, pp. 329–353, 2018.

[13] Z. J. Wang, K. Fidkowski, R. Abgrall et al., "High-order CFD methods: current status and perspective," *International Journal for Numerical Methods in Fluids*, vol. 72, no. 8, pp. 811–845, 2013.

[14] J. Du, C. W. Shu, and M. Zhang, "A simple weighted essentially non-oscillatory limiter for the correction procedure via reconstruction (CPR) framework," *Applied Numerical Mathematics*, vol. 90, pp. 146–167, 2015.

[15] Q. Lu, G. Liu, P. Ming, and Z. J. Wang, "A parameter-free gradient-based limiter for the FR/CPR method on mixed unstructured meshes," in *AIAA Aviation 2019 Forum*, p. 3210, Dallas, Texas, June 2019.

[16] W. Li, Q. Wang, and Y. X. Ren, "A p-weighted limiter for the discontinuous Galerkin method on one-dimensional and two-dimensional triangular grids," *Journal of Computational Physics*, vol. 407, article 109246, 2020.

[17] G. E. Barter and D. L. Darmofal, "Shock capturing with PDE-based artificial viscosity for DGFEM: part I. Formulation," *Journal of Computational Physics*, vol. 229, no. 5, pp. 1810–1827, 2010.

[18] P. O. Persson and J. Peraire, "Sub-cell shock capturing for discontinuous Galerkin methods," in *44th AIAA Aerospace Sciences Meeting and Exhibit*, Reno, Nevada, January 2006.

[19] M. Dumbser, O. Zanotti, R. Loubere, and S. Diot, "A posteriori subcell limiting of the discontinuous Galerkin finite element method for hyperbolic conservation laws," *Journal of Computational Physics*, vol. 278, pp. 47–75, 2014.

[20] J. Cheng, Y. W. Lu, and T. G. Liu, "Multidomain hybrid RKDG and WENO methods for hyperbolic conservation laws," *SIAM Journal on Scientific Computing*, vol. 35, no. 2, pp. A1049–A1072, 2013.

[21] J. Cheng, K. Wang, and T. G. Liu, "A general high-order multidomain hybrid DG/WENO-FD method for hyperbolic conservation laws," *Journal of Computational Mathematics*, vol. 34, no. 1, pp. 30–48, 2019.

[22] H. J. Zhu, X. G. Deng, M. L. Mao, H. Y. Liu, and G. H. Tu, "Osher flux with entropy fix for two-dimensional Euler equations," *Advances in Applied Mathematics and Mechanics*, vol. 8, no. 4, pp. 670–692, 2016.

[23] X. G. Deng and H. X. Zhang, "Developing high-order weighted compact nonlinear schemes," *Journal of Computational Physics*, vol. 165, no. 1, pp. 22–44, 2000.

[24] R. Borges, M. Carmona, B. Costa, and W. S. Don, "An improved weighted essentially non-oscillatory scheme for hyperbolic conservation laws," *Journal of Computational Physics*, vol. 227, no. 6, pp. 3191–3211, 2008.

[25] Z.-G. Yan, H. Y. Liu, M. L. Mao, Y. K. Ma, and H. J. Zhu, "Development of 3rd-order hwcns and its application in hypersonic flow," *Acta Aeronautica et Astronautica Sinica*, vol. 36, no. 5, pp. 1460–1470, 2015.

[26] B. Cockburn and C. W. Shu, "TVB Runge-Kutta local projection discontinuous Galerkin finite element method for conservation laws II: general framework," *Mathematics of Computation*, vol. 52, no. 186, pp. 411–435, 1989.

[27] L. Krivodonova, J. Xin, J. F. Remacle, N. Chevaugeon, and J. Flaherty, "Shock detection and limiting with discontinuous Galerkin methods for hyperbolic conservation laws," *Applied Numerical Mathematics*, vol. 48, no. 3-4, pp. 323–338, 2004.

[28] M. Wu and M. P. Martin, "Direct numerical simulation of supersonic turbulent boundary layer over a compression ramp," *AIAA Journal*, vol. 45, no. 4, pp. 879–889, 2007.

[29] G. A. Sod, "A survey of several finite difference methods for systems of nonlinear hyperbolic conservation laws," *Journal of Computational Physics*, vol. 27, no. 1, pp. 1–31, 1978.

[30] S. Pirozzoli, "On the spectral properties of shock-capturing schemes," *Journal of Computational Physics*, vol. 219, no. 2, pp. 489–497, 2006.

[31] P. D. Lax, "Weak solutions of nonlinear hyperbolic equations and their numerical computation," *Communications on Pure and Applied Mathematics*, vol. 7, no. 1, pp. 159–193, 1954.

[32] C. Hu and C. W. Shu, "Weighted essentially non-oscillatory schemes on triangular meshes," *Journal of Computational Physics*, vol. 150, no. 1, pp. 97–127, 1999.

[33] P. Woodward and P. Colella, "The numerical simulation of two-dimensional fluid flow with strong shocks," *Journal of Computational Physics*, vol. 54, no. 1, pp. 115–173, 1984.

Hindawi
International Journal of Aerospace Engineering
Volume 2020, Article ID 8811565, 12 pages
https://doi.org/10.1155/2020/8811565

Research Article

Safety Analysis of Integrated Modular Avionics System Based on FTGPN Method

Haiyun Yang,[1] **Youchao Sun**,[1] **Longbiao Li**,[1] **Yundong Guo**,[1] **Siyu Su**,[1] **and Qijun Huangfu**[2]

[1]*College of Civil Aviation, Nanjing University of Aeronautics and Astronautics, Nanjing 210016, China*
[2]*Nanjing Glaway Software Co., Ltd., Nanjing 210013, China*

Correspondence should be addressed to Youchao Sun; sunyc@nuaa.edu.cn

Received 27 May 2020; Revised 5 August 2020; Accepted 18 August 2020; Published 1 September 2020

Academic Editor: Feng Qu

Compared with federated avionic architecture, the integrated modular avionic (IMA) system architecture in the aircraft can provide more sophisticated and powerful avionic functionality, and meanwhile, it becomes structurally dynamic, variably interconnected, and highly complex. The traditional approach such as fault tree analysis (FTA) becomes neither convenient nor sufficient in making safety analysis of the IMA system. In order to overcome the limitations, the approach that FTA combines with generalized stochastic petri net (GSPN) is proposed. First, FTA is used to establish the static model for the top level of the IMA system, while GSPN is used to build a dynamic model for each cell system. Finally, the combination model is generated, which is called the FTGPN model. Moreover, the FTGPN model is made safety analysis with the PIPE2 tool. According to the simulation result, corresponding measures are taken to meet the safety requirements of the IMA system.

1. Introduction

IMA system is evolving to provide more functionality with lesser parts, weight, and cost, while it is also meeting all the reliability and safety constraints [1–4]. To cope efficiently with the high level of complexity, a novel and structured development methodology is required [5–7]. As known to all, FTA is widely used for safety analysis of the system, but it has some limitations. One of such limitation is that it can only evaluate the safety of static systems. However, the IMA system gives rise to a variety of dynamic failure characteristics such as functional dependencies between events and priorities of failure events [8].

Model-Based safety analysis (MBSA) utilizes software automation and integrates with design models to simplify the safety analysis of complex systems [9]. Among these MBSA methods, the HiP-HOPS focuses on the automatic construction of predictive system failure analyses [10–17]. Meanwhile, the languages such as Architecture Analysis and Design Language (AADL) and AltaRica are used, automatically analyzing potential failures in a system model. AADL provides a standardized textual and graphical notation for describing software and hardware system architectures and their functional interfaces [18, 19]. Therefore, the IMA system is proposed to model based on AADL [20–26]. However, its disadvantage is that it cannot directly perform safety analysis and needs to be converted to other safety analysis methods such as Petri net and HiP-HOPS [16, 17]. In addition, AltaRica [27] is high-level modelling language dedicated to safety analysis. Based on the AltaRica, there is a commercial tool called Simfia, which is the modelling platform for Airbus A380.

The two methods that GSPN and Fault tree driven Markov processes (FTDMP) are compared in [28]. Then, it points out that GSPN is at a higher level in modelling formalism and shows a superior modelling capacity compared to FTDMP. A conceptual framework, which incorporates the Semi-Markov Process (SMP) based complex behavior to HiP-HOPS for modelling of complex system is proposed in [29]. Although the quantitative analysis results obtained

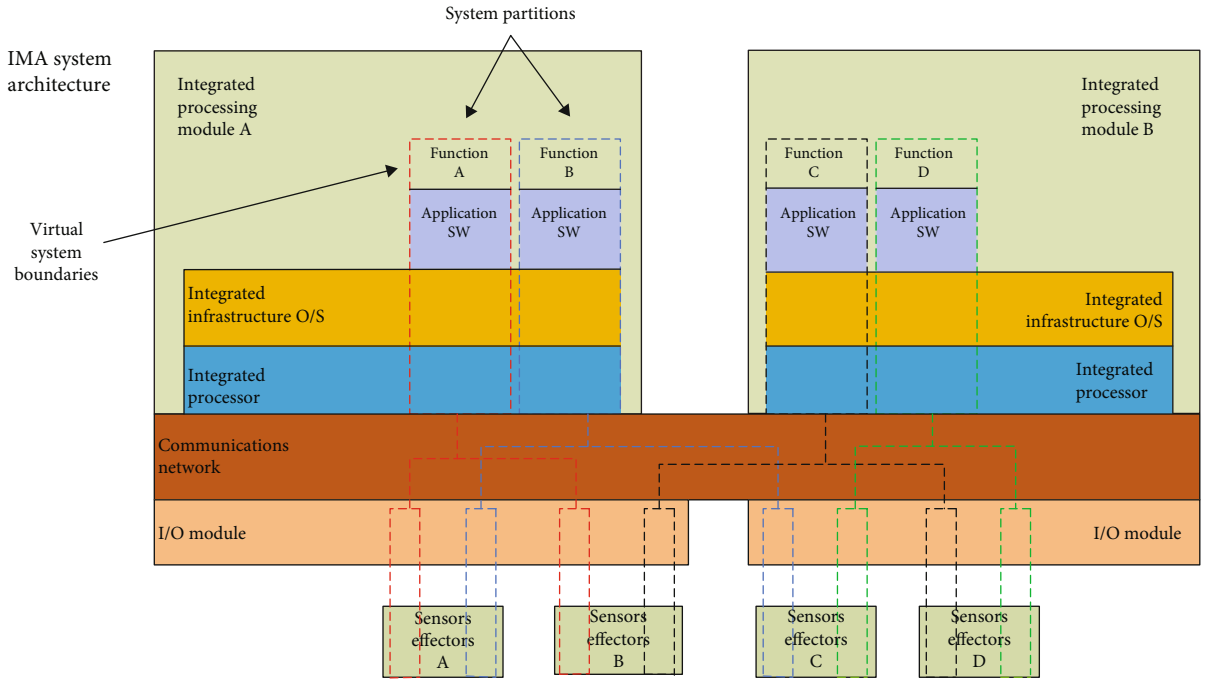

Figure 1: IMA system.

through this SMP [30, 31] is much more precise than the results from GSPN analysis, the safety model in GSPN is more intuitive. Moreover, in order to reduce the computation for GSPN analysis, many mature simulation software tools such as GreatSPN [32] and PIPE2 [33, 34] are developed.

The hybrid method that GSPN is used with these cell systems and the FTA process is applied to the upper-level system is validated effectively [35]. Then, it gained a clear view of the relationship between the failure of subsystems and the failure of the system. However, it also lacks the further safety evaluation for the whole system. In addition, GSPN in some works [36–43] have been used to build a safety model for a single dynamic system. But the model cannot illustrate its interactions with other systems.

Within this broader context, the smaller novelties include:

(1) According to the working principle, the IMA system is simplified in order to make the safety model more easily

(2) The proposed FTGPN method not only builds static safety analysis for the top level of the IMA system but also establishes the dynamic safety model for cell systems

(3) FTGPN model for the IMA system is simulated with PIPE2 tool and corresponding parameters can be adjusted to meet the safety requirements easily

FTGPN method solves the problem of being unable to conduct a comprehensive and accurate safety model for complex IMA system. Moreover, FTGPN provides an effective safety analysis method for the IMA system.

The section of this paper is organized as follows:

Section 2 introduces some preliminary knowledge mainly about the IMA system and the FTGPN method. Section 3 establishes the FTGPN model with FTA and GSPN for the IMA system. Section 4 makes the safety analysis for the FTGPN model. Section 5 depicts the capabilities and limitations of the FTGPN. Section 6 draws the conclusions.

2. Preliminary

In this section, the first IMA system is introduced. Then, an interview of the GSPN is given.

2.1. Integrated Modular Avionics. IMA architectures provide a general platform for hosting avionics in the aircraft. IMA platform includes the shared processing system, shared data network, and shared I/O system. The shared platform is an efficient means for implementing avionic functionality since it greatly reduces the electronic box and wire count in the aircraft. Therefore, the IMA system enables a great reduction in the size, weight, and power for a suite of avionic systems.

The IMA architecture is shown in Figure 1 [44]. The ARINC-653 standard is a common implementation of software partitioning [45]. It can guarantee each application's memory space and temporal execution environment so that they will not be affected by other applications.

The shared network replaces many dedicated communication lines with a shared backbone network. A common network implementation today is defined by the ARINC-664p7 standard [46]. ARINC-664p7 also includes the concept of partitioning through the use of Virtual Links (VLs) to ensure that communications from one application cannot affect the contents or impact the temporal characteristics of the message delivery (not-to-exceed data latency is guaranteed).

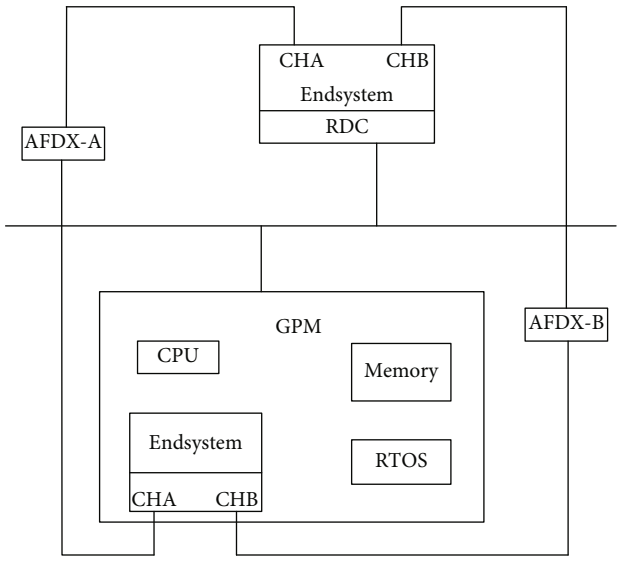

Figure 2: The simplified topology of the IMA system.

The shared Input/Output (I/O) system acts as a gateway to transfer I/O between many separate sources and the shared network. This makes the I/O available to all network-connected devices without having to run dedicated wiring in the aircraft. Since many sources of data are concentrated onto a common network, these devices are typically referred to as "Remote Data Concentrators (RDCs)" [47].

In order to model the IMA system, the simplified topology of the IMA system is attained and shown in Figure 2. These include the RDC, the General Processing Module (GPM), and the shared communication data network using the ARINC664 standard. The terminal AFDX has two independent communication interfaces, which are channels A and B, respectively. The software and hardware of the operating system for each GPM are the same while the software applications of the GPM are different [2].

The IMA system works as a converter and all communication signals are processed in the system. First, the non-AINC664 signal is converted to the ARINC664 signal. Second, the signal goes through RDC. Third, it is transmitted to the GPM through channel A or B. After the signal is being processed, it is output through channel A or B from GPM. Finally, the signal is changed to the corresponding non-ARINC664 signal at RDC. This whole process is the simplified work theory of the IMA system. The following sections will make a safety analysis for the IMA system based on its simplified structure.

2.2. Overview of GSPN. GSPN is consisted by places (circular), transitions (rectangular bars), directed arcs, and tokens (black bullets). The directed arcs connect input places to transitions or transitions to input places. The places "P" represent the state or condition of a component. The transition "T" describes the change in state from input to output place. However, the direction of the flow of tokens is determined by the directed arcs. Each arc has a multiplicity, which depicts the token migration capacity of the arc. The transition can only fire if the input place has an equal number of tokens or more as the arc multiplicity [48–50].

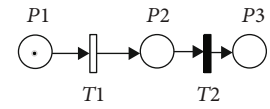

Figure 3: A simple GSPN.

In stochastic petri net (SPN), if a transition is fired, the token waits until the firing delay (which helps to stop the token). Once the firing delay ends, the migration of tokens takes place from initial to final place, and the number of tokens migrating depends upon the input and output functions. Then, SPN was extended to GSPN. Besides SPN features, two new features are added which are immediate transition firing and inhibitor arcs (used to disable the transition when a token is present in input places) [51, 52]. The definitions of the GSPN are introduced as follows.

A GSPN is a 6-tuple $(P, T, F, W, M_0, \lambda)$ where:

(1) $P = \{p_1, p_2, \cdots, p_m\}$ is a finite set of places, $n \geq 0$

(2) $T = T_1 \cap T_2$ presented all the transitions

$T_1 = \{t_1, t_2, \cdots, t_m\}$ is a finite set of timed transitions which is associated with a random delay time between enabling and firing;

$T_2 = \{t_{m+1}, t_{m+2}, \cdots, t_n\}$ is a finite set of immediate transitions which can be fired randomly and the delay is zero.

(3) $F \subseteq (P \times T) \cap (T \times P)$ is a set of arcs

There exist inhibitor arcs that can only form places to transitions and make the enable conditions to be disenabled.

(4) W is a weight function of arcs

(5) $M_0 : P \to \{0, 1, 2, 3, \cdots\}$ is initial marking where $(P \times T) = \varphi \cap (T \times P) = \varphi$

(6) $\lambda = \{\lambda_1, \lambda_2, \cdots, \lambda_n\}$ is a set of the firing rates corresponding to the timed transitions

M_i is from M_0. For example, as shown in Figure 3, M is represented by $\{P1, P2, P3\}$. M_0 is {1,0,0}. A new marking $M_1\{0, 1, 0\}$ is reached when timed transitions $T1$ is enabled. M_1 marking is Vanishing state because the immediate transition $T2$ is enabled at once. Meanwhile, the Tangible state $M_2\{0, 0, 1\}$ is reached. M_0, M_1, and M_2 are the reachability sets for the simple system. M_0 and M_2 are Tangible states, while M_1 is Vanishing state. That is Vanishing state can change to a new Tangible state immediately.

3. Proposed FTGPN Method

Traditional safety analysis methods (such as fault trees, reliability block diagrams, binary decision diagrams, and Markov process models) cannot effectively simulate the dynamic behaviour of the system. However, GSPN is suitable for modelling the dynamic behaviour of the system [50].

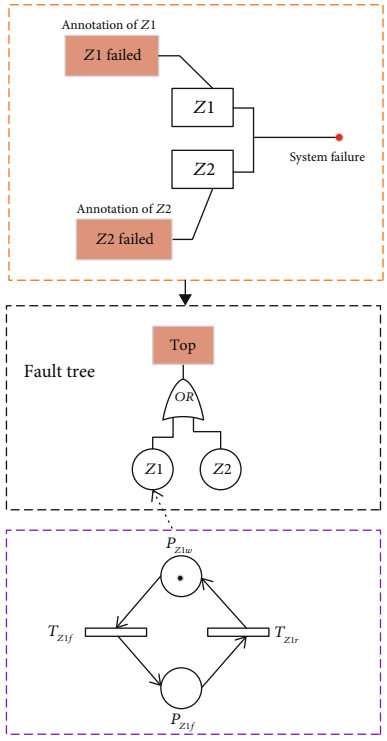

Figure 4: FTGPN is illustrated with a simple example.

Therefore, the FTGPN approach is developed to combine fault trees and GSPN in a new way. And FTGPN is used to make safety analysis for the IMA system in this paper.

3.1. Brief Description of FTGPN. FTGPN is depicted clearly with a simple example in Figure 4. The failure of component $Z1$ is represented by "$Z1$", while the failure of component $Z2$ is represented by "$Z2$". Fault tree uses λ_{z1} and μ_{z1} as the failure and repair rates of component $Z1$ for quantitative analysis. If the component $Z1$ has failed, the FTGPN would use a GSPN model to represent the failure behaviour of $Z1$.

FTGPN approach is applied in the following steps. First, the fault tree is used to clearly identify the cell systems' sequence with the deductive logic and establish the top level of the system. Second, the GSPN model for each cell systems is built. Third, the GSPN of cell systems are constructed according to the architecture of the fault tree. Finally, the FTGPN model for the whole system is formed and it can be made the safety analysis with the PIPE2 tool. And how to establish the FTGPN model for the IMA system will be introduced in detail in the following sections.

3.2. FTA Modelling. Generally, in order to ensure that the FTGPN model is correct and effective for application, some restrictions need to be made. It is assumed that the following conditions are true:

Assumption 1. Each component of the system has only two states, which are failed and operational.

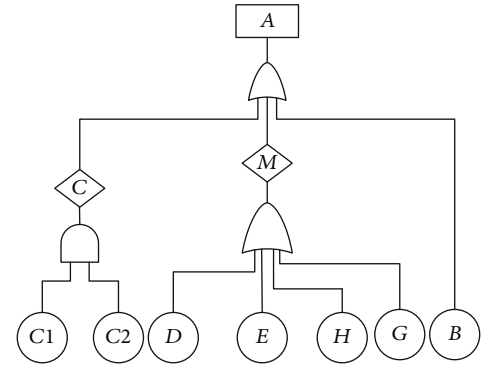

Figure 5: The FTA model of the IMA system.

Assumption 2. Each component in the system fails independently, and no more than two components will fail at the same time.

Assumption 3. The maintenance equipment is sufficient, and the component is repaired in time after failed, and the repaired component is new as before.

Assumption 4. The failure rate of component is λ.

Assumption 5. The repair rate of component is μ.

Figure 5 shows the fault tree analysis for the architecture of the IMA system. The failure of RDC is represented by B. Meanwhile channel A of ARINC664 network is $C1$ and channel B of ARINC664 network is $C2$. Then, both of them lead to the failure of ARINC664 network represented as C. In addition, CPU is D, memory is E, RTOS is H, and the software of end system is G. Therefore, that one of them is failure will lead to the failure of GPM represented as M. Moreover, the relationship among the RDC, the ARINC664 network, and the GPM is combined with "OR".

3.3. FTGPN Modelling. Based on the module theory, the GSPN model for GPM and ARINC664 network are established firstly. Finally, the top level of the FTGPN model for the IMA system is synthesized.

3.3.1. GPM Model. The GSPN of GPM model is illustrated in Figure 6, and model descriptions are presented in Tables 1 and 2. The working process for GPM is as follows. It is operational normally at first. After a random time, CPU changes from P_{dw} to the P_{df} and the marks in P_{mw} is empty (the number of marks in P_{mn} is 1, and it is used to prohibit the failure of other components in GPM), then the immediate transition T_{mf} is triggered, and the GPM changes from P_{mw} to P_{mf}. A random time later, it is assumed that the CPU in the GPM is repaired, and it changes from P_{df} to P_{dw} (the marks of P_{df} and P_{mn} disappear). Then, the CPU changes from P_{mf} to P_{mw}, and it indicates that CPU is operational.

3.3.2. ARINC664 Network Model. The GSPN model of the ARINC664 network is depicted in Figure 7, and the model descriptions are presented in Tables 3 and 4. The working

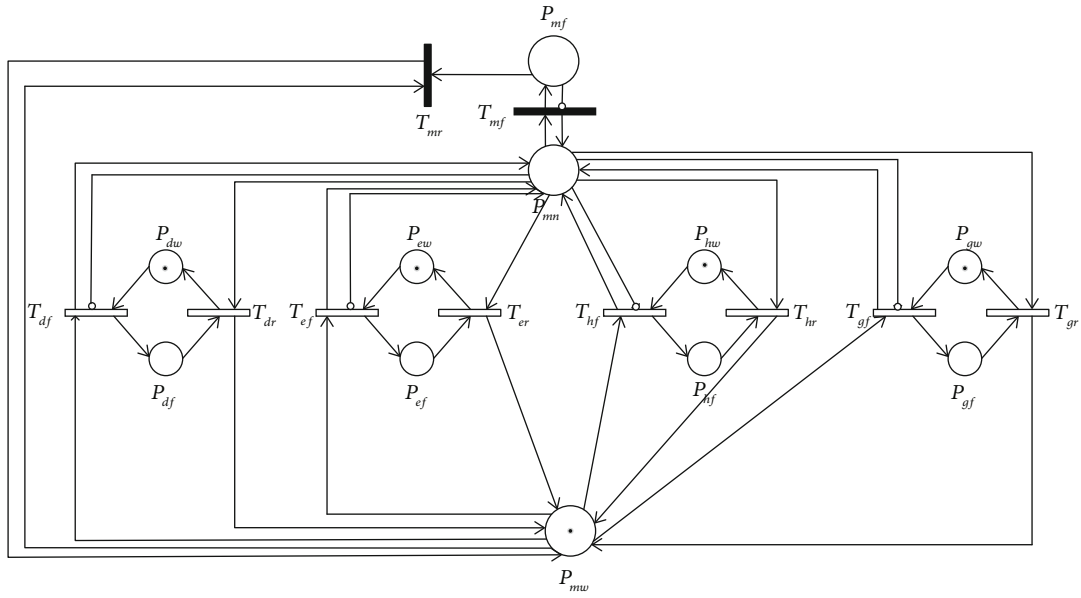

Figure 6: The GSPN model of GPM.

Table 1: Places in the GSPN model for GPM.

Name	Operational meaning
P_{mw}	GPM is operational
P_{mf}	GPM is failed
P_{dw}	CPU is operational
P_{df}	CPU is failed
P_{ew}	Memory is operational
P_{ef}	Memory is failed
P_{hw}	RTOS is operational
P_{hf}	RTOS is failed
P_{gw}	Software is operational
P_{gf}	Software is failed
P_{mn}	Number of components in failed state

Table 2: Transitions in GSPN model for GPM.

Name	Operational meaning	Trigger rate (1/h)
T_{mr}	GPM goes from failed to operational	—
T_{mf}	GPM goes from operational to failed	—
T_{dr}	CPU goes from failed to operational	0.001
T_{df}	CPU goes from operational to failed	2×10^{-5}
T_{er}	Memory goes from failed to operational	0.002
T_{ef}	Memory goes from operational to failed	2×10^{-5}
T_{hr}	RTOS goes from failed to operational	0.0011
T_{hf}	RTOS goes from operational to failed	5×10^{-5}
T_{gr}	Software goes from failed to operational	0.0011
T_{gf}	Software goes from operational to failed	5×10^{-5}

process for the ARINC664 network is as follows. It is operational normally at first. After a random time, ARINC664 network channel A changes from P_{c1w} to P_{c1f}, and the number of marks in P_{cw} becomes 1, then the number of marks in P_{cn} is 1. When the number of marks in P_{cw} becomes 0 and the number of marks in P_{cn} becomes 2, the immediate transition T_{cf} is triggered, and the ARINC664 network changes to P_{cf}. A random time later, ARINC664 network channel A changes from P_{c1f} to P_{c1w}, and the ARINC664 network system recovers to P_{cw}.

3.3.3. FTGPN Model. The FTGPN model of the IMA system is shown in Figure 8, and the model descriptions are presented in Tables 5 and 6. The working process for the IMA system is as follows. The IMA system works normally at first. After a random time, the transition T_{bf} is triggered and the IMA system changes to P_{af}. A random time later, the RDC recovers to operational, and the transition T_{br} is triggered next. Meanwhile, the mark of P_{af} disappears, and the IMA system recovers to operational. Finally, according to top level of FTA model for the IMA system, the GSPN models for the cell systems such as GPM and ARINC664 network are combined to the FTGPN model. Additionally, the safety analysis is made for the IMA system in the following sections.

4. Results and Discussion

The tool PIPE2 [33, 34] is used to make analysis for the FTGPN model of the IMA system. PIPE2 is an open-source tool that supports creating and analyzing Petri nets and has an easy-to-use graphical user interface that allows a user to establish stochastic petri net models. Additionally, the analysis environment in this tool includes different modules such as steady-state analysis, reachability/coverability graph analysis, and GSPN analysis [37].

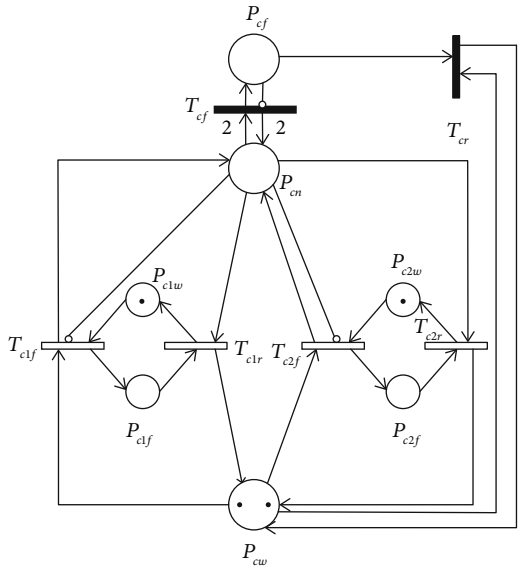

Figure 7: The GSPN model of ARINC664 network.

Table 3: Places in GSPN model for ARINC664 network.

Place	Operational meaning
P_{cw}	ARINC664 network is operational
P_{cf}	ARINC664 network is failed
P_{c1w}	ARINC664 network channel A is operational
P_{c1f}	ARINC664 network channel A is failed
P_{c2w}	ARINC664 network channel B is operational
P_{c2f}	ARINC664 network channel B is failed
P_{cn}	Number of channels in failed state

First, the FTGPN model is established in PIPE2 as shown in Figure 8. Then, the analysis results in Tables 7 and 8 can be obtained through GSPN analysis. As depicted in Table 7, the IMA system's operational states are $M0$, $M5$, and $M6$, and the number of tokens in P_{af} is 0. Moreover, the total value of $M0$, $M5$, and $M6$ is 0.89213. It equals to the probability of P_{af} when the number of tokens is 0 ($\mu = 0$) in Table 8. Therefore, the conclusion is that the probability of the IMA system in operational state is 0.89213.

Figure 9 illustrates the reachability graph of the FTGPN model for the IMA system. Each of the graph node acts as one of the IMA system states, and the initial state is node $S0$. It is known that $S0 = \{0, 0, 0, 0, 1, 0, 1, 0, 0, 2, 0, 1, 0, 1, 0, 1, 0, 1, 0, 0, 1\}$, which is represented by the number of tokens in each place. Also, $S0$ is corresponding to $M0$ in Table 7. In addition, the Tangible state is presented in red color, while the blue color is for Vanishing state. Therefore, the marking of the Tangible state is corresponding to the marking in Table 7.

As shown in Figure 9, the states are changed by firing the transitions. For instance, state $S0(M0)$ is fired by transition T_{c1f} and then becomes $S6(M6)$. Meanwhile, state $S0(M0)$ is fired by transition T_{c2f} and then becomes $S5(M5)$. These

Table 4: Transitions in GSPN model for ARINC664 network.

Transition	Operational meaning	Trigger rate (1/h)
T_{cf}	ARINC664 network goes from operational to failed	—
T_{cr}	ARINC664 network goes from failed to operational	—
T_{c1f}	ARINC664 network channel A goes from operational to failed	2×10^{-5}
T_{c1r}	ARINC664 network channel A goes from failed to operational	0.001
T_{c2f}	ARINC664 network channel B goes from operational to failed	2×10^{-5}
T_{c2r}	ARINC664 network channel B goes from failed to operational	0.001

can all be referred to in Table 7. The number of marks is changing in the corresponding transitions such as P_{c1f}, P_{c1w}, P_{c2f}, and P_{c2w}. Meanwhile, $S7(M1)$, $S8(M2)$, $S9(M3)$, and $S10(M4)$ can be found in the corresponding states in Table 7. The states in Table 7 match with the Tangible state with red color one by one in Figure 9. Although the results can be attained manually from Figure 7, the whole reachability graph for a complex system is got fast and accurate with the PIP2 tool.

In addition, every small part of the reachability graph is a closed loop. For instance, first, $S6(M6)$ is fired by transition T_{df} and becomes $S18$. Second, $S18$ is fired by transition T_{mf} and becomes $S27$. Third, $S27$ is fired by transition T_{dr} and becomes $S29$. Finally, $S29$ is fired by transition T_{mr} and returns to $S6(M6)$. The whole process is a circle which is depicted in purple color in Figure 9. And the reachability graph is composed of many circles. These indicate all the Tangible states and Vanishing states for the IMA system. Moreover, according to the reachability graph, further research for quantitative analysis can be made in the future.

The different initial random firings have been implemented for the simulation of the FTGPN model. The token distribution has been updated by 100, 500, and 1000 random firings, which are shown in Figure 10.

The graph in Figure 10 shows that the three lines almost coincide. The highest point is P_{cw}, and the average number of tokens is close to 2, while the lowest points are P_{bf}, P_{bw}, and P_{cf}. The value of P_{bw} is not our expectation. Therefore, corresponding countermeasures should be developed to increase its value and make it get to 1. Obviously, the simulation for the FTGPN model allows users to analyze the failure behavior of IMA systems in a more intuitive way. In fact, the above simulations are used to explain the application to the FTGPN model of the IMA system. However, it does not correspond to the real case in the aircraft. For example, there is no repair for the IMA system when the FTGPN model is based on the flight. Although the FTGPN method for modelling the IMA system is verified effectively, further quantitative analysis should be made in the future.

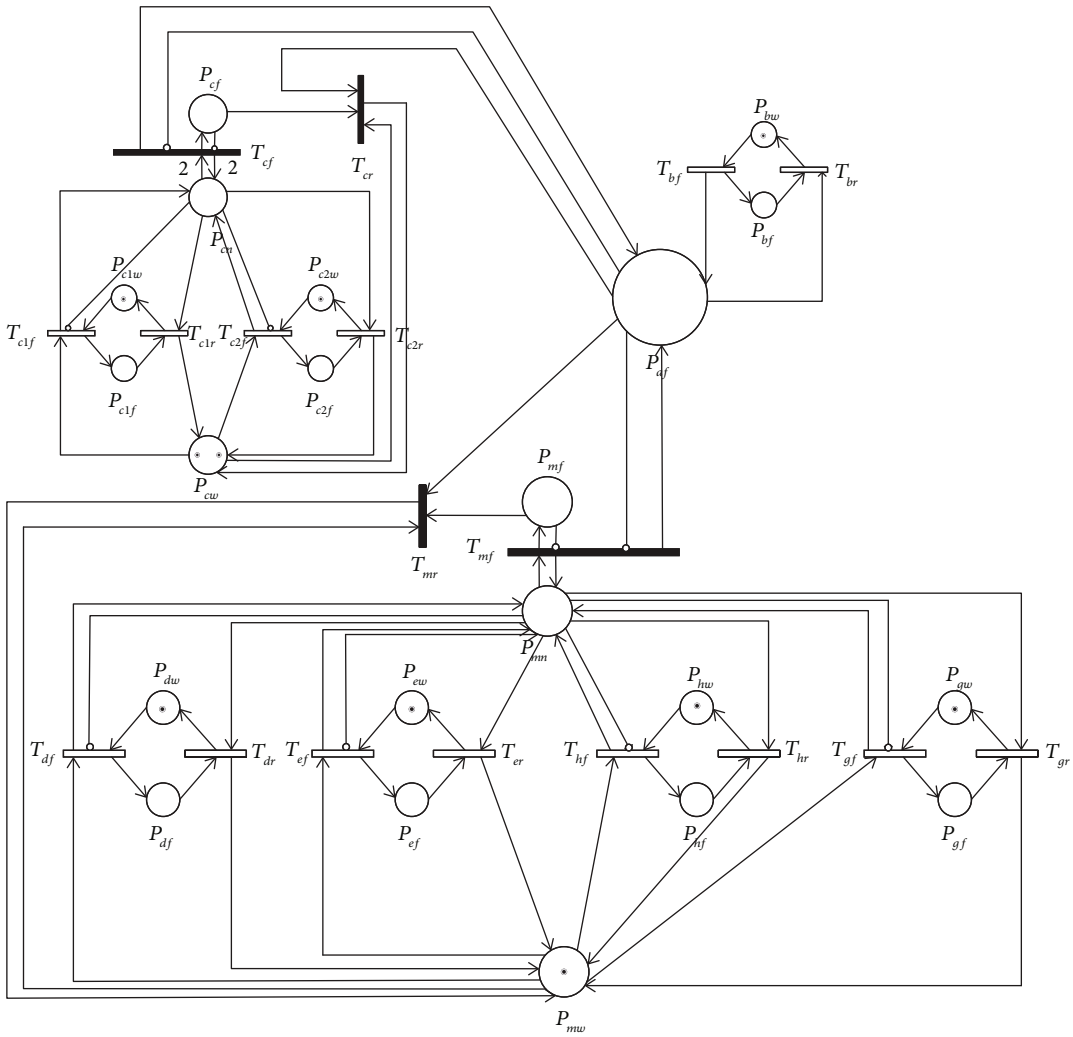

Figure 8: FTGPN model of the IMA system.

Table 5: Places in GSPN model for RDC and IMA system.

Place	Operational meaning
P_{bw}	RDC is operational
P_{bf}	RDC is failed
P_{af}	IMA system is failed

Table 6: Transitions in the GSPN model for RDC.

Transition	Operational meaning	Trigger rate (1/h)
T_{bf}	RDC goes from operational to failed	2.0×10^{-5}
T_{br}	RDC goes from failed to operational	0.001

5. Capabilities and Limitations of the FTGPN

Some of the capabilities and limitations (limitation in making accurate quantitative analysis for the IMA system) of the FTGPN are discussed in this section.

5.1. Capabilities of the FTGPN. The FTGPN offers the following capabilities.

(1) First, the architecture of the IMA system is simplified according to the work theory. And this is a very important step to build the FTA model for the top level of the system

(2) The FTGPN method establishes the top level of the IMA system with FTA in the static model, while the cell systems are built with GSPN in a dynamic model. In addition, the dependency and interactions among the IMA system are depicted intuitively by the FTGPN model

(3) PIPE2 tool is chosen to make a simulation for the FTGPN model of the IMA system. The results are not only the Tangible states but also the probability of the IMA system in operational. In addition, the

Table 7: GSPN steady-state analysis results set of Tangible states.

	$M0$	$M1$	$M2$	$M3$	$M4$	$M5$	$M6$	$M7$	$M8$	$M9$	$M10$	$M11$	$M12$	$M13$	$M14$
P_{af}	0	1	1	1	1	0	0	1	1	1	1	1	1	1	1
P_{bf}	0	0	0	0	0	0	0	0	0	0	0	0	0	0	0
P_{bw}	0	0	0	0	0	0	0	0	0	0	0	0	0	0	0
P_{c1f}	0	0	0	0	0	0	1	0	1	0	1	0	1	0	1
P_{c1w}	1	1	1	1	1	1	0	1	0	1	0	1	0	1	0
P_{c2f}	0	0	0	0	0	1	0	1	0	1	0	1	0	1	0
P_{c2w}	1	1	1	1	1	0	1	0	1	0	1	0	1	0	1
P_{cf}	0	0	0	0	0	0	0	0	0	0	0	0	0	0	0
P_{cn}	0	0	0	0	0	1	1	1	1	1	1	1	1	1	1
P_{cw}	2	2	2	2	2	1	1	1	1	1	1	1	1	1	1
P_{df}	0	0	0	0	1	0	0	0	0	0	0	0	0	1	1
P_{dw}	1	1	1	1	0	1	1	1	1	1	1	1	1	0	0
P_{ef}	0	0	0	1	0	0	0	0	0	0	0	1	1	0	0
P_{ew}	1	1	1	0	1	1	1	1	1	1	1	0	0	1	1
P_{gf}	0	0	1	1	0	0	0	0	0	1	1	0	0	0	0
P_{gw}	1	1	0	0	1	1	1	1	1	0	0	1	1	1	1
P_{hf}	0	1	0	0	0	0	0	1	1	0	0	0	0	0	0
P_{hw}	1	0	1	1	1	1	1	0	0	1	1	1	1	1	1
P_{mf}	0	1	1	1	1	0	0	1	1	1	1	1	1	1	1
P_{mn}	0	1	1	1	1	0	0	1	1	1	1	1	1	1	1
P_{mw}	1	0	0	0	0	1	1	0	0	0	0	0	0	0	0

Table 8: Token probability density.

	P_{af}	P_{bf}	P_{bw}	P_{c1f}	P_{c1w}	P_{c2f}	P_{c2w}
$\mu = 0$	0.89213	1	1	0.98077	0.01923	0.98077	0.01923
$\mu = 1$	0.10787	0	0	0.01923	0.98077	0.01923	0.98077
$\mu = 2$	0	0	0	0	0	0	0
	P_{cf}	P_{cn}	P_{cw}	P_{df}	P_{dw}	P_{ef}	P_{ew}
$\mu = 0$	1	0.96154	0	0.98216	0.01784	0.99108	0.00892
$\mu = 1$	0	0.03846	0.03846	0.01784	0.98216	0.00892	0.99108
$\mu = 2$	0	0	0.96154	0	0	0	0
	P_{gf}	P_{gw}	P_{hf}	P_{hw}	P_{mf}	P_{mn}	P_{mw}
$\mu = 0$	0.95945	0.04055	0.95945	0.04055	0.89213	0.89213	0.10787
$\mu = 1$	0.04055	0.95945	0.04055	0.95945	0.10787	0.10787	0.89213
$\mu = 2$	0	0	0	0	0	0	0

reachability graph which depicts all the states can be attained automatically. Moreover, the number of tokens is illustrated clearly in each place. Therefore, the corresponding measures can be taken according to the simulation

5.2. Limitations of the FTGPN. The FTGPN has the following limitations. All will be resolved is our future works.

(1) The simplified IMA system is used in this paper. However, it is known that simplifying the complex

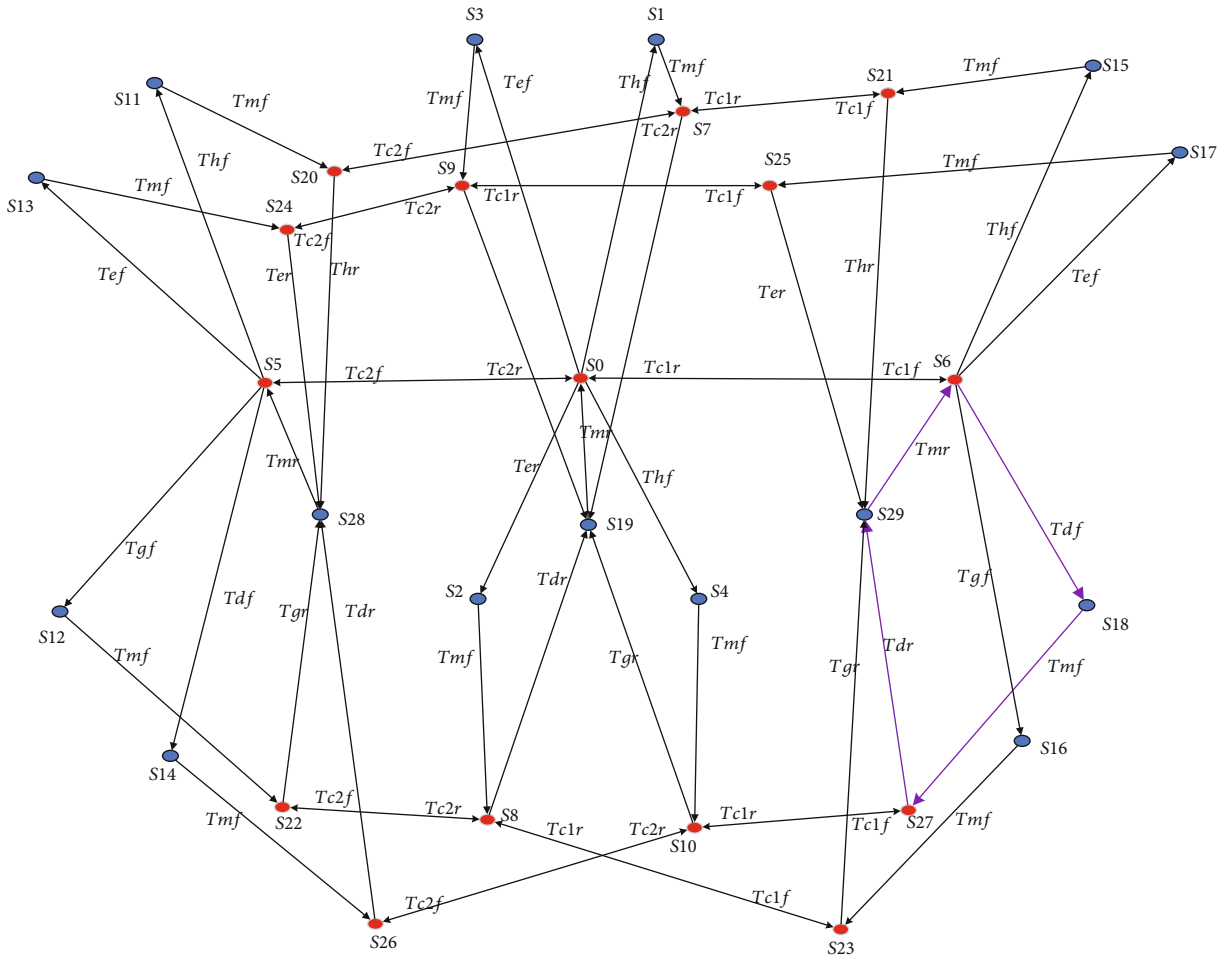

Figure 9: Reachability graph of the FTGPN model for the IMA system.

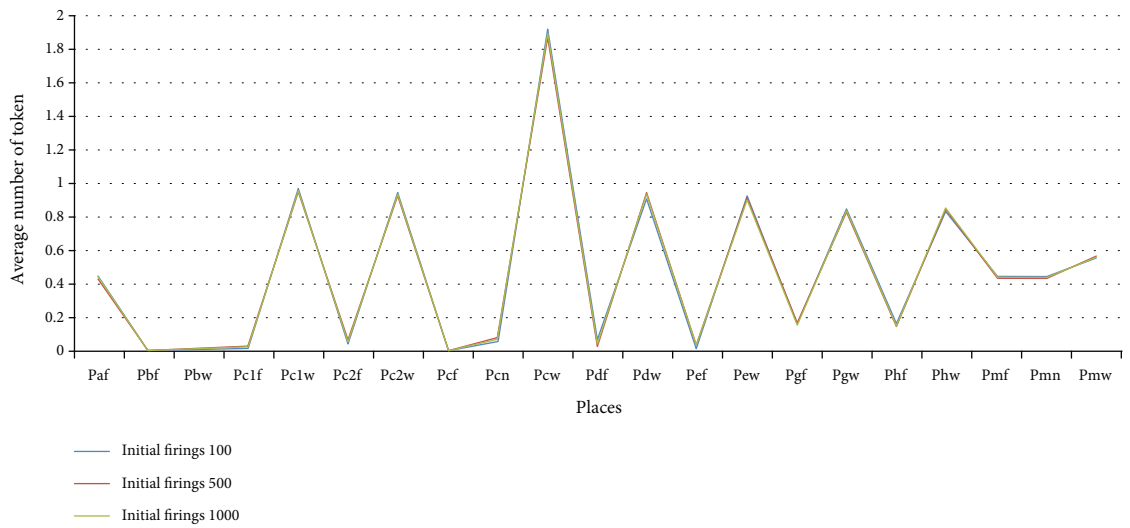

Figure 10: Token distribution of different number of firings.

system is difficult. Therefore, we should develop a new method to generate the FTA automatically. This work should be done in the future

(2) It takes much time to establish the FTGPN model. In addition, it is very easy to make mistakes in building model manually. Therefore, a software

which can generate the model automatically should be developed

(3) Comparing with the existing approaches [12, 29–32], the FTGPN method is better in establishing the safety model clearly and directly. However, quantitative analysis for FTGPN is not accurate. Therefore, the quantitative analysis of the FTGPN should be optimized and verified with the Aircraft fuel distribution system. Making optimization for quantitative analysis is my further work

(4) In this paper, the PIPE2 tool is chosen to make the simulation. Because of the limitations of the tool, the safety analysis is inadequate. Therefore, the functions for the tool should be extended especially in quantitative analysis

6. Conclusion

FTGPN model is proposed for dynamic safety analysis of the IMA system. First, FTA is introduced to make a static model for the top level of the IMA system, and then GSPN is employed to construct a dynamic model for cell systems. It represents an advancement model for safety analysis and allows faster, automatic analysis of dynamic systems using GSPN. The FTGPN model has combined the advanced features of FTA with GSPN. The integration for the two safety analysis methods is a potential tool to make the safety analysis for the complex and interactive IMA system.

The conclusions of this paper are as follows:

(1) The complex IMA system is simplified properly which makes the rest work such as establishing the FTGPN model more easily

(2) The FTGPN method for combining the FTA and GSPN and applying in the IMA system not only shows the relationship between cell systems but also simulates the dynamic interactions in each cell system

(3) PIPE2 is used to simulate the FTGPN model of the IMA system. All the parameters that we need are shown to us obviously. Then, we can adjust them to meet the safety requirements conveniently

However, for the large system including thousands of components, it is difficult to build the FTGPN model. It is better to develop a tool that can establish the FTGPN model and make safety analysis for it automatically.

Data Availability

No data were used to support this study.

Conflicts of Interest

The authors declare that they have no competing interests.

Acknowledgments

This paper is supported by the Research Program supported by the National Natural Science Foundation of China (U1333119), the National defense basic scientific research program of China (JCKY2013605B002), and the Civil Aircraft Special Foundation of Ministry of Industry and Information Technology (MJ-2017-J-91).

References

[1] D. Rajaram, Y. Cai, I. Chakraborty, and D. N. Mavris, "Integrated sizing and optimization of aircraft and subsystem architectures in early design," *Journal of Aircraft*, vol. 55, no. 5, pp. 1942–1954, 2018.

[2] C. H. Fleming and N. G. Leveson, "Improving hazard analysis and certification of integrated modular avionics," *Journal of Aerospace Information System*, vol. 11, no. 6, pp. 397–411, 2014.

[3] T. Ishimatsu, N. G. Leveson, J. P. Thomas et al., "Hazard analysis of complex spacecraft using systems-theoretic process analysis," *Journal of Spacecraft and Rockets*, vol. 51, no. 2, pp. 509–522, 2014.

[4] Z. Jiang, T. Zhao, S. Wang, and F. Ren, "A novel risk assessment and analysis method for correlation in a complex system based on multi-dimensional theory," *Applied Science*, vol. 10, article 3007, 2020.

[5] R. P. Collinson, *Introduction to Avionics System*, Springer Science & Business Media, 2017.

[6] C. R. Spizer, *Digital Avionic Handbook*, 3rd edition, pp. 22–258, CRC Press., 2015.

[7] J. B. Itier, "A380 integrated modular avionics," in *Proceedings of the ARTIST2 Meeting on Integrated Modular Avionics*, pp. 72–75, Roma, Italy, 2007.

[8] J. Anjali and W. Michael, *Model-based safety analysis final report*, NASA/CR-2006-21395, NASA Contractor Report, 2006.

[9] Y. Papadopoulos, M. Walker, D. Parker et al., "A synthesis of logic and bio-inspired techniques in the design of dependable systems," *Annual Reviews in Control*, vol. 41, pp. 170–182, 2016.

[10] Y. Papadopoulos and J. A. McDermid, "Hierarchically performed hazard origin and propagation studies," in *Computer Safety, Reliability and Security. SAFECOMP 1999*, M. Felici and K. Kanoun, Eds., vol. 1698 of Lecture Notes in Computer Science, pp. 139–152, Springer, Berlin, Heidelberg, 1999.

[11] Y. Papadopoulos, M. Walker, D. Parker et al., "Engineering failure analysis and design optimisation with HiP-HOPS," *Engineering Failure Analysis*, vol. 18, no. 2, pp. 590–608, 2011.

[12] S. Kabir, M. Walker, and Y. Papadopoulos, "Dynamic system safety analysis in HiP-HOPS with petri nets and bayesian networks," *Safety Science*, vol. 105, pp. 55–70, 2018.

[13] M. Bozzano and Y. Papadopoulos, "A model-based extension to HiP-HOPS for dynamic fault propagation studies," in *Model-Based Safety and Assessment. IMBSA 2017*, M. Bozzano and Y. Papadopoulos, Eds., vol. 10437 of Lecture Notes in Computer Science, pp. 163–178, Springer, Cham, 2017.

[14] Z. Mian, L. Bottaci, Y. Papadopoulos, and M. Biehl, "System dependability modelling and analysis using AADL and HiP-HOPS," in *Proceedings of the 14th IFAC Symposium on*

Information Control Problems in Manufacturing, pp. 1447–1652, Bucharest, Romania, 2012.

[15] Y. Papadopoulos, *Safety-Directed System Monitoring Using Safety Cases, [Ph.D. thesis]*, University of York, 2000.

[16] Z. Mian, L. Bottaci, Y. Papadopoulos, and N. Mahmud, "Model transformation for analyzing dependability of AADL model by using HiP-HOPS," *Journal of Systems and Software*, vol. 151, pp. 258–282, 2019.

[17] Z. Mian, Y. Gao, X. Shi, and C. Tang, "Semantic mapping for model transformation between AADL2 and HiP-HOPS," in *2019 4th International Conference on System Reliability and Safety (ICSRS)*, pp. 539–543, Rome, Italy, 2019.

[18] A. E. Rugina, *Dependability modelling and evaluation-from AADL to stochastic petri nets in systèmes informatiques, [Ph. D. thesis]*, Institute National Polytechnique de Toulouse, Toulouse, 2007.

[19] A. E. Rugina, K. Kanoun, and M. Kaâniche, "A system dependability Modeling framework using AADL and GSPNs," in *Architecting Dependable Systems IV*, R. Lemos, C. Gacek, and A. Romanovsky, Eds., vol. 4615 of Lecture Notes in Computer Science, pp. 14–38, Springer, Berlin, Heidelberg, 2007.

[20] A. E. Rugina, K. Kanoun, and M. Kaâniche, "The ADAPT tool: from AADL architectural models to stochastic petri nets through model transformation," in *2008 Seventh European Dependable Computing Conference*, Kaunas, Lithuania, 2008.

[21] R. B. Han and S. H. Wang, "Transformation rules from AADL to improved colored GSPN for integrated modular avionics," in *2016 11th International Conference on Reliability, Maintainability and Safety (ICRMS)*, Hangzhou, China, 2016.

[22] B. Liu, Z. Quan, and S. Wang, "IMA reconfiguration modelling and reliability analysis based on AADL," in *The 4th Annual IEEE International Conference on Cyber Technology in Automation, Control and Intelligent*, Hong Kong, China, 2014.

[23] T. Robati, A. E. Kouhen, A. Gherbi, S. Hamadou, and J. Mullins, "An extension for AADL to model mixed-criticality avionic systems deployed on IMA architectures with TTEthernet," in *1st Architecture Centric Virtual Integration Workshop (ACVI)*, Valencia, Spain, 2014.

[24] Y. Wu, W. Wang, Z. Yu, and B. Liu, "Study of Ima software dynamic reconfiguration based on AADL," *Information Technology Journal*, vol. 12, no. 22, pp. 6627–6630, 2013.

[25] J. Delange and P. Feiler, "Architecture fault modeling with the AADL error-model annex," in *2014 40th EUROMICRO Conference on Software Engineering and Advanced Applications*, Verona, Italy, 2014.

[26] P. Wang, C. X. Zhao, and F. Yan, "Research on the reliability analysis of the integrated modular avionics system based on the AADL error model," *International Journal of Aerospace Engineering*, vol. 2018, Article ID 9358461, 11 pages, 2018.

[27] T. Prosvirnova, M. Batteux, P. A. Brameret et al., "The altarica 3.0 project for model-based safety assessment," in *Proceedings of 4th IFAC Workshop on Dependable Control of Discrete Systems, DCDS 2013*, York, Great Britain, September 2013.

[28] M. Talebberrouane, F. Khan, and Z. Lounis, "Availability analysis of safety critical systems using advanced fault tree and stochastic petri net formalisms," *Journal of Loss Prevention in the Process Industries*, vol. 44, pp. 193–203, 2016.

[29] S. Kabir, K. Aslansefat, I. Sorokos, Y. Papadopoulos, and Y. Gheraibia, "A conceptual framework to incorporate complex basic events in HiP-HOPS," in *Model-Based Safety and Assessment. IMBSA 2019*, Y. Papadopoulos, K. Aslansefat, P. Katsaros, and M. Bozzano, Eds., vol. 11842 of Lecture Notes in Computer Science, pp. 109–124, Springer, Cham, 2019.

[30] S. Kabir, K. Aslansefat, I. Sorokos, Y. Papadopoulos, and S. Konur, "A hybrid modular approach for dynamic fault tree analysis," *IEEE Access*, vol. 8, pp. 97175–97188, 2020.

[31] K. Aslansefat and G. R. Latif-Shabgahi, "A hierarchical approach for dynamic fault trees solution through semi-Markov process," *IEEE Transactions on Reliability*, vol. 2019, pp. 1–18, 2019.

[32] E. G. Amparore, M. Beccuti, and S. Donatelli, "(Stochastic) model checking in Great SPNApplication and Theory of Petri Nets and Concurrency. PETRI NETS 2014," vol. 8489 of Lecture Notes in Computer Science, Springer, Cham, 2014.

[33] P. Bonet, C. M. Llad, and R. Puigjaner, "PIPE v2.5: a petri net tool for performance modelling," in *In Proceedings of 23rd Latin American conference informatics*, Costa Rica, 2007.

[34] N. J. Dingle, W. J. Knottenbelt, and T. Suto, "PIPE2: a tool for the performance evaluation of generalised stochastic petri nets," *ACM SIGMETRICS Performance Evaluation Review*, vol. 36, no. 4, pp. 34–39, 2009.

[35] Y. Lu, Y. W. Dong, X. M. Wei, and M. Xiao, "A hybrid method of redundancy system reliability analysis based on AADL models," in *2018 IEEE International Conference on Software Quality, Reliability and Security Companion (QRS-C)*, Lisbon, Portugal, 2018.

[36] J. P. Fan and T. D. Zhao, "Dispatch reliability of civil aviation simulation based on generalized stochastic petri nets (GSPN)," in *2014 10th International Conference on Reliability, Maintainability and Safety (ICRMS)*, Guangzhou, China, 2014.

[37] L. M. Almutairi and S. Shetty, "Generalized stochastic petri net model based security risk assessment of software defined networks," in *MILCOM 2017 - 2017 IEEE Military Communications Conference (MILCOM)*, pp. 545–550, Baltimore, MD, USA, 2017.

[38] D. Jana and N. Chakraborty, "Generalized stochastic petri nets (GSPN) for analysis of microgrid under uncertainities," in *2018 20th National Power Systems Conference (NPSC)*, Tiruchirappalli, India, 2018.

[39] M. Garoui, "Modeling and analysis of vehicles platoon safety in a dynamic environment based on GSPN," in *Enterprise, Business-Process and Information Systems Modeling. BPMDS 2016, EMMSAD 2016*, R. Schmidt, W. Guédria, I. Bider, and S. Guerreiro, Eds., vol. 248 of Lecture Notes in Business Information Processing, pp. 465–478, Springer, Cham, 2016.

[40] S. Kabir, M. Walker, and Y. Papadopoulos, "Quantitative evaluation of Pandora temporal fault trees via petri nets," *IFAC-Papers Online*, vol. 48, no. 21, pp. 458–463, 2015.

[41] M. A. Marsan, G. Balbo, G. Conte, S. Donatelli, and G. Franceschinis, "Modelling with generalized stochastic petri nets," *ACM SIGMETRICS Performance Evaluation Review*, vol. 26, no. 2, 1998.

[42] Y. Chu, Z. Yuan, and J. Chen, "Research on dynamic reliability of a jet pipe servo valve based on generalized stochastic petri nets," *International Journal of Aerospace Engineering*, vol. 2015, 8 pages, 2015.

[43] S. Tigane, L. Kahloul, S. Benharzallah, S. Baarir, and S. Bourekkache, "Reconfigurable GSPNs: a modeling formalism of evolvable discrete-event systems," *Science of Computer Programming*, vol. 183, article 102302, 2019.

[44] C. Watkins, "Integrated modular avionics: managing the allocation of shared intersystem resources," in *2006 IEEE/AIAA*

25TH Digital Avionics Systems Conference, Portland, OR, USA, 2006.

[45] A. R. I. N. C. Electronic Engineering Committee, *ARINC653: Avionics Application Software Standard Interface*, Aeronautical Radio, Inc, Annapolis, MD, 2006.

[46] ARINC Electronic Engineering Committee, "ARINC 664p7: Aircraft Data Network, Part 7," in *Avionics full duplex switched ethernet (AFDX) network*, Aeronautical Radio, Inc, Annapolis, MD, 2005.

[47] C. B. Watkins and R. Walter, "Comparing two industry game changers: integrated modular avionics and the iPhone," in *2009 IEEE/AIAA 28th Digital Avionics Systems Conference*, Orlando, FL, USA, 2009.

[48] R. David and H. Alla, *Discrete, Continuous, and Hybrid Petri Nets*, Springer, Berlin Heidelberg, 2005.

[49] T. Murata, "Petri nets: properties, analysis and applications," *Proceedings of the IEEE*, vol. 77, no. 4, pp. 541–580, 1989.

[50] R. Li and S. Reveliotis, "Performance optimization for a class of generalized stochastic petri nets," *Event Dynamic Systems*, vol. 25, no. 3, pp. 387–417, 2014.

[51] M. Z. Kamil, M. Taleb-Berrouane, F. Khan, and S. Ahmed, "Dynamic domino effect risk assessment using petri-nets," *Process Safety and Environmental Protection*, vol. 124, no. 2019, pp. 308–316, 2019.

[52] P. J. Haas, "Stochastic petri nets: modelling, stability, simulation," in *Proceedings of the 2004 Winter Simulation Conference*, vol. 1, pp. 101–112, 2004.

Hindawi
International Journal of Aerospace Engineering
Volume 2020, Article ID 8857821, 9 pages
https://doi.org/10.1155/2020/8857821

Research Article

Structural Optimization of the Aircraft NACA Inlet Based on BP Neural Networks and Genetic Algorithms

Zhimao Li,[1,2] Changdong Chen,[3] Houju Pei,[1] and Benben Kong[1]

[1]*College of Aerospace Engineering, Key Laboratory of Aircraft Environmental Control and Life Support, MIIT, Nanjing University of Aeronautics and Astronautics, Nanjing 210016, China*
[2]*Shanghai Aircraft Design and Research Institute, Environment Control and Oxygen System Department, Shanghai 201210, China*
[3]*AVIC Nanjing Servo Control System Co., Ltd., Nanjing 210032, China*

Correspondence should be addressed to Houju Pei; hj_pei@nuaa.edu.cn

Received 5 June 2020; Revised 1 July 2020; Accepted 9 July 2020; Published 1 August 2020

Academic Editor: Feng Qu

With the development of the increasing demand for cooling air in cabin and electronic components on aircraft, it urges to present an energy-efficient optimum method for the ram air inlet system. A ram air performance evaluation method is proposed, and the main structural parameters can be extended to a certain type of aircraft. The influence of structural parameters on the ram air performance is studied, and a database for the performance is generated. A new method of integrating the BP neural networks and genetic algorithm is used for structure optimization and is proven effective. Moreover, the optimum result of the structure of the NACA ram air inlet system is deduced. Results show that (1) the optimization algorithm is efficient with less prediction error of the mass flow rate and fuel penalty. The average relative error of the mass flow rate is 1.37%, and the average relative error of the fuel penalty is 1.41% in the full samples. (2) Predicted deviation analysis shows very little difference between optimized and unoptimized design. The relative error of the mass flow rate is 0.080% while that of the fuel penalty is 0.083%. The accuracy of the proposed optimization method is proven. (3) The mass flow rate after optimization is increased to 2.506 kg/s, and the fuel penalty is decreased by 74.595 Et kg. The BP neural networks and genetic algorithms are studied to optimize the design of the ram air inlet system. It is proven to be a novel approach, and the efficiency can be highly improved.

1. Introduction

The ram air inlet of the aircraft environmental control system ("ECS") is a key component of the air source introduction and plays a very key role in the system performance. A NACA (National Advisory Committee for Aeronautics) air inlet is one of the typical forms, designed by Davis et al. [1] in 1945. Its unique shape controls the involvement of the attached surface layer to a certain extent and increases the flow of mainstream air into the inlet using the side coiling effect, which has a unique advantage in high backpressure and high flow rate conditions. Besides, compared with other air inlets, its air pressure loss is smaller, so it is widely used. The inlet intake shape of different NACA air intakes is the same. However, the inlet position and structural parameters are different. Currently, most design of NACA air inlets follows the instruction of ESDU 86002 document [2], in which a two-dimensional surface design instruction is presented. It cannot be extended to all of the NACA shape design especially to three-dimensional shape of different aircraft. And there are no uniform standard and specification for its optimization method. Therefore, it is of practical significance to find a method for NACA air inlet optimization for the actual airplane surface. The following advances have been made in the design of an air inlet for airborne and onboard engines.

The CFD simulation technique was adopted by Surve, Wang et al., and Xiaolong et al. [3–5]. The inlet drag, total pressure recovery coefficient, and torque loss of the onboard engine were designed and calculated, and the performance of the onboard engine was improved. The optimization algorithm was introduced into the calculation by Jiang et al.

and Li et al. [6, 7], and the algorithm was proven by experiments. The structural optimization design method combining the BP neural network and genetic algorithm was proposed by Guo and Lu [8], and the value of this method in the design of parts of an aeroengine was proven by CFD simulation.

As mentioned above, the design and optimization of the inlets mainly focus on the airborne and vehicle engines, but there are few researches on the aircraft ram air inlet, and the performance evaluation criteria of the ram air inlets are different from those of the above-mentioned engines. Generally, the criterion of an air inlet of engines is the mass flow rate, while the criteria of ram air inlet performance are complicated, including total pressure recovery coefficient, mass flow rate, and aerodynamic resistance, and fuel usage is also needed to be involved. Therefore, the existing theory and method are limited for the full study of a ram air inlet.

There are many prediction methods for parameters, such as linear regression analysis, polynomial analysis based on linear regression expansion, artificial neural networks, time series analysis, least squares support vector machines, and other prediction methods. The methods of parameter optimization mainly include sample experiment optimization, simulated annealing algorithm optimization, genetic algorithm optimization, and other optimization methods. In fact, each of these methods has its own characteristics.

The combination of BP neural networks and genetic algorithms has advantages for the above problem solving. The BP neural network has an excellent nonlinear mapping ability. After sample training, the relationship between different input parameters and different output parameters can be obtained, which can solve the mapping problem of multiple structural parameters and multiple evaluation indicators. Meanwhile, the genetic algorithm overcomes the drawbacks of narrow applicability and slow convergence of traditional optimization algorithms, which can cope with discontinuous, high-dimensional, multipolar values in real processes. Accordingly, the genetic algorithm has a strong global optimization capability and can use mapping relationships to evaluate the fitness of individuals, which is applicable to the global optimization solution of structural parameters.

In this paper, an air inlet performance evaluation method for multiple performance indicators is proposed and a database of multiple structural parameters and multiple performance indicators is established. On this basis, the influence of the structural parameters of the NACA air inlet on its performance is investigated. Also, in conjunction with the artificial intelligence algorithm, the structural parameters of the air inlet are optimized and determined. Finally, the reliability of this optimization algorithm is proven by numerical calculation.

2. NACA Air Inlet Structure Parameters and Evaluation Indicators

2.1. NACA Air Inlet Structure Parameters. Before the structural optimization design, the structural parameters of the air inlet need to be decomposed to obtain the main structural parameters. A NACA ram air inlet is a common part of an air inlet for aircraft environmental control systems [9], and its structure is shown in Figure 1. Due to the influence of the opening form, when the airflow enters the inlet, a symmetrical swirling vortex is generated at the throat, which improves airflow and increases the inlet mass flow rate. The main structural parameters that affect inlet performance are slope inclination (α), throat aspect ratio (A_{wdt}), and opening length (L_1).

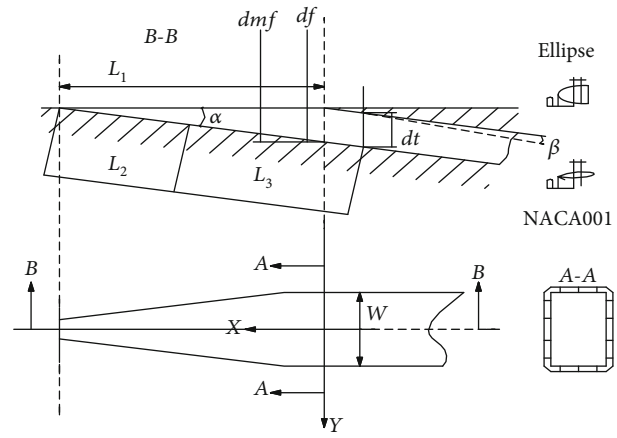

Figure 1: Diagram of a NACA ram air inlet.

2.2. NACA Air Inlet Performance Evaluation Index. The existing experience proposes that the total pressure recovery coefficient, ram recovery rate, mass flow rate, and resistance can be used as inlet performance evaluation indicators, which are mainly single indicators for the aerodynamic performance of a ram air inlet. For civil aircraft, the system weight, engine power, and system resistance should also be taken into account for a comprehensive evaluation of the system. Therefore, the fuel penalty can be regarded as an economic performance indicator for evaluating the ram inlet of the environmental control system, which should be taken into account in the design of the air inlet. Moreover, the mass flow rate is taken as the basic design requirement for the air inlet.

Therefore, the following two requirements should be involved in the optimized design: (1) guaranteed minimum fuel penalty ΔW and (2) the inlet mass flow rate M higher than the minimum mass flow rate M_d. In this paper, M_d = 2.506 kg/s.

The fuel penalty of the ram air inlet of the environmental control system consists of two aspects: the fuel penalty W_{fD} caused by the fixed system unit weight and the fuel penalty W_{fx} caused by the ram air resistance.

The fuel weight W_{fD} consumed by the fixed system unit weight W_{D} on the aircraft can be expressed as [10]

$$W_{\text{fD}} = W_{\text{D}}\left[\exp\left(\frac{C_e \cdot \tau_0 \cdot g}{K}\right) - 1\right], \tag{1}$$

where C_e is the fuel consumption ratio (kg/N/h), τ_0 is the flight time (h), g is the gravitational acceleration (m/s^2), and K is the aerodynamic mass of the aircraft.

Due to differences in fuel consumption ratios, flight time, and speed of different aircraft, the fuel penalty caused by the fixed system unit weight is defined as $W_{fD}/W_D = \exp(C_e\tau_0 g/K) - 1$, expressed as E_t. At this point, formula (1) can be written as

$$W_{fD} = W_D \cdot E_t. \tag{2}$$

The fuel penalty W_{fx} caused by aerodynamic resistance can be described as [10]

$$W_{fx} = \frac{X \cdot K}{g}\left[\exp\left(\frac{C_e \cdot \tau_0 \cdot g}{K}\right) - 1\right], \tag{3}$$

where X is the aerodynamic resistance of the ram air inlet, which is related to the mass flow rate M and the flight speed v, described as

$$X = M \cdot v. \tag{4}$$

Then, formula (3) can be expressed as

$$W_{fx} = \frac{M \cdot v \cdot K}{g} \cdot E_t. \tag{5}$$

Therefore, the total fuel penalty ΔW caused by the air inlet can be expressed as

$$\Delta W = \left(W_D + \frac{M \cdot v \cdot K}{g}\right) \cdot E_t. \tag{6}$$

3. NACA Air Inlet Optimization Design Method Based on an Artificial Intelligence Algorithm

3.1. Air Inlet Optimization Design Process. Considering that there is no clear functional relationship between the inlet structure parameters and the performance evaluation indicators, one possible solution is that a data-driven prediction model can be used to establish a functional relationship and an intelligent optimization algorithm model can be used to optimize the structural parameters of the air inlet.

This process involves the determination of optimization structural parameters and performance evaluation indicators, the acquisition of data samples, the establishment of prediction models, the establishment of optimization models, and the comparison and verification of optimization results.

3.2. The Establishment of the Air Inlet Performance Database. Data samples were acquired from numerical simulations of aircraft ram air inlet models. The data sample collection includes the design of structural parameters, the generation of parametric model and parametric grid, the batch simulation calculations, and the export of results.

In this paper, the throat aspect ratio, slope inclination, and opening length were selected by the instruction in ESDU 86002 document, which are the key structural parameters affecting the air intake performance. For sample expansion, three structural parameters were divided into six sample test values. The total sample is $6^3 = 216$, as shown in Table 1.

Table 1: Structure parameters.

Throat aspect ratio	Slope inclination (°)	Opening length (mm)
2	6	1460
2.4	6.4	1555
2.8	6.8	1650
3.2	7.2	1745
3.6	7.6	1840
4	8	1935

In this paper, the internal and external flow fields of the whole aircraft with ram inlets were calculated for 216 sets of working conditions with different aspect ratios, slope inclinations, and opening lengths and a database of aircraft air intake performance is obtained.

In order to obtain a database of inlet performance with different structural parameters, the reliability of the calculation method was verified first. The simulation was carried out by ANSYS CFX. The validation uses the DLR-F6 model, which is proven by the wind tunnel experiment conducted by the AIAA Resistance Prediction Workshop (DPW) [11, 12]. The simulation results are shown in Table 2.

It can be seen from Table 2 that when the grid number reaches 19745870, the resistance coefficient does not fluctuate much and the calculation error is less than 1%. Therefore, the k-ε turbulence model is selected in this paper. The grid type is a structured grid, and the grid number is 19745870. The velocity flow diagram of the air inlet is shown in Figure 2.

As shown in Figure 2, the ram air flow field before the entrance of the NACA inlet is uniform; after the entrance, due to the expansion angle, the flow is separated, the flow velocity in the middle is large, and the flow velocity on both sides is small; there is a vortex flow on the left and the right side of the outlet surface, and the distribution is relatively symmetrical. The vortex flow results in the strong entrainainment of the NACA inlet, which facilitates the introduction of more ram air.

The flow separation occurs at the downstream of the air inlet throat. At the same time, due to the joint influence of wing fairing and outer wing, the peripheral flow field of the air inlet has a certain side slip angle in the flow direction, which is not consistent with the axis direction of the air inlet. In addition, flow separation may also be caused by the dilated segment behind the throat. Both of these two factors affect the air inlet performance.

Further, the 216 conditions listed above were calculated to obtain the database of aircraft inlet performance with different structural parameters, and general laws of the database were analyzed, as shown in Figures 3 and 4.

In Figures 3–6, it can be seen that the fuel penalty and mass flow rate of the aircraft tend to increase monotonously with the change of the aspect ratio, slope angle, and opening length and the curvature is not fixed.

When the slope angle is large, the mass flow rate changes smoothly after the aspect ratio becomes larger than 3.5.

Table 2: Comparisons between predictions of CFX and test results.

Method	C_L	C_D	ΔC_D
Experiment	0.500	0.02950	—
Simulation calculation (grid number 6353702)	0.500	0.03094	0.000144
Simulation calculation (grid number 10694138)	0.500	0.029781	0.00031
Simulation calculation (grid number 19745870)	0.500	0.02976	0.00026
Simulation calculation (grid number 29573892)	0.500	0.02975	0.00025

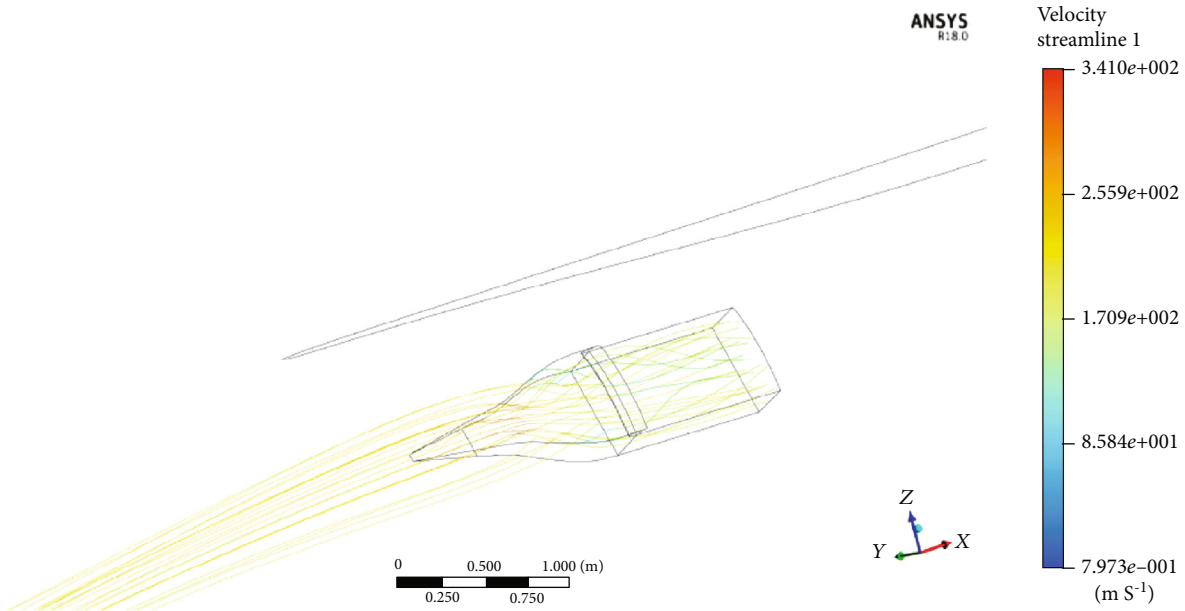

(1) Flow lines in the aircraft outflow field

(2) Flow lines in the air inlet section

Figure 2: Velocity streamline of a NACA ram air inlet.

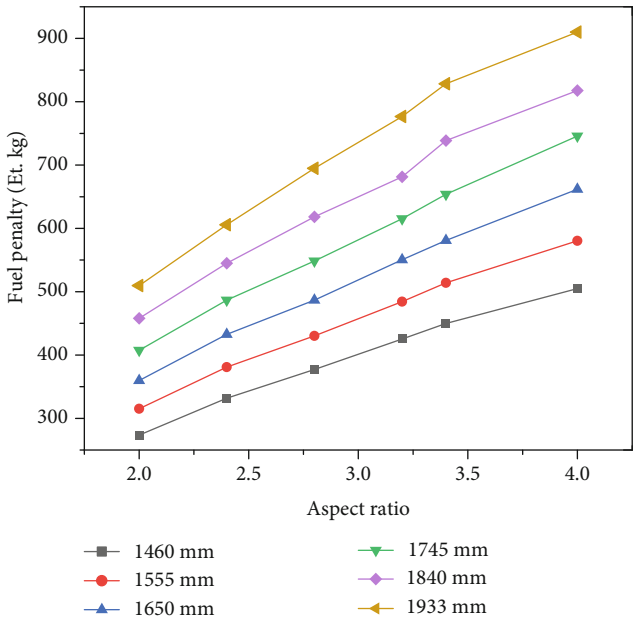

Figure 3: Fuel penalty with different aspect ratios and opening lengths at a slope angle of 6°.

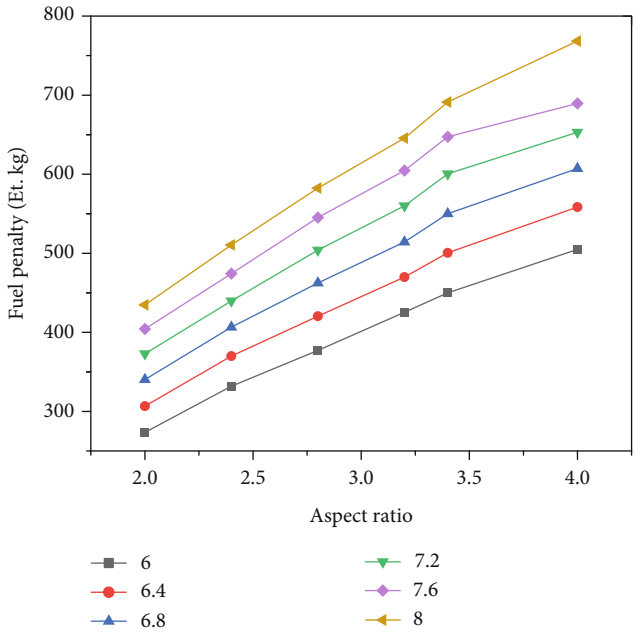

Figure 4: Fuel penalty with different aspect ratios and slope angles at an opening length of 1460 mm.

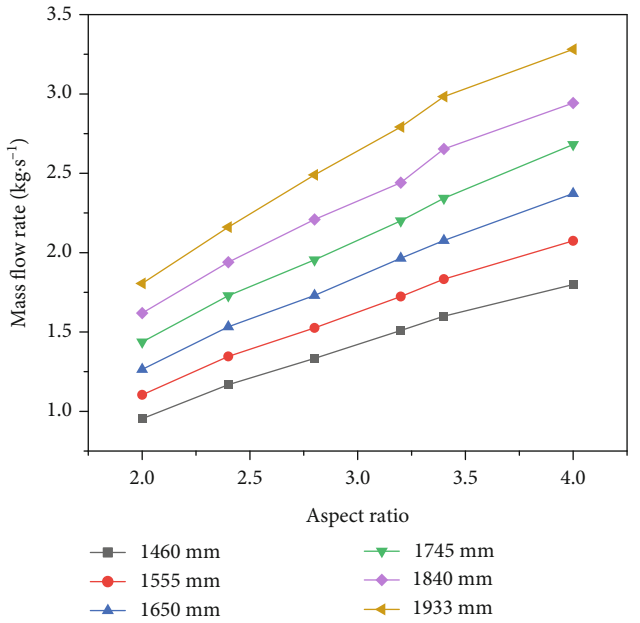

Figure 5: Mass flow rate with different aspect ratios and opening lengths at a slope angle of 6°.

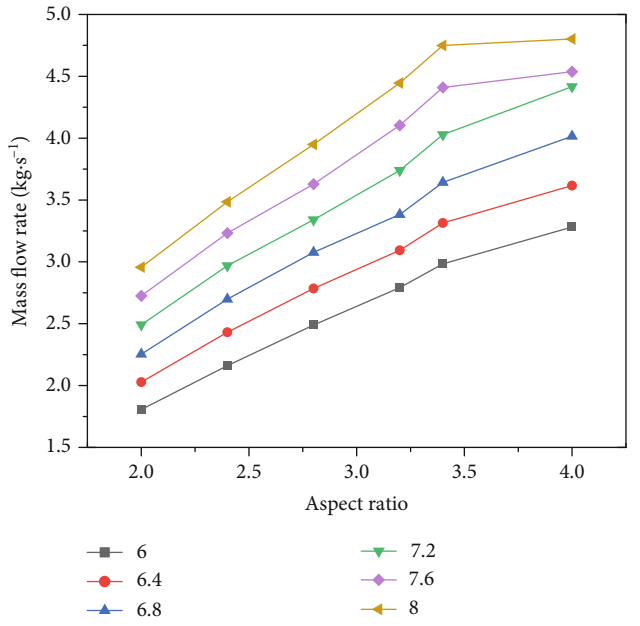

Figure 6: Mass flow rate with different aspect ratios and slope angles at an opening length of 1933 mm.

Meanwhile, it can be seen that the mass flow rate at the air inlet is relatively small in many conditions. However, these conditions do not meet the design requirements and need to be screened in the later optimization.

3.3. BP Neural Network. The BP (back propagation) neural network algorithm is a typical algorithm of artificial neural networks, which estimates the errors of each layer in the form of error back propagation [13, 14]. The BP neural network has strong nonlinear generalization capability, which can obtain the global mapping between arbitrary input variables and output variables and accurately simulate the distribution of the mass flow rate and fuel penalty. Therefore, based on the BP neural network, the data-driven prediction model was established. The mapping relationship S_{net} between the

output performance indicator aggregate S and the input structure parameters was established, and the abstract function is

$$S(M, \Delta W) = S_{\text{net}}(A_{\text{wdt}}, \alpha, L). \tag{7}$$

The topology of the BP neural network prediction model is shown in Figure 7.

The BP neural network algorithm is also known as the error back propagation algorithm for multilayer perceptron. As shown in Figure 7, the output error is gradually propagated through the implicit layer to the input layer in some form, and the error is distributed to all the units in each layer to obtain the error signal. In this process, the output error is used to estimate the error of the previous layer adjacent to the output layer, and then, the error of the previous layer is estimated by this error. The error is propagated layer by layer; in this way, the error of all other layers can be obtained.

Based on MATLAB, the BP neural network toolbox was called [15] to establish the network topology of the prediction model.

The network topology was established based on the newff function. Sample training was carried out based on the train function. Simulation was performed based on the sim function. The specific parameters of the network are shown in Table 3.

3.4. Genetic Algorithm Optimization Model. The genetic algorithm, one of the representative algorithms in the field of artificial intelligence, carries out "survival of the fittest" for individuals [16]. The genetic algorithm has a strong ability of global optimization and can use mapping relationship to evaluate the fitness of individuals, which is suitable for the global optimization of structural parameters without specific expressions.

In order to optimize the structural parameters, an optimization model was built and a range of structural parameters was given.

$$\begin{cases} \min\ \Delta W_i = S_{\text{net}}(A_{\text{wdt}}, a, L), \\ M_i = S_{\text{net}}(A_{\text{wdt}}, a, L) > M_d, \end{cases}$$

$$\begin{cases} 2 \le A_{\text{wdt}} \le 4, \\ 6 \le a \le 8^{\circ}, \\ 1460 \le L \le 1933\ \text{mm}. \end{cases} \tag{8}$$

The code of the genetic algorithm was compiled based on MATLAB, and the key parameters of the general genetic algorithm are set as shown in Table 4. In addition, if the mass flow rate of an individual is lower than the minimum mass flow rate, the fuel penalty will increase a penalty value.

3.5. Combination of the BP Neural Network and Genetic Algorithm Optimization Model. The BP neural network uses sample point data for sample training to obtain data mapping relationships. Depending on the data mapping relationship, the optimal data can be found in the global parameter range. A schematic diagram of BP neural networks and genetic algorithms is shown in Figure 8.

As shown in Figure 8, the input data of the BP neural network contains the throat aspect ratio, slope angle, opening length, fuel penalty, and mass flow rate. The output data mapping relationships are the throat aspect ratio, slope inclination, and opening length versus fuel substitution loss and mass flow. The output data mapping relationship is the relationship between the throat aspect ratio, slope angle, and opening length and fuel penalty and mass flow.

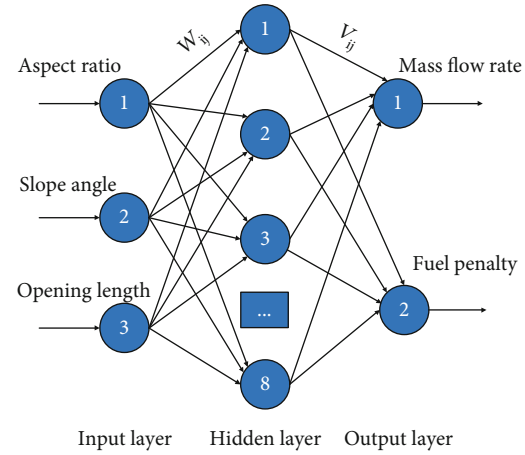

Figure 7: Topology of the BP neural network prediction model.

Table 3: BP neural network parameters.

Parameters	Settings
Number of input layer neurons	3
Number of hidden layer neurons	8
Number of output layer neurons	2
Intermediate result display period	50
Learning rate	0.01
Maximum number of iterations	10000
Target error	0.001
Hidden layer activation function	tansig
Output layer activation function	purelin
Training function	trainlm

Table 4: Genetic algorithm parameters.

Parameters	Settings
Population size	100
Iterations	2000
Chromosome length	30
Crossover rate	0.8
Mutation rate	0.1

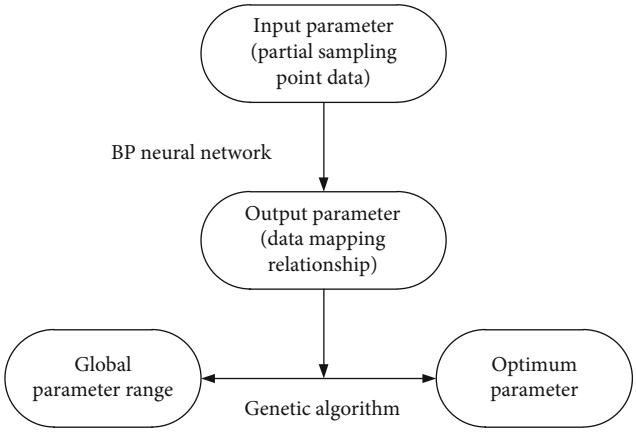

Figure 8: Schematic diagram of BP neural networks and genetic algorithms.

The global parameters solved by the genetic algorithm are the throat aspect ratio, slope angle, and opening length in a certain range. The objective is to find the combination of structural parameters whose mass flow rate is higher than the minimum value and whose fuel penalty is the lowest at the same time.

Therefore, the method of combining the BP neural network and genetic algorithm was proposed to optimize the structure of a NACA air inlet; the specific flow is shown in Figure 9.

As shown in Figure 9, a BP neural network was established based on the collected database, the network topology was determined, and data samples were input for training.

The network was expressed in terms of network weights and thresholds, which was invoked in the course of the genetic algorithm adaptation calculation. Draw support from genetic algorithms, and the optimal structural parameters of the NACA air inlet were obtained through the selection, replication, crossover, variation, and replacement of the population.

4. Optimization Results and Discussion

The database of different structural and performance parameters of the NACA air inlet is obtained by CFD simulation. The data are put into the optimization method of the BP neural network and genetic algorithm to train and optimize the samples. The data were trained and optimized by the optimization method combining the BP neural network and genetic algorithm.

Finally, the optimized NACA inlet structure parameters and the mass flow rate and fuel penalty predicted based on the BP neural network and genetic algorithm were obtained. The performance indicators calculated by ESDU and the optimized algorithm are shown in Table 5.

As shown in Table 5, the NACA inlets before and after optimization all meet the mass flow rate requirements. The fuel penalty after optimization is much lower than the one before optimization.

The comparison between the full-sample predicted value of the BP neural network and the calculated value of CFX is shown in Figures 10 and 11.

As shown in Figures 10 and 11, the penalty and mass flow rate error between predicted and calculated values by CFX are small.

The error is represented by the absolute value of mean relative error [17], in order to comprehensively describe the relative error of the test sample. In this case, the absolute values of mean relative error of the mass flow rate and fuel penalty are 1.37% and 1.41%, respectively. It can be seen that the calculation error of the optimization method adopted in this paper is reasonable.

Since the mass flow rate and fuel penalty of the NACA inlet after optimization are predicted by the BP neural network, they cannot fully represent the real performance value with the optimized structural parameters. Therefore, further CFX simulation was conducted to obtain the mass flow rate and fuel penalty at the optimized slope angle (6.813), throat aspect ratio (2.507), and opening length (1781.840). The specific results are shown in Table 6.

As can be seen from Table 6, after optimization, on the premise that the actual mass flow rate meets the design requirements, the fuel penalty is reduced by 74.595 Et kg compared with that before optimization. The error between the optimized prediction value and CFX simulation result is small, the relative error of the mass flow rate is 0.080%, and the relative error of the fuel penalty is 0.083%.

Therefore, it is proven that the BP neural network and genetic algorithm optimization model adopted in this paper is reliable.

5. Conclusion

The existing design specifications cannot fully satisfy the need of aircraft NACA inlet design because of the light weight requirements and higher inlet flow demands. Therefore, by combining the BP neural network and genetic algorithm, a set of optimization design methods which is proven to be suitable for an aircraft NACA air inlet was proposed in this paper. Besides, this method was used to optimize the air inlet of a certain type of aircraft. It can be summarized as follows:

(1) The fuel penalty and the lower limit of the inlet mass flow rate can be regarded as the two objectives in the optimization process so that not only the fuel economy has to consider the intake demand

(2) A method combining the BP neural network and genetic algorithm was proposed, and the prediction error of the mass flow rate and fuel penalty is small. The absolute values of mean relative error of the total sample mass flow rate and total sample fuel penalty are 1.37% and 1.41%, respectively

(3) Compared with the simulated value of the NACA air inlet before the optimized design, on the premise that the mass flow rate is higher than 2.506 kg/s, the fuel

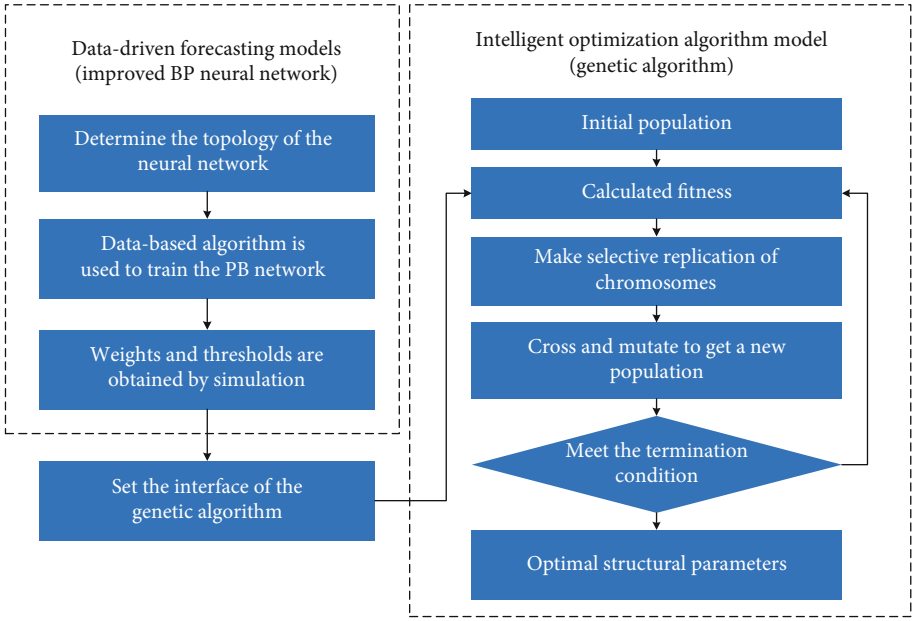

Figure 9: Flow diagram of the optimization method.

Table 5: Comparison of parameters before and after optimization.

Parameters	Before optimization	After optimization
Throat aspect ratio	3	2.507
Slope angle (°)	7	6.813
Opening length (mm)	1800	1781.840
Mass flow rate (kg·s^{-1})	2.574	2.506
Fuel penalty (kg)	772.682 Et	698.087 Et

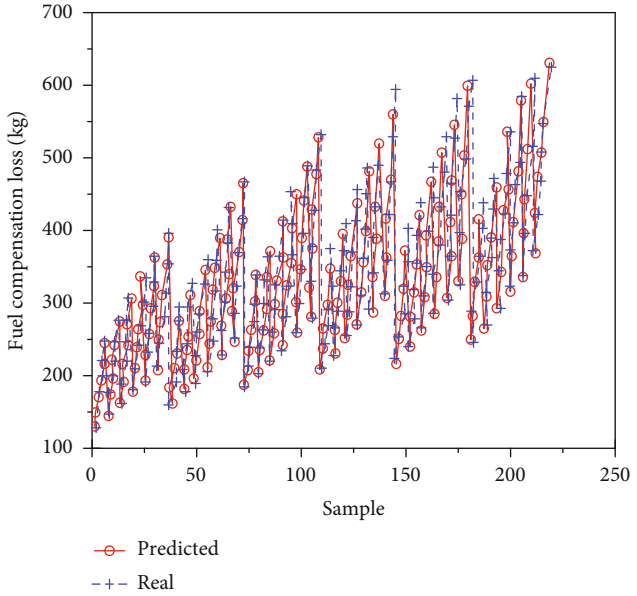

Figure 10: Comparison of predicted and calculated values of fuel penalty.

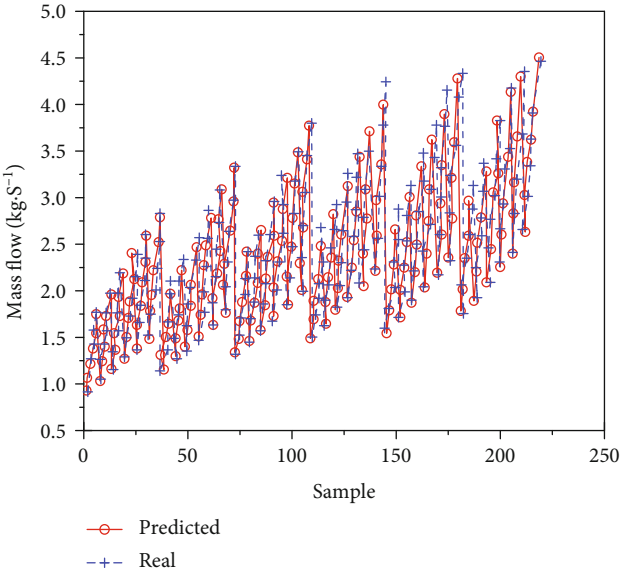

Figure 11: Comparison of predicted and calculated values of the mass flow rate.

Table 6: Performance before and after optimization.

Parameters	After optimization	CFX verification
Mass flow rate (kg·s^{-1})	2.506	2.508
Fuel penalty (kg)	698.087 Et	698.667 Et

penalty is reduced by 74.595 Et kg. This is extremely important for commercial aircraft

As a conclusion, the present method is attractive because it is effective for solving optimization design of the NACA

inlet. Therefore, it is promising to be extended to a practical aircraft design process.

Data Availability

The data used to support the findings of this study are available from the corresponding author upon request.

Conflicts of Interest

We declare that we do not have any commercial or associative interest that represents a conflict of interest in connection with the work submitted.

Acknowledgments

This study was supported by the Research Fund of Key Laboratory of Aircraft Environment Control and Life Support, MIIT, Nanjing University of Aeronautics and Astronautics (Grant No. KLAECLS-E-202001).

References

[1] X. Li, "Technical status of submerged inlet," *Journal of Fuzhou University: Natural Science Edition*, vol. 6, pp. 61–66, 2001.

[2] A. Lombardi, D. Ferrari, and L. Santos, "Aircraft air inlet design optimization via surrogate-assisted evolutionary computation," in *Evolutionary Multi-Criterion Optimization. EMO 2015*, vol. 9019 of Lecture Notes in Computer Science, pp. 313–327, 2015.

[3] A. K. Surve, "Knowledge based inlet port design: a simple graphical method to design inlet port and flow simulation," in *2016 International Conference on Automatic Control and Dynamic Optimization Techniques (ICACDOT)*, pp. 829–834, Pune, India, 2017.

[4] X. Wang, G. Jiang, and C. Zhou, "Optimization design for the two-dimensional contour of the ramjet engine inlet," in *2008 Asia Simulation Conference - 7th International Conference on System Simulation and Scientific Computing*, pp. 1197–1200, Beijing, China, 2008.

[5] Y. Xiaolong, H. Ming, and L. Biao, "Optimization of intake and exhaust system of a gasoline engine based on genetic algorithm," in *2009 IEEE 10th International Conference on Computer-Aided Industrial Design & Conceptual Design*, pp. 2100–2104, Wenzhou, China, 2009.

[6] A. Jiang, J. Huang, J. Wang, Q. Ding, Z. Jiang, and G. Huang, "Optimal design of intake system mufflers in engine based on single and multi-objective optimization," in *2008 7th World Congress on Intelligent Control and Automation*, pp. 8733–8737, Chongqing, China, 2008.

[7] S. Li, S. Tang, and D. Gao, "An integrated optimization for hypersonic inlet design based on python," in *2010 International Conference On Computer Design and Applications*, pp. V4–64, Qinhuangdao, China, 2010.

[8] H. Guo and Z. Lu, "Structural optimization design based on BP neural network and genetic algorithm," *Journal of Aeronautical Dynamics*, vol. 18, no. 2, pp. 216–220, 2003.

[9] Y. Xue, Z. Song, and Z. Xu, "Design method of NACA inlet for civil aircraft," *Science and Technology Information*, vol. 6, pp. 187–189, 2014.

[10] Aircraft design manual, *Aircraft Design Manual Volume 15, Life Support and Environmental Control System Design*, Aviation Industry Press, Beijing:, China, 1999.

[11] K. R. Laflin, S. M. Klausmeyer, T. Zickuhr et al., "Data summary from second AIAA computational fluid dynamics drag prediction workshop," *Journal of Aircraft*, vol. 42, no. 5, pp. 1165–1178, 2005.

[12] D. Levy, K. Laflin, E. Tinoco et al., "Summary of data from the fifth AIAA CFD drag prediction workshop," in *51st AIAA Aerospace Sciences Meeting including the New Horizons Forum and Aerospace Exposition*, p. 46, Grapevine, TX, USA, 2013.

[13] X. U. Donghui, Y. Xiong, S. Yan, W. Li, G. Wu et al., "Forecast study of gasoline engine intake flow based on BP neural network," *Journal of Kunming University of Science & Technology*, vol. 41, 2016.

[14] L. Yu, W. Heping, and P. Runyan, "Two-dimensional stochastic airfoil optimization design method based on neural networks," *Transactions of Nanjing University of Aeronautics and Astronautics*, vol. 28, no. 4, pp. 324–330, 2011.

[15] Q. Dai and D. Zhao, "Training and simulation on gear position decision for vehicle based on optimal algorithm of BP network," *Journal of Mechanical Engineering*, vol. 38, no. 11, pp. 124–127, 2002.

[16] P. Wang, S. Zheng, and G. Wu, "Multidisciplinary design optimization of vehicle body structure based on collaborative optimization and multi-objective genetic algorithm," *Journal of Mechanical Engineering*, vol. 47, no. 2, pp. 102–108, 2011.

[17] G. Haitao, Y. Lin, Z. Hu, J. Yu et al., "Optimization method for wing design of underwater glider based on agent model," *Chinese Journal of Mechanical Engineering*, vol. 45, no. 12, pp. 7–14, 2009.

Hindawi
International Journal of Aerospace Engineering
Volume 2020, Article ID 2813856, 10 pages
https://doi.org/10.1155/2020/2813856

Research Article

Dynamic Aerothermal Analysis of a Cone-Cylinder Flight Body

Jun Zhang, Guangchen Jia, Sibanda Gibson Mkumbuzi, and Yu Wu

College of Engineering Science and Technology, Shanghai Ocean University, Shanghai 201306, China

Correspondence should be addressed to Jun Zhang; zhangjun@shou.edu.cn

Received 29 January 2020; Revised 30 June 2020; Accepted 4 July 2020; Published 21 July 2020

Academic Editor: Feng Qu

Exploring the aerothermal characteristic of a flight body has great military applications in tracking, locating, thermal protection, and infrared stealth technologies. Available studies are mostly focused on the transient aerothermal characteristics of vehicles in some specific flight datum, which are not able to satisfy the requirements in real-time tracking for an infrared system. This paper probes into a method of dynamic thermal analysis of a cone-cylinder flight body with a high spinning speed. Firstly, a theoretical model for analyzing the dynamic aerothermal characteristics is established using the thermal node-network method. Then, trajectory datum and the convective heat-transfer coefficients are solved simultaneously. Besides, the trajectory datum in supersonic, transonic, and subsonic regimes is separately defined as the boundary conditions, and fluid-thermal analysis methods are implemented by a combination of sliding mesh and multicoordinate approaches. Finally, the flow characteristics are analyzed and compared with disregarding the rotational speed. The results demonstrate that there are significant differences between the two cases, especially at the high-speed regimes. This study further confirms that it is essential to conduct the aerothermal analysis from a dynamic point of view, and taking the impacts of coupling motion into account is also of vital importance.

1. Introduction

For flight vehicles, aerothermal responses are crucial in the testing of flight parameters for an infrared radiation tracking measurement system, such as coordinate, attitude, and yaw [1–4]. Furthermore, aerothermal analysis methods are also essential to design the thermal protection structure and infrared stealth technology [5–9]. However, it is hard to accurately assess the aeroheating characteristics due to physical uncertainties and time-varying properties. In the past few decades, a series of numerical methods to estimate the aerothermal characteristics for hypersonic vehicles were proposed [10–16]. Knight et al. [17–19] appraised the capability for CFD simulation of hypersonic shock wave laminar boundary layer interaction for a double wedge model and compared with experimental heat transfer and schlieren visualization. Zheng and Qiu [20] performed the uncertainties in aerodynamic force and heating characteristics of the wing of a hypersonic vehicle accounting for uncertain-but-bounded geometric parameters. Ahmed and Qin [21–25] explored extensive research on a spiked blunt body. They investigated the airflow over the conical, disk, and flat spiked bodies and analyzed the flow asymmetry around axisymmetric spiked blunt bodies at hypersonic regimes. Qin et al. [26] conducted a loosely coupled fluid-thermal method to explore the aerodynamic thermal responses of a spiked blunt in a hypersonic regime and relevant flow variation.

Unfortunately, researchers have mainly focused on the transient aerodynamic heating of vehicle in some specific flight states [27–29]. However, aeroheating characteristics on the surface of vehicles are not only determined by the current flight state but also related closely to the heat transfer environment during the flight, which is a progressive, lasting, and dynamic process [30]. Therefore, the results of the transient thermal analysis were inevitably deviated from a practical situation, which cannot be used for real-time tracking and monitoring of the IR detecting system [31]. For example, Duda [32] formulated an effective method which can be employed to calculate the transient heat fluxes, and the algorithms were used to assess the transient temperature distribution in a whole component based on measured temperatures in selected points on the component surface.

Research on the real-time infrared radiation imaging simulation method of aircraft skin with aerodynamic heating effect, Li et al. [33] employed a dynamic simulation method to carry out the research of infrared radiation (IR) characteristics of an aircraft during the flight, and the aeroheating model and environmental radiation model were established for solving the heat balance equations.

Additionally, high-speed spinning is the major mode to maintain flying stability for some vehicles, but related to the aeroheating characteristics for a flight body with coupling motion of precession, spinning, and pitching is limited. Particularly, the effects of spinning are often neglected. For example, Silton [34] adopted the CFD method to analyze the flow behaviors for a flying projectile under different velocities and attack angles, but the rotational speed was ignored. Although the simulated values of drag and lift coefficients were basically consistent with the calculated data of semiempirical formulas and experiments, there was a remarkable deviation between the Magnus force and moment with the experimental results. On the contrary, James [35] investigated the flow characteristics of airflow around the M910 projectile under different rotating speeds. The simulated results acquired by employing the RANS/LES mixed turbulence model were in good accordance with the experimental values in subsonic and transonic conditions.

Therefore, the dynamic aerothermal characteristics of the flight body in coupled motions of precession, spinning, and pitching are necessary studies. In this article, dynamic aerothermal related to the surface of a cone-cylinder spinning flight body is reconstructed using updated modeling approaches. Firstly, the six degrees of freedom (6-DOF) trajectory model is established, and the motion characteristics are analyzed at different launch conditions. Then, the trajectory datum and the convective heat-transfer coefficients are simultaneously solved by the Runge-Kutta method, and the influencing factors are also analyzed.

2. 6-DOF Trajectory Model

A kind of spinning projectile is taken as the research object to investigate the continuous aeroheating characteristics on the surface of a flight body in the coupled motions of precession, spinning, and pitching. The simplified structural model is depicted in Figure 1; the lengths of the conical section and the cylindrical section are, respectively, indicated by L_1 and L_2. The diameter of the cylindrical section is d.

The 6-DOF kinetic model is established by the exterior ballistic theory to describe the movement regularities of the cone-cylinder spinning flight body. The modeling procedures are listed below: Firstly, the reference coordinate systems are created, including the ground coordinate, datum coordinate, ballistic coordinate, body coordinate, and body-axis coordinate systems. Then, the dynamic loads are analyzed, including the gravity, drag, lift, Magnus force, static moment, equatorial and polar damping moment, and Magnus moment.

Based on the general theoretical analysis above, the kinematic equations and the kinetic equations are derived

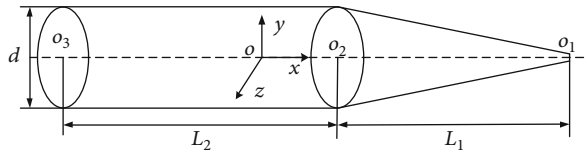

Figure 1: Geometric model.

according to the momentum theorem and mass center motion theorem in the ballistic coordinate system.

$$\begin{cases} m\dfrac{d\mathbf{v}}{dt} = \sum \mathbf{F}_x, \\ m\mathbf{v}\dfrac{d\psi_1}{dt}\cos\psi_2 = \sum \boldsymbol{F}_y, \\ m\mathbf{v}\dfrac{d\psi_2}{dt} = \sum \mathbf{F}_z, \end{cases} \tag{1}$$

$$\begin{cases} \dfrac{dx}{dt} = v\cos\psi_1\cos\psi_2, \\ \dfrac{dy}{dt} = v\sin\psi_1\cos\psi_2, \\ \dfrac{dz}{dt} = v\sin\psi_2. \end{cases} \tag{2}$$

Similarly, the kinetic equations and kinematic equations are derived in accordance with the theorem of momentum moment in the body-axis coordinate system.

$$\begin{cases} \dfrac{d\boldsymbol{\omega}_\xi}{dt} = \dfrac{1}{C}\sum \mathbf{M}_\xi, \\ \dfrac{d\boldsymbol{\omega}_\eta}{dt} = \dfrac{1}{A}\sum \mathbf{M}_\eta - \dfrac{C}{A}\omega_\xi\omega_\zeta + \boldsymbol{\omega}_\zeta^2\tan\varphi_2 + \dfrac{A-C}{A}\beta_1\phi'', \\ \dfrac{d\boldsymbol{\omega}_\zeta}{dt} = \dfrac{1}{A}\sum \mathbf{M}_\zeta + \dfrac{C}{A}\boldsymbol{\omega}_\xi\boldsymbol{\omega}_\eta - \boldsymbol{\omega}_\eta\boldsymbol{\omega}_\zeta\tan\varphi_2 + \dfrac{A-C}{A}\beta_2\phi'', \end{cases} \tag{3}$$

$$\begin{cases} \dfrac{d\varphi_1}{dt} = \dfrac{\omega_\zeta}{\cos\varphi_2}, \\ \dfrac{d\varphi_2}{dt} = -\omega_\eta, \\ \dfrac{d\phi}{dt} = \omega_\xi - \omega_\zeta\tan\varphi_2. \end{cases} \tag{4}$$

Accordingly, the 6-DOF trajectory model can be obtained by simultaneous equations (1), (2), (3), and (4) and constraint equations (5).

$$\begin{cases} \sin\delta_1 = \dfrac{\cos\varphi_2}{\cos\delta_2}\sin(\varphi_1 - \psi_1), \\ \sin\delta_2 = \cos\psi_2\sin\varphi_2 - \sin\psi_2\cos\varphi_2\cos(\varphi_1 - \psi_1), \end{cases} \tag{5}$$

where x, y, z are the mass center coordinates; $\mathbf{F}_x$, $\mathbf{F}_y$, $\mathbf{F}_z$ are the force components in the ballistic coordinate system;

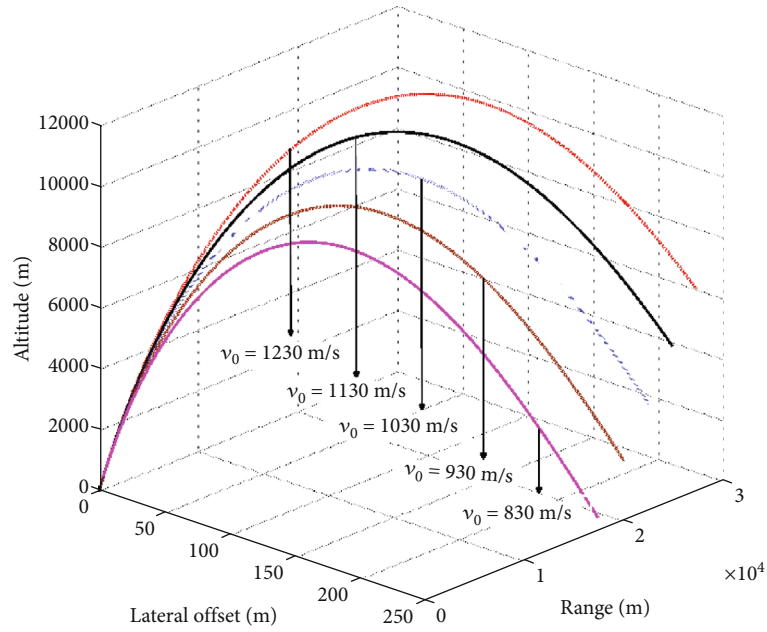

Figure 2: Trajectory curves at different initial velocities.

$\mathbf{M}_\xi$, $\mathbf{M}_\eta$, $\mathbf{M}_\zeta$ are the moment components that of acting on the projectile in the body-axis coordinate system; $\boldsymbol{\omega}_\xi$, $\boldsymbol{\omega}_\eta$, $\boldsymbol{\omega}_\zeta$ are the components of angular speed.

3. Theoretical Model of Aerodynamic Heating

3.1. Surface Element Division. The domain decomposition and surface element division are essential to derive the theoretical model. In this paper, the node-network method is proposed to generate the surface elements and take the center of each element as a compute node. The cone-shaped angle α is equally separated into n parts, and the fan-shaped radius R is evenly divided into n_1 parts. Then, according to the rules of equal areas, the area of a surface panel Δs and R_i is, respectively, expressed as

$$R_i = \sqrt{\frac{iR^2}{n_1}}, \quad i = (1, n_1), \tag{6}$$

$$\Delta s = \frac{\pi d R}{2 n n_1}. \tag{7}$$

The cylindrical surface is evenly divided into n_2 parts in an axial direction, and the division numbers are identical to the cone-shaped angle in a radial direction. For equalizing the area of the surface panel, n_2 yields

$$n_2 = \frac{2 n_1 L_2}{\sqrt{L_1 + \left(d^2/4\right)}}. \tag{8}$$

In the body coordinate system, column coordinates of node (i, k) and normal vectors of the surface panel on the conical surface are expressed as

$$\begin{cases} r(i,k) = \dfrac{d}{2R} \times \sqrt{\dfrac{i-1}{2n_1} R^2 + \dfrac{i}{2n_1} R^2}, \\ \varphi(i,k) = \dfrac{2\pi}{n} k, \\ z(i,k) = -\dfrac{L_1}{R} \times \sqrt{\dfrac{i-1}{2n_1} R^2 + \dfrac{i}{2n_1} R^2} + L_1 + L_2, \end{cases} \tag{9}$$

$$\mathbf{n}_i = \left[\frac{L_1}{R} \cos\left(\frac{2\pi}{n} k\right), \frac{L_1}{R} \sin\left(\frac{2\pi}{n} k\right), \frac{d}{2R}\right]. \tag{10}$$

Similarly, the column coordinates of node (j, k) and normal vectors of the surface panel on the cylindrical surface are expressed as

$$\begin{cases} r(j,k) = \dfrac{d}{2}, \\ \varphi(j,k) = \dfrac{2\pi}{n} k, \\ z(j,k) = \dfrac{L_2}{n_2}(m_1 - j - 1) + \dfrac{L_2}{2n_2} + L_2, \end{cases} \tag{11}$$

$$\mathbf{n}_j = \left[\cos\left(\frac{2\pi}{n} k\right), \sin\left(\frac{2\pi}{n} k\right), 0\right]. \tag{12}$$

3.2. Convective Heat Transfer Model. In this section, a theoretical model for solving the convective heat transfer coefficient on the surface of the flight body will be constructed from the theory of heat transmission. For taking the impacts of spinning speed into account, the absolute velocity in the rotating coordinate system is assumed to be the flight velocity; then, according to the velocity synthesis theorem,

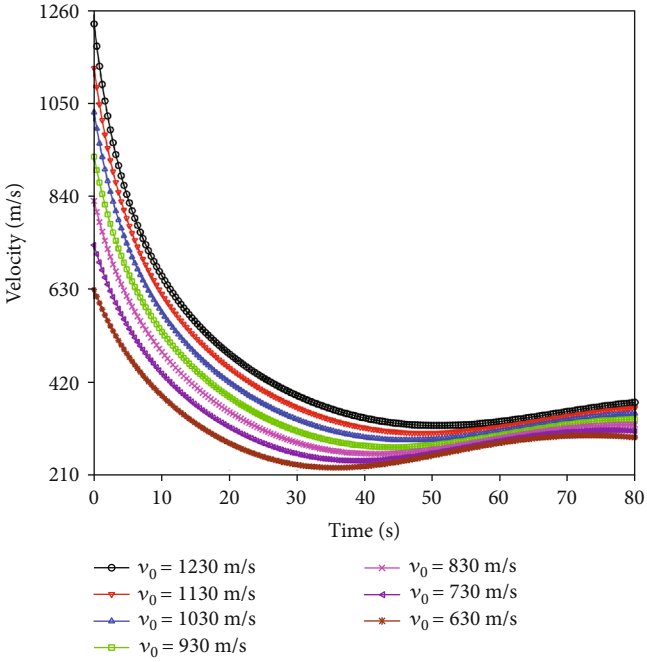

Figure 3: Velocity at different initial velocities.

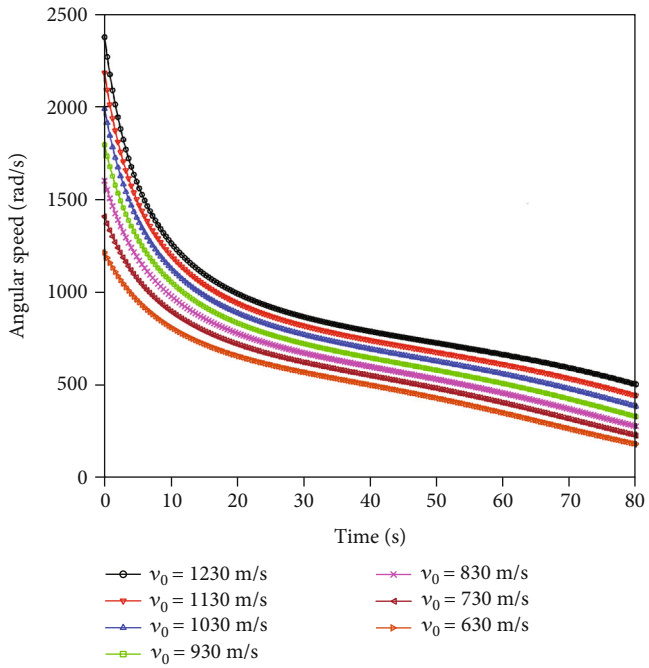

Figure 4: Angular speed at different initial velocities.

$$\mathbf{u} = \mathbf{v} + \mathbf{w} \times \mathbf{r}, \tag{13}$$

where $\mathbf{u}$ is the velocity vector in the rotating coordinate system, $\mathbf{v}$ is the velocity vector in the inertial coordinate system, and $\boldsymbol{\omega}$ is the angular speed vector. The initial angular speed is defined as

$$\boldsymbol{\omega}_0 = \frac{2\pi \mathbf{v}_0}{\eta d}. \tag{14}$$

If the standard-sea-level atmospheric parameters are regarded as the airflow parameters of the projectile at the launch position, and the relations between temperature, density, and pressure of the freestream can be, respectively, expressed as

$$T_\infty = 288.15 - \frac{65}{10000} y, \tag{15}$$

$$\rho_\infty = 1.225 \left(\frac{T_\infty}{288.15} \right)^{4.2558}, \tag{16}$$

$$P_\infty = 101325 \left(\frac{T_\infty}{288.15} \right)^{5.2558}. \tag{17}$$

The adiabatic wall temperature T_0 and the recovery temperature T_r are formulated as

$$T_0 = T_\infty \left(1 + \frac{\kappa - 1}{2} Ma_\infty^2 \right), \tag{18}$$

$$T_r = T_\infty \left(1 + \gamma \frac{\kappa - 1}{2} Ma_\infty^2 \right), \tag{19}$$

where y is the flight altitude and γ is the temperature recovery coefficient. When the flow is laminar, $\gamma = \sqrt{Pr}$, otherwise, $\gamma = \sqrt[3]{Pr}$.

According to the fluid mechanics and heat-transfer theories, the local Nusselt number can be approximately substituted for calculating the forced convection heat transfer on a flat plate, when the high-speed airflow is passing over the cylindrical surface longitudinally.

$$\begin{cases} \mathrm{Nu}_{i,v}^* = 0.332 \times \left(\mathrm{Re}_{i,v}^* \right)^{1/2} \left(\mathrm{Pr}^* \right)^{1/3}, & \mathrm{Re}_{i,v}^* \le 5 \times 10^5, \\ \mathrm{Nu}_{i,v}^* = 0.0296 \times \left(\mathrm{Re}_{i,v}^* \right)^{4/5} \left(\mathrm{Pr}^* \right)^{1/3}, & 5 \times 10^5 < \mathrm{Re}_{i,v}^* \le 10^7, \\ \mathrm{Nu}_{i,v}^* = 0.185 \times \left(\mathrm{Re}_{i,v}^* \right) \left(\lg\ \mathrm{Re}_{i,v}^* \right)^{-2.584} \left(\mathrm{Pr}^* \right)^{1/3}, & 10^7 < \mathrm{Re}_{i,v}^* \le 10^9, \end{cases} \tag{20}$$

where $\mathrm{Nu}_{i,v}^*$, Pr^*, $\mathrm{Re}_{i,v}^*$ are the local Nusselt number, Prandtl number: $\mathrm{Pr}^* = \mu^* c_p^* / \lambda^*$, and Reynolds number: $\mathrm{Re}_{i,v}^* = \rho^* u x / \mu^*$; x_i, λ^*, and μ^* are the distance from a compute node to the warhead, the thermal conductivity, and the viscosity coefficient.

$$\lambda^* = 2.72 \times 10^{-4} \left(T^* \right)^{4/5}, \tag{21}$$

$$\mu^* = 2.27 \times 10^{-8} \frac{\left(T^* \right)^{3/2}}{T^* + 198.6}. \tag{22}$$

It is known that the compressible flow theory cannot be used in predicating the aerodynamic heat flux using an implicit function with the given physical quantity. In order to solve the problem, a reference temperature method that calculates the boundary-layer parameters in the flow field is proposed. The transport and thermodynamic properties are

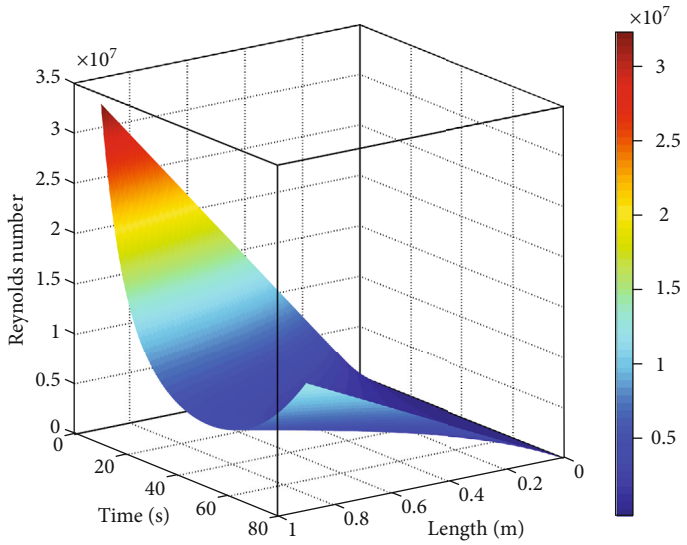

Figure 5: 3-D distribution of the Reynolds number.

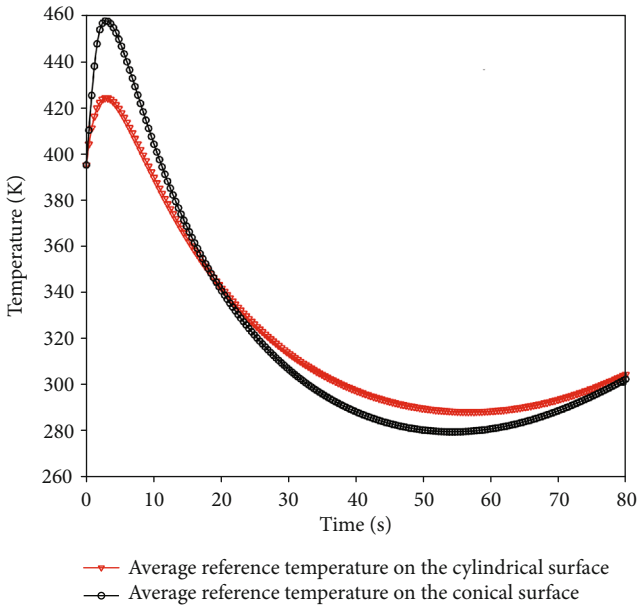

Figure 6: Average reference temperatures.

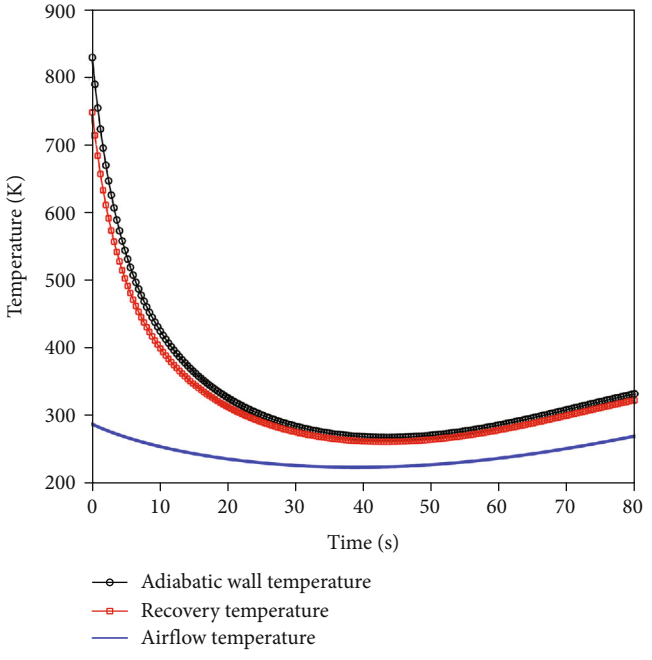

Figure 7: Adiabatic wall, recovery, and airflow temperature.

evaluated at the reference temperature (T^*) which indicates positions inside the boundary layer [22].

$$T^* = T_\infty + 0.5(T_w - T_\infty) + 0.22(T_r - T_\infty). \tag{23}$$

According to the theory of heat transmission, a relation between the local Nusselt number and the heat-transfer coefficient is defined as

$$\mathrm{Nu}^*_{i,v} = \frac{h^*_i x_i}{\lambda^*}. \tag{24}$$

Then, the coefficient of convection heat transfer on the cylindrical surface can be expressed as

$$\begin{cases} h^*_{i,c} = 0.332 x_i^{-1/2} (\mu^* c^*)^{1/3} (\lambda^*)^{2/3} \left(\dfrac{u\rho^*}{\mu^*}\right)^{1/2}, & \mathrm{Re}^*_{i,v} \le 5 \times 10^5, \\ h^*_{i,c} = 0.0296 x_i^{-1/5} (\mu^* c^*)^{1/3} (\lambda^*)^{2/3} \left(\dfrac{u\rho^*}{\mu^*}\right)^{4/5}, & 5 \times 10^5 < \mathrm{Re}^*_{i,v} \le 10^7, \\ h^*_{i,c} = 0.185 u\rho^* (\mu^*)^{-2/3} (c^*)^{1/3} (\lambda^*)^{2/3} \left(\lg \dfrac{u\rho^* x_i}{\mu^*}\right)^{-2.584}, & 10^7 < \mathrm{Re}^*_{i,v} \le 10^9. \end{cases} \tag{25}$$

The coefficient of convection heat transfer on the conical surface can be approximately calculated by the circle theorem of hydrodynamics [31].

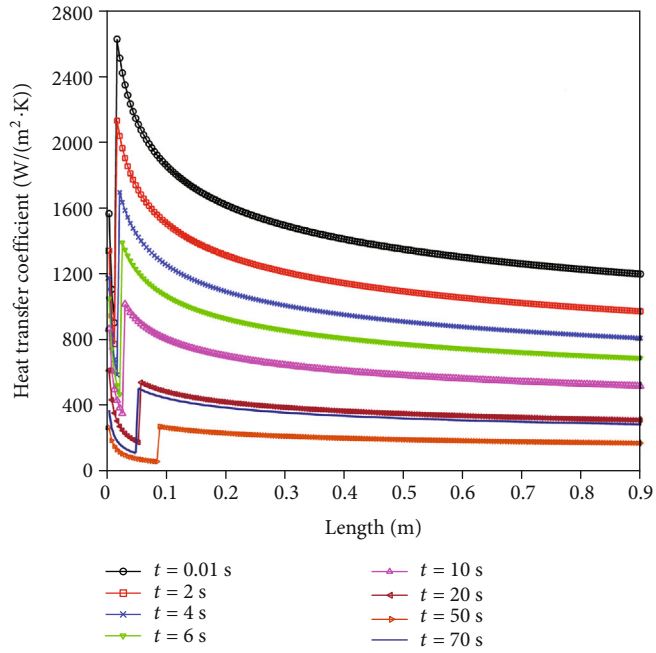

Figure 8: Transient heat transfer coefficients.

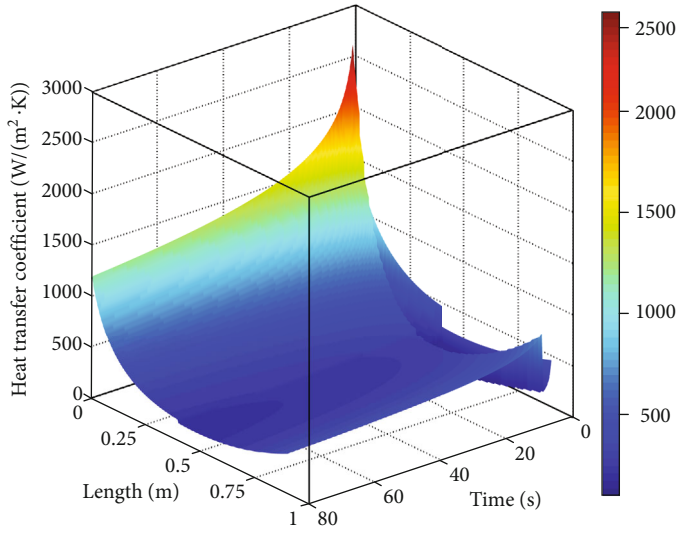

Figure 9: Convection heat transfer coefficient.

$$\begin{cases} h_{i,\mathrm{p}}^{*} = 0.332\sqrt{3}x_i^{-1/2}(\mu^{*}c^{*})c^{*1/3}(\lambda^{*})^{2/3}\left(\dfrac{u\rho^{*}}{\mu^{*}}\right)^{1/2}, & \mathrm{Re}_{i,v}^{*} \le 5\times 10^{5}, \\ h_{i,\mathrm{p}}^{*} = 0.03481x_i^{-1/5}(\mu^{*}c^{*})^{1/3}(\lambda^{*})^{2/3}\left(\dfrac{u\rho^{*}}{\mu^{*}}\right)^{4/5}, & \mathrm{Re}_{i,v}^{*} > 5\times 10^{5}. \end{cases} \tag{26}$$

4. Theoretical Calculation and Discussion

4.1. Trajectory Calculation. The primary data for trajectory calculation is shown below: the lengths of conical and cylindrical sections are 400 mm and 500 mm. The cylindrical diameter is 155 mm, and the mass is 46.5 kg. The distance from the center of mass to the warhead is 550 mm. The launch velocity, shot angle, and flight time are 1030 m/s, 45°, and 80 s, respectively. The equatorial moment of inertia is 1.814 kg•m^2, and the pole moment of inertia is 0.163 kg•m^2. The Runge-Kutta method is adopted to simultaneously solve the 6-DOF trajectory model and the aerodynamic heat transfer model, and the ballistic parameters and the heat-transfer coefficients with flight time can be obtained synchronously. Figure 2 presents the trajectory curves at different launch velocities, where the x, y, and z, respectively, indicate the range, flight altitude, and lateral offset. The lateral offset is caused by the gyroscopic orientation effects and gravitational deflection in the trajectory tangent.

Figures 3 and 4, respectively, show the flight velocity and spinning speed at different initial velocities. It is shown that the velocity conforms to decrease exponentially in ascending order. Yet at the parabola apexes, there is not the minimum before the air resistance acceleration is greater than the component of the gravity acceleration in the vertical direction. Moreover, the velocity approaches the minimum when the center of mass acceleration is zero, and then, it starts to rise reversely in the terminal trajectory. Thru comparison, it can be found that the velocity in the ascending period is greater than that in the descending at the same flight altitude. Besides, the faster the initial velocity is, the quicker the attenuation rates will be, and the attenuation rate of angular speed in the ascending period is faster than in the descending. It is known that the ratio of flight velocity and rotational speed approaches the minimum in the launch position, and the peak appears at the parabola apexes, yet the ratio starts to drop as the velocity is increasing in the terminal trajectory.

4.2. Dynamic Heat-Transfer Coefficients. Figure 5 presents the 3-D distribution of the Reynolds number. As shown in Figure 6, the average reference temperatures on the cylindrical surface and conical surface can be obtained.

From the results, each compute node corresponds to a Reynolds number and a reference temperature, and the maximum Re is about 3.3×10^7, which covers the calculation range from laminar to turbulence flow. In the first 20 seconds of the trajectory, the average reference temperature of the conical part is significantly higher than that of the cylindrical part, especially in a short time after launching, but the temperature attenuation is also faster. After 20 seconds, the average reference temperature of the conical part is lower than that of the cylindrical part.

Figure 7 presents the adiabatic wall temperature, recovery temperature, and airflow temperature. As shown in Figure 8, the transient heat transfer coefficients on the surface of the flight body can be obtained. From the results, the trends of adiabatic wall temperature and recovery temperature are basically consistent with the flight velocities, but the change extents are relatively different. The differences between adiabatic wall temperature and recovery temperature are mainly reflected in the first 20 seconds of the trajectory. The airflow temperature is first to decrease and then increase with the change in flight altitude.

Figure 9 presents the 3-D distribution of the convection heat transfer coefficient on the surface of the flight body. The results demonstrate that the heat-transfer coefficient is changed similarly with flying velocity, but the extent is discrepant. Firstly, the heat-transfer coefficient decreases rapidly and then increases until reaching a maximum, after it slowly drops off, and the former two processes that have steep gradients are concentrated in the warhead area. For the cone-shaped part, the coefficient of convection heat transfer is proportional to the square root of the velocity in laminar conditions, while the ratio is 4/5 in the turbulent flow conditions. Accordingly, the coefficient of convection heat transfer reaches a maximum at the moment of launching, and then, it drops rapidly in the terminal trajectory. Apparently, the coefficient of convection heat transfer fluctuation increases by a small fraction in the midcourse of trajectory, which is responsible for the laminar-turbulent transition.

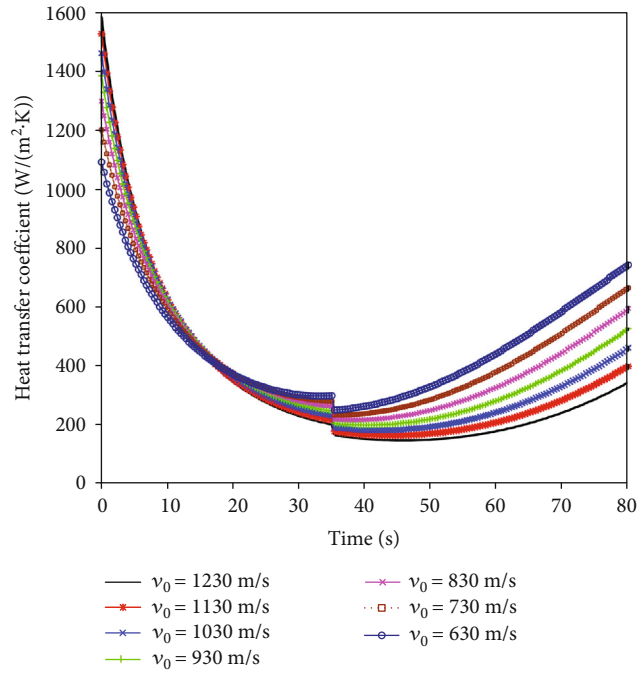

Figure 10: Average coefficients at different launch velocities.

To get the effects of launch conditions on the coefficient of convection heat transfer, the influencing factors which include the launching velocity, spinning speed, and launching angle are analyzed, as shown in Figures 10–12. It can be found from the calculation results that the average heat-transfer coefficient increases with launching velocity in the first half of the trajectory, and the decrement grows rapidly at the same time. However, the coefficient is inversely proportional to the initial velocities during the second half of the trajectory, and the launching angle yields a similar tendency. Although the smaller launching angle will lead to more serious aerodynamic heating, it will not be reflected until the body has been launched for a short time. Furthermore, the effects of spinning speed are more noticeable at the high-speed stage, yet the effects will be weakened gradually with a reduction of velocity.

5. Conclusions

In this article, dynamic aerothermal characteristics on the surface of a cone-cylinder spinning flight body are reconstructed using updated modeling approaches, and the thermal node-network method is successfully applied for predicting the aerothermal environment of the body coupling motion of precession, spinning, and pitching. The exterior trajectory datum and the coefficient of convection heat transfer during the flight are synchronously obtained. The main results of this work are as follows:

(1) The flight velocity is decreasing exponentially in the ascending period of the trajectory, and the

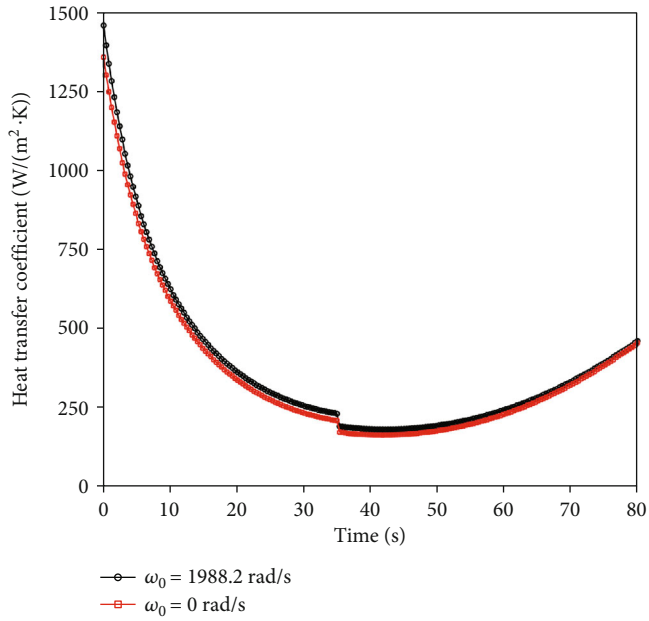

Figure 11: Average coefficients of convection heat transfer at different initial rotational speeds.

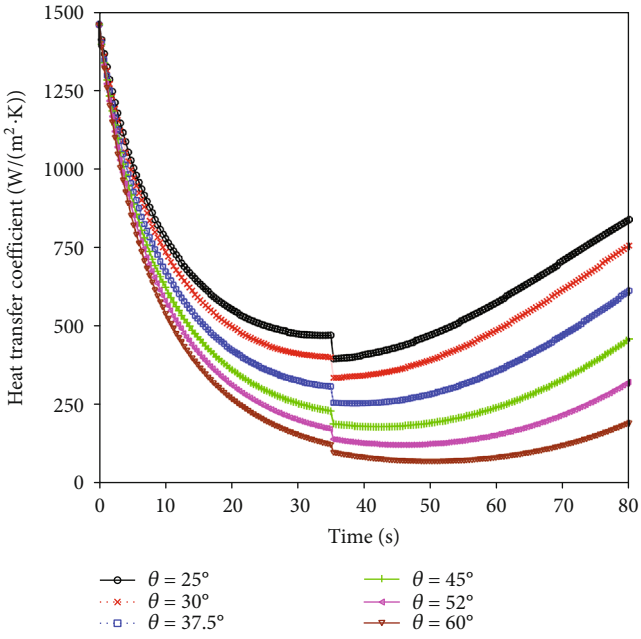

Figure 12: Average coefficients of convection heat transfer at different launch angles.

attenuation rates are quicker with the initial velocities. The exponential attenuation rate of angular speed in the ascending period is faster than in the descending. Besides, the average reference temperature on the surface of the conical part is significantly higher than that of the cylindrical part in the first 20 seconds of the trajectory, especially in a short time after launching. After 20 seconds, the average reference temperature on the conical surface is lower than that of the cylindrical part

(2) The average coefficient of convection heat transfer is increasing with the initial velocity and rotational speed, and the attenuation rates are growing rapidly at the ascending stage during the flight, whereas the coefficient is inversely proportional to the initial velocity at the descending stage, and the shot angle is changed similarly. Additionally, the transient coefficient of convection heat transfer is dropping sharply at the beginning, and rising dramatically before a slow attenuation

(3) Aerothermal characteristic is determined not only by the current flight state but also by the heat transfer environment during the flight, which is a progressive, lasting, and dynamic process. In consideration of the spinning speed, the coefficient of convection heat transfer is obviously too high to disregard, especially in supersonic regimes

Nomenclature

d: Diameter, m
m: Mass, kg
t: Time, s
Δs: Area of surface panel, m^2
ρ: Density, kg/m^3
cp: Specific heat capacity, J/(kg·K)
α: Cone-shaped angle, rad
λ: Thermal conductivity, W/(m·K)
κ: Adiabatic index
$\mathbf{n}$: Normal vector of surface panel
A: Equatorial moment of inertia
C: Polar moment of inertia
$\mathbf{v}$: Velocity, m/s
ω: Angular speed, rad/s

μ: Dynamic viscosity, $(N \cdot s)/m^2$
η: Rifling angle, rad
h: Heat transfer coefficient, $W/(m^2 \cdot K)$
δ_1: Elevation attack angle, rad
δ_2: Azimuth attack angle, rad
φ_1: Elevation angle in the x direction, rad
φ_2: Azimuth angle in the x direction, rad
ψ_1: Elevation angle in the velocity direction
ψ_2: Azimuth angle in the velocity direction, rad
T: Temperature, K
P: Pressure, Pa
H: Total enthalpy, J
Nu: Nusselt number
Re: Reynolds number
Pr: Prandtl number.

Subscripts

w: Wall
i: Compute node
x: Axial direction
r: Relative values
∞: Freestream condition
$*$: Flow parameter at reference temperature condition.

Data Availability

The [MATLAB calculation procedures] data used to support the findings of this study are available from the corresponding author upon request.

Conflicts of Interest

The authors declare that there is no conflict of interest regarding the publication of this paper.

Acknowledgments

This work was supported by the Natural Science Foundation of China (NSFC) under the Grant Number of 11372136, the Shanghai Municipal Science and Technology Commission of China (SMSTCC) under the Grant Number of 17050502000, and the Shanghai Ocean University under the Grant Number of A2-2006-20-200210.

References

[1] T. Ozawa, T. Suzuki, and K. Fujita, "Aerodynamic measurements and computational analyses in hypersonic rarefied flows," *AIAA Journal*, vol. 53, no. 11, pp. 3327–3337, 2015.

[2] C. J. Alban, A. N. Palazotto, and J. L. Rutledge, "Thermal considerations with respect to sliding contact at high speed," *Journal of Thermophysics and Heat Transfer*, vol. 30, no. 1, pp. 54–61, 2016.

[3] M. B. Gerdroodbary, M. Imani, and D. D. Ganji, "Investigation of film cooling on nose cone by a forward facing array of micro- jets in hypersonic flow," *International Communications in Heat and Mass Transfer*, vol. 64, pp. 42–49, 2015.

[4] S. Eyi, K. M. Hanquist, and I. D. Boyd, "Aerothermodynamic design optimization of hypersonic vehicles," *Journal of Thermophysics and Heat Transfer*, vol. 33, no. 2, pp. 392–406, 2019.

[5] X. Pan, X. Wang, R. Wang, and L. Wang, "Infrared radiation and stealth characteristics prediction for supersonic aircraft with uncertainty," *Infrared Physics & Technology*, vol. 73, pp. 238–250, 2015.

[6] S. P. Mahulikar, H. R. Sonawane, and G. Arvind Rao, "Infrared signature studies of aerospace vehicles," *Progress in Aerospace Sciences*, vol. 43, no. 7-8, pp. 218–245, 2007.

[7] G. Bingtao, W. Xiaorui, C. Yujiao, L. Zhaohui, and Z. Jianlei, "High-accuracy infrared simulation model based on establishing the linear relationship between the outputs of different infrared imaging systems," *Infrared Physics & Technology*, vol. 69, pp. 155–163, 2015.

[8] R. Savino, M. de Stefano Fumo, D. Paterna, and M. Serpico, "Studio aerotermodinamico di sistemi di protezione termica basati su UHTC," *Aerospace Science and Technology*, vol. 9, no. 2, pp. 151–160, 2005.

[9] Y. Takahashi and K. Yamada, "Aerodynamic-heating analysis of sample-return capsule in future Trojan-asteroid exploration," *Journal of Thermophysics and Heat Transfer*, vol. 32, no. 3, pp. 547–559, 2018.

[10] M. B. Gerdroodbary and S. M. Hosseinalipour, "Numerical simulation of hypersonic flow over highly blunted cones with spike," *Acta Astronautica*, vol. 67, no. 1-2, pp. 180–193, 2010.

[11] M. B. Gerdroodbary, M. Imani, and D. D. Ganji, "Heat reduction using conterflowing jet for a nose cone with aerodisk in hypersonic flow," *Aerospace Science and Technology*, vol. 39, pp. 652–665, 2014.

[12] S. Zhou, Z. O'Neill, and C. O'Neill, "A review of leakage detection methods for district heating networks," *Applied Thermal Engineering*, vol. 137, pp. 567–574, 2018.

[13] J. Huang, P. Li, and W. Yao, "Thermal protection system gap analysis using a loosely coupled fluid- structural thermal numerical method," *Acta Astronautica*, vol. 146, pp. 368–377, 2018.

[14] G. R. Inger, "Nonequilibrium boundary-layer effects on the aerodynamic heating of hypersonic waverider vehicles," *Journal of Thermophysics and Heat Transfer*, vol. 9, no. 4, pp. 595–604, 1995.

[15] X. I. A. Yang, J. Urzay, S. Bose, and P. Moin, "Aerodynamic heating in wall-modeled large-Eddy simulation of high-speed flows," *AIAA Journal*, vol. 56, no. 2, pp. 731–742, 2018.

[16] S. Zhang, F. Chen, and H. Liu, "Time-adaptive, loosely coupled strategy for conjugate heat transfer problems in hypersonic flows," *Journal of Thermophysics and Heat Transfer*, vol. 28, no. 4, pp. 635–646, 2014.

[17] D. Knight, O. Chazot, J. Austin et al., "Assessment of predictive capabilities for aerodynamic heating in hypersonic flow," *Progress in Aerospace Sciences*, vol. 90, pp. 39–53, 2017.

[18] D. Knight, J. Longo, D. Drikakis et al., "Assessment of CFD capability for prediction of hypersonic shock interactions," *Progress in Aerospace Sciences*, vol. 48-49, pp. 8–26, 2012.

[19] D. Knight, H. Yan, A. G. Panaras, and A. Zheltovodov, "Advances in CFD prediction of shock wave turbulent boundary layer interactions," *Progress in Aerospace Sciences*, vol. 39, no. 2-3, pp. 121–184, 2003.

[20] Y. Zheng and Z. Qiu, "Uncertainty propagation in aerodynamic forces and heating analysis for hypersonic vehicles with

uncertain-but-bounded geometric parameters," *Aerospace Science and Technology*, vol. 77, pp. 11–24, 2018.

[21] M. Y. M. Ahmed and N. Qin, "Metamodels for aerothermodynamic design optimization of hypersonic spiked blunt bodies," *Aerospace Science and Technology*, vol. 14, no. 5, pp. 364–376, 2010.

[22] M. Y. M. Ahmed and N. Qin, "Recent advances in the aerothermodynamics of spiked hypersonic vehicles," *Progress in Aerospace Sciences*, vol. 47, no. 6, pp. 425–449, 2011.

[23] M. Y. M. Ahmed and N. Qin, "Numerical investigation of aeroheating characteristics of spiked blunt bodies at Mach six flight conditions," *Aeronautical Journal*, vol. 115, no. 1168, pp. 377–386, 2011.

[24] M. Y. M. Ahmed and N. Qin, "Surrogate-based multi-objective aerothermodynamic design optimization of hypersonic spiked bodies," *AIAA Journal*, vol. 50, no. 4, pp. 797–810, 2012.

[25] M. Y. M. Ahmed and N. Qin, "Investigation of flow asymmetry around axi-symmetric spiked blunt bodies in hypersonic speeds," *Aeronautical Journal*, vol. 118, no. 1200, pp. 169–179, 2014.

[26] Q. Qin, J. Xu, and S. Guo, "Fluid-thermal analysis of aerodynamic heating over spiked blunt body configurations," *Acta Astronautica*, vol. 132, pp. 230–242, 2017.

[27] M. B. Gerdroodbary, "Numerical analysis on cooling performance of counterflowing jet over aerodisked blunt body," *Shock Waves*, vol. 24, no. 5, pp. 537–543, 2014.

[28] M. B. Gerdroodbary, S. Bishehsari, S. M. Hosseinalipour, and K. Sedighi, "Transient analysis of counterflowing jet over highly blunt cone in hypersonic flow," *Acta Astronautica*, vol. 73, pp. 38–48, 2012.

[29] L. Wang, Y. Li, Z. Zhao, and Z. Liu, "Transient thermal and pressurization performance of LO2 tank during helium pressurization combined with outside aerodynamic heating," *International Journal of Heat and Mass Transfer*, vol. 62, pp. 263–271, 2013.

[30] M. G. Persova, Y. G. Soloveichik, V. K. Belov et al., "Modeling of aerodynamic heat flux and thermoelastic behavior of nose caps of hypersonic vehicles," *Acta Astronautica*, vol. 136, pp. 312–331, 2017.

[31] T. G. Vincent, E. N. Rolfe, K. T. Lowe, and J. A. Schetz, "Aerodynamic analysis of total temperature probe thermal performance using conjugate heat transfer," *Journal of Thermophysics and Heat Transfer*, vol. 33, no. 3, pp. 830–843, 2019.

[32] P. Duda, "A method for transient thermal load estimation and its application to identification of aerodynamic heating on atmospheric reentry capsule," *Aerospace Science and Technology*, vol. 51, pp. 26–33, 2016.

[33] N. Li, Z. Lv, S. Wang, G. Gong, and L. Ren, "A real-time infrared radiation imaging simulation method of aircraft skin with aerodynamic heating effect," *Infrared Physics & Technology*, vol. 71, pp. 533–541, 2015.

[34] S. I. Silton, "Navier-Stokes computation's for a spinning projectile from subsonic to supersonic speeds," *Journal of Spacecraft and Rockets*, vol. 42, no. 2, pp. 223–231, 2005.

[35] D. S. James, *CFD prediction of Magnus effect in subsonic to supersonic flight*, U.S. Army Research Laboratory, ARL–TR–4929, 2009.

Hindawi
International Journal of Aerospace Engineering
Volume 2020, Article ID 8885226, 14 pages
https://doi.org/10.1155/2020/8885226

Research Article

Phase-Field-Based LBM Analysis of KHI and RTI in Wide Ranges of Density Ratio, Viscosity Ratio, and Reynolds Number

Xun Zhou, Bo Dong, and Weizhong Li

Key Laboratory of Ocean Energy Utilization and Energy Conservation of Ministry of Education, Dalian University of Technology, Dalian 116024, China

Correspondence should be addressed to Weizhong Li; wzhongli@dlut.edu.cn

Received 8 April 2020; Revised 25 May 2020; Accepted 25 May 2020; Published 19 June 2020

Academic Editor: Feng Qu

Numerous studies have elaborated the dominated roles of Kelvin-Helmholtz instability (KHI) and Rayleigh-Taylor instability (RTI) in the liquid sheet breakup and primary atomization. As for applications in aeronautics, the liquid-gas mixing generally occurs at the challenging conditions of a large density ratio and high Reynolds number. Hence, the evaluation of KHI and RTI under such challenging conditions will have great significance in better understanding the destabilizing mechanism of the liquid layer. To this end, a lattice Boltzmann multiple-relaxation-time (MRT) two-phase model, based on the conservative Allen-Cahn equation, is reconstructed for the present study. Preliminarily, the numerical stability and accuracy of this MRT model are tested by Laplace's law under a large density ratio and high Reynolds number, including the sensitivity study to the values of mobility. Afterward, KHI and RTI are investigated in wide ranges of the Reynolds number, density ratio, and viscosity ratio. Numerical results indicate that the enhanced viscous force of light fluid with an increasing viscosity ratio notably suppresses the roll-ups of heavy fluid in KHI and RTI. As for the density ratio, it generally shows negative impacts on fluid-mixing in KHI and spike-spiraling in RTI. However, when the density ratio and the Reynolds number both arrive at high levels, the Kelvin-Helmholtz wavelets aroused by a dominated inertia force of heavy fluid trigger severe interface disintegration. The above results once more demonstrate the excellent ability of the present model in dealing with challenging conditions. Besides, the morphological characteristics of KHI and RTI at a high Reynolds number and large density ratio also greatly support the typical interface breakup mechanism observed in primary atomization.

1. Introduction

Among many fundamental and ubiquitous fluid phenomena in nature and engineering, the Kelvin-Helmholtz instability (KHI) and the Rayleigh-Taylor instability (RTI) have attracted much attention for their essential roles playing in the interface distortion and breakup [1]. To be specific, KHI occurs at a perturbed interface between two fluid flows with different tangential velocities, while RTI is aroused when a heavy fluid is accelerated by gravity against a light one [2, 3]. Recent studies have elaborated that these two instabilities dominate the liquid sheet breakup and primary atomization: KHI leading to the amplification of interface perturbations and formation of longitudinal waves, followed by RTI resulting in the formation of bulges on top of the wave crest and subsequent destabilization of the liquid sheet [4–6]. Generally, for applications in aeronautics, the liquid-gas mixing layer encountered in atomization owns a large density contrast, and the Reynolds number of gas happens to be much higher than that of liquid. In that perspective, it is necessary to conduct investigations of KHI and RTI by considering the effects of large density contrast and high Reynolds number simultaneously, which has great significance in better understanding the destabilizing mechanism of the liquid layer.

In the past decades, extensive efforts have been devoted to probe KHI and RTI through theoretical analyses [7, 8], experiments [9, 10], and numerical simulations [11–15].

However, few studies deal with them under the conditions of large density contrast and high Reynolds number. In terms of KHI, Ceniceros and Roma [12] studied the long-time dynamics of KHI by a fully adaptive nonstiff method. They inspected the interface evolution at a high Reynolds number only for the cases of density- and viscosity-matched fluids. Rangel and Sirignano [14] investigated the effects of the density ratio and surface tension on the nonlinear growth of interface disturbance using a vortex-sheet discretization approach. They found out that the disturbance growth was suppressed by increasing the surface tension or the density ratio, and a bifurcation phenomenon was observed when density ratios were larger than 0.2. In a recent experimental study, Wan et al. [9] observed the single-mode KHI in a supersonic flow with the Atwood number being 0.81, and hydrodynamic simulations reported in their work can reproduce the resulting interface structure fairly well. Besides, a hydrodynamic model based on the evolution of KHI in shear viscous flows has been proposed in the work of Konovalov et al. [16] to specify the formation of nanostructures in materials subjected to the action of concentrated energy flows. As for RTI, the pioneer study was performed by Taylor [3] via theoretical analyses to explore the factors affecting the instability growth rate, followed by the experiment of Lewis [10] to test the theoretical conclusions. Then, in the work of Goncharov [17], the continuous bubble evolution of single-mode RTI at arbitrary Atwood numbers was provided by an analytical model from the earlier exponential growth to the nonlinear regime. Later, Wei and Livescu [13] investigated the growth of 2D single-mode RTI at low Atwood numbers by using direct numerical simulation. The mean quadratic growth was found at late times and sufficiently high Reynolds numbers.

In the current work, we invoke the lattice Boltzmann method (LBM) to investigate KHI and RTI, given its distinct advantages in tracking interface evolution with large morphological deformations [18, 19]. To begin with KHI, Zhang et al. [20] used the two-phase LB model proposed by He et al. [21] to study this type of instability for density-matched incompressible fluids, focusing on the effects of surface tension at a low Reynolds number (Re = 250). In order to assess KHI at a high Reynolds number, Fakhari and Lee [22] incorporated the multiple-relaxation-time (MRT) collision operator into a LB multiphase model. Their simulation, however, was limited to low density ratios with a Reynolds number up to 10000. Through an efficient discrete Boltzmann model, Gan et al. [23] investigated nonequilibrium and morphological characterizations of KHI in compressible flows, taking the effects of viscosity and heat conduction into account. Regarding the applications of LBM in RTI, most of the related studies account for incompressible fluids. For example, He et al. [21] proposed a LB multiphase model in the nearly incompressible limit, and it was applied to simulate RTI with a low density contrast at a moderate Reynolds number. Later, Liang et al. [24] studied RTI via a new phase-field-based MRT LB model in incompressible multiphase flow systems. The Reynolds number was increased to 30000 in their study.

Based on the research listed above, the LBM has achieved great success in the fields of KHI and RTI. However, at present, it is still an open subject for the LBM with many challenges, especially those relevant to a large density contrast at a high Reynolds number. The existing multiphase LB models dealing with a large density contrast can be roughly classified into pseudo-potential-based type and phase-field-based type. For the pseudo-potential-based type, the models of Li et al. [25] and Xu et al. [26] are conducted at a density ratio in excess of 700. For the phase-field-based type, most of the models use the Cahn-Hilliard (CH) equation for interface tracking, such as those of Zu and He [19] and Yan and Zu [18]. Recently, Liang et al. [27] and Fakhari and Bolster [28] also apply the Allen-Cahn (AC) equation for interface tracking. Compared with the CH equation, the AC equation contains a lower-order diffusion term. Thus, according to the work of Chai et al. [29] and Wang et al. [30], the AC-based model theoretically has a higher numerical accuracy and stability in solving the index function and density field than the CH-based one. To this end, a lattice Boltzmann two-phase MRT model based on the conservative AC equation is reconstructed in this paper to enhance its numerical stability at a large density contrast and high Reynolds number. Then, it is adopted to investigate KHI and RTI by considering the effects of the viscosity ratio, density ratio, and Reynolds number. Special attention is paid on morphological characteristics under the challenging conditions of a high Reynolds number and large density ratio, which are rarely covered in the literature. The rest of this paper is therefore organized as follows: In Section 2, the present MRT model is introduced in detail. In Section 3, after the preliminarily evaluation, the present model is utilized to inspect KHI and RTI in wide ranges of the viscosity ratio, density ratio, and Reynolds number. In Section 4, some conclusions are summarized. It is worth noting that the postprocessing tool of Tecplot 360 is utilized to visualize all the numerical results in this paper.

2. Mathematical Method

2.1. The MRT LB Model for the Conservative Allen-Cahn Equation. With the MRT collision operator [29], the generalized evolution equation for the conservative AC equation [29, 31] can be written as

$$f_i(x + c_i\delta t, t + \delta t) = f_i(\boldsymbol{x}, t) - \Lambda_{ij}^{f}\left[f_j - f_j^{eq}\right]\Big|_{(\boldsymbol{x},t)} + \delta t\left[F_i - 0.5\Lambda_{ij}^{f}F_j\right]\Big|_{(\boldsymbol{x},t)}, \quad (1)$$

where $f_i(x, t)$ and $f_i^{\mathrm{eq}}(x, t)$ are the particle distribution function and its corresponding equilibrium distribution function for the order parameter ϕ at position x and time t, respectively. Here, the order parameter ϕ taking 1 and 0 is adopted to distinguish different fluids with the interface marked by the contour level of $\phi = 0.5$. c_i is the discrete velocity of the ith direction, δt is the time step. Λ_{ij}^{f} stands for an element of the collision matrix $\boldsymbol{\Lambda}^{f} = \mathbf{M}^{-1}\mathbf{S}^{f}\mathbf{M}$, in

which $\mathbf{M}$ is an orthogonal transformation matrix and $\mathbf{S}^f$ is a diagonal matrix given by (for the D2Q9 model)

$$\mathbf{M} = \begin{pmatrix} 1 & 1 & 1 & 1 & 1 & 1 & 1 & 1 & 1 \\ -4 & -1 & -1 & -1 & -1 & 2 & 2 & 2 & 2 \\ 4 & -2 & -2 & -2 & -2 & 1 & 1 & 1 & 1 \\ 0 & 1 & 0 & -1 & 0 & 1 & -1 & -1 & 1 \\ 0 & -2 & 0 & 2 & 0 & 1 & -1 & -1 & 1 \\ 0 & 0 & 1 & 0 & -1 & 1 & 1 & -1 & -1 \\ 0 & 0 & -2 & 0 & 2 & 1 & 1 & -1 & -1 \\ 0 & 1 & -1 & 1 & -1 & 0 & 0 & 0 & 0 \\ 0 & 0 & 0 & 0 & 0 & 1 & -1 & 1 & -1 \end{pmatrix}, \quad (2)$$

$$\mathbf{S}^f = \operatorname{diag}\left(s_0^f, s_1^f, s_2^f, s_3^f, s_4^f, s_5^f, s_6^f, s_7^f, s_8^f\right).$$

In Equation (1), F_i represents the forcing term in the velocity space [27, 32], and it is defined as

$$F_i = \frac{\omega_i c_i \cdot \left[\partial_t(\phi u) + c_s^2 \lambda n\right]}{c_s^2}, \quad (3)$$

where ω_i is the weight coefficient with the value given by $\omega_0 = 4/9$, $\omega_{1,\cdots 4} = 1/9$, and $\omega_{5,\cdots 8} = 1/36$, $c_s = c/\sqrt{3}$ is the sound speed, and u is the macroscopic velocity. $n = \nabla\phi/|\nabla\phi|$ denotes the unit vector normal to the interface. $\lambda = 4\phi(1-\phi)/W$ is a function of ϕ, and W is the interface thickness. The time derivative term $\partial_t(\phi u)$ is introduced to eliminate the artificial term in the recovered equation.

Through the orthogonal transformation matrix $\mathbf{M}$, the right-hand side of Equation (1) can be projected onto the moment space via $\mathbf{m}_f = \mathbf{M}\mathbf{f}$ and $\mathbf{m}_f^{\mathrm{eq}} = \mathbf{M}\mathbf{f}^{\mathrm{eq}}$ [33, 34] as

$$\mathbf{m}_f^* = \mathbf{m}_f - \mathbf{S}^f\left(\mathbf{m}_f - \mathbf{m}_f^{\mathrm{eq}}\right) + \delta t\left(\mathbf{I} - \frac{\mathbf{S}^f}{2}\right)\mathbf{E}, \quad (4)$$

where $\mathbf{f} = (f_0, \cdots f_8)^T$, $\mathbf{f}^{\mathrm{eq}} = (f_0^{\mathrm{eq}}, \cdots f_8^{\mathrm{eq}})^T$, $\mathbf{I}$ is the unit tensor, and $\mathbf{E} = \mathbf{M}\mathbf{F} = \mathbf{M}(F_0, \cdots, F_8)^T$ is the forcing term in the moment space. Based on $\mathbf{f}^{\mathrm{eq}}$ and $\mathbf{F}$ in the velocity space [27, 32], $\mathbf{m}_f^{\mathrm{eq}}$ and $\mathbf{E}$ can be easily derived for the D2Q9 model as

$$\mathbf{m}_f^{eq} = \phi\left(1, -2, 1, u_x, -u_x, u_y, -u_y, 0, 0\right)^T, \quad (5)$$

$$\mathbf{E} = \begin{pmatrix} 0 \\ 0 \\ 0 \\ \partial_t(\phi u_x) + c_s^2 \lambda n_x \\ -\partial_t(\phi u_x) - c_s^2 \lambda n_x \\ \partial_t(\phi u_y) + c_s^2 \lambda n_y \\ -\partial_t(\phi u_y) - c_s^2 \lambda n_y \\ 0 \\ 0 \end{pmatrix}, \quad (6)$$

where u_x and u_y are the components of the macroscopic velocity u, n_x and n_y are the components of the unit vector $\mathbf{n}$. Afterward, the streaming process is given as

$$f_i(\boldsymbol{x} + \boldsymbol{c}_i\delta t, t + \delta t) = f_i^*(\boldsymbol{x}, t), \quad (7)$$

where the postcollision distribution function f_i^* can be obtained via $\mathbf{f}^* = \mathbf{M}^{-1}\mathbf{m}_f^*$.

Applying the Chapman-Enskog expansion to Equation (1), the conservative AC equation [30, 35] can be recovered correctly as

$$\frac{\partial\phi}{\partial t} + \nabla \cdot (\phi \boldsymbol{u}) = \nabla \cdot [M(\nabla\phi - \lambda \boldsymbol{n})], \quad (8)$$

where the mobility M is determined by

$$M = c_s^2\left(\tau_f - 0.5\right)\delta t, \quad (9)$$

in which τ_f is the dimensionless relaxation time of f_j, and it is related to the diagonal matrix $\mathbf{S}^f$ with $s_3^f = s_5^f = 1/\tau_f$. In the present model, the order parameter is calculated as

$$\phi = \sum_i f_i, \quad (10)$$

and the fluid density ρ should be consistent with the order parameter by taking the linear interpolation as

$$\rho = \phi(\rho_A - \rho_B) + \rho_B, \quad (11)$$

where ρ_A and ρ_B stand for the densities of two different fluids corresponding to the order parameter $\phi_A = 1$ and $\phi_B = 0$, respectively.

2.2. The MRT LB Model for the Navier-Stokes Equations. In order to improve the numerical stability, the lattice

Boltzmann equation for the incompressible NS equations is combined with the MRT collision operator as

$$g_i(\boldsymbol{x}+\boldsymbol{c_i}\delta t, t+\delta t) = g_i(\boldsymbol{x},t) - \Lambda_{ij}^{g}\left[g_j - g_j^{eq}\right]\Big|_{(\boldsymbol{x},t)} + \delta t\left(R_i - 0.5\Lambda_{ij}^{g}R_j\right)\Big|_{(\boldsymbol{x},t)}, \tag{12}$$

where g_i and g_i^{eq} are the density distribution function and its corresponding equilibrium distribution function, respectively. R_i is the forcing term in the velocity space. Λ_{ij}^{g} is an element of the collision matrix $\boldsymbol{\Lambda}^{g} = \mathbf{M}^{-1}\mathbf{S}^{g}\mathbf{M}$, in which $\mathbf{S}^{g}$ is a diagonal matrix given by (for the D2Q9 model)

$$\mathbf{S}^{g} = \mathrm{diag}\left(s_0^{g}, s_1^{g}, s_2^{g}, s_3^{g}, s_4^{g}, s_5^{g}, s_6^{g}, s_7^{g}, s_8^{g}\right). \tag{13}$$

Similar to Equation (3), the right-hand side of Equation (12) in the moment space reads

$$\mathbf{m}_g^{*} = \mathbf{m}_g - \mathbf{S}^{g}\left(\mathbf{m}_g - \mathbf{m}_g^{\mathrm{eq}}\right) + \delta t\left(\mathbf{I} - \frac{\mathbf{S}^{g}}{2}\right)\widehat{\mathbf{R}} \tag{14}$$

where $\mathbf{m}_g = \mathbf{M}\mathbf{g}$, $\mathbf{m}_g^{\mathrm{eq}} = \mathbf{M}\mathbf{g}^{\mathrm{eq}}$, and $\widehat{\mathbf{R}} = \mathbf{M}\mathbf{R}$ are the corresponding matrices in the moment space with $\mathbf{g} = (g_0,\cdots g_8)^{T}$, $\mathbf{g}^{\mathrm{eq}} = (g_0^{\mathrm{eq}},\cdots g_8^{\mathrm{eq}})^{T}$, and $\mathbf{R} = (R_0,\cdots,R_8)^{T}$. Inspired by the BGK model of Liang et al. [27], the matrices $\mathbf{m}_g^{eq}$ and $\widehat{\mathbf{R}}$ for the D2Q9 model are evaluated as

$$\mathbf{m}_g^{eq} = \begin{pmatrix} 0 \\ 6p + 3\rho|\boldsymbol{u}|^2 \\ -9p - 3\rho|\boldsymbol{u}|^2 \\ \rho u_x \\ -\rho u_x \\ \rho u_y \\ -\rho u_y \\ \rho\left(u_x^2 - u_y^2\right) \\ \rho u_x u_y \end{pmatrix}, \quad \widehat{\mathbf{R}} = \begin{pmatrix} u_x\partial_x\rho + u_y\partial_y\rho \\ 0 \\ -u_x\partial_x\rho - u_y\partial_y\rho \\ G_x \\ -G_x \\ G_y \\ -G_y \\ 2\left(u_x\partial_x\rho - u_y\partial_y\rho\right)/3 \\ \left(u_x\partial_y\rho + u_y\partial_x\rho\right)/3 \end{pmatrix}, \tag{15}$$

where p is the hydrodynamic pressure. G_x and G_y are the components of the total force $\boldsymbol{G} = \boldsymbol{F}_s + \boldsymbol{F}_e + \boldsymbol{F}_a$. Here, $\boldsymbol{F}_s = -\sigma\alpha W|\nabla\phi|\nabla\phi\nabla\cdot\mathbf{n}$ is the surface tension force with the formulation recommended by Kim [36] and Ren et al. [37], where σ is the surface tension coefficient. F_e is the possible body force. At the interface, phase-field-based LB models fail to satisfy the continuity equation [38] and, hence, an additional interfacial force $F_a = q_a u$ is introduced with the term q_a determined by

$$q_a = M(\rho_A - \rho_B)\left[\nabla^2\phi - \nabla\cdot(\lambda\boldsymbol{n})\right]. \tag{16}$$

Ultimately, with $\mathbf{g}^{*} = \mathbf{M}^{-1}\mathbf{m}_g^{*}$, the streaming process is achieved as

$$g_i(x + c_i\delta t, t + \delta t) = g_i^{*}(x,t). \tag{17}$$

Based on the density distribution function g_i, the macroscopic quantities u and p can be evaluated as

$$u = \frac{1}{\rho - 0.5q_a}\left[\sum_i c_i g_i + \frac{\delta t}{2}\left(F_s + F_e\right)\right], \qquad p = \frac{c_s^2}{1-\omega_0}\left[\sum_{i\neq 0} g_i + \frac{\delta t}{2}u\cdot\nabla\rho - \omega_0\rho\frac{|u|^2}{2c_s^2}\right]. \tag{18}$$

Besides, through the Chapman-Enskog analysis, the kinematic viscosity ν is determined by

$$\nu = c_s^2\left(\tau_g - 0.5\right)\delta t, \tag{19}$$

where $\tau_g = 1/s_7^{g} = 1/s_8^{g}$. Note that the value of viscosity is usually not uniform in a two-phase flow system. To make it smoothly across the interface, the popular treatments are supposed that the viscosity is a linear or inverse linear function of the order parameter [18, 21, 39]. In this work, the linear form is adopted,

$$\nu = \phi(\nu_A - \nu_B) + \nu_A, \tag{20}$$

where ν_A and ν_B are the kinematic viscosities of two different fluids corresponding to the order parameter $\phi_A = 1$ and $\phi_B = 0$, respectively. Hence, the elements s_7^{g} and s_8^{g} of the diagonal matrix $\mathbf{S}^{g}$ are not uniform in the whole system due to its relation with the kinematic viscosity. Regarding the derivative terms in the present model, the explicit Euler scheme is adopted to calculate the temporal derivative in Equation (6) [40], while the gradient and the Laplacian operator are determined by second-order isotropic central schemes used in the studies of Yan and Zu and Zu and He [18, 19].

3. Results and Discussion

3.1. Static Droplet. Before the simulation of KHI and RTI, the present model is preliminarily tested by Laplace's law as well as the sensitivity study to the values of mobility. Initially, a

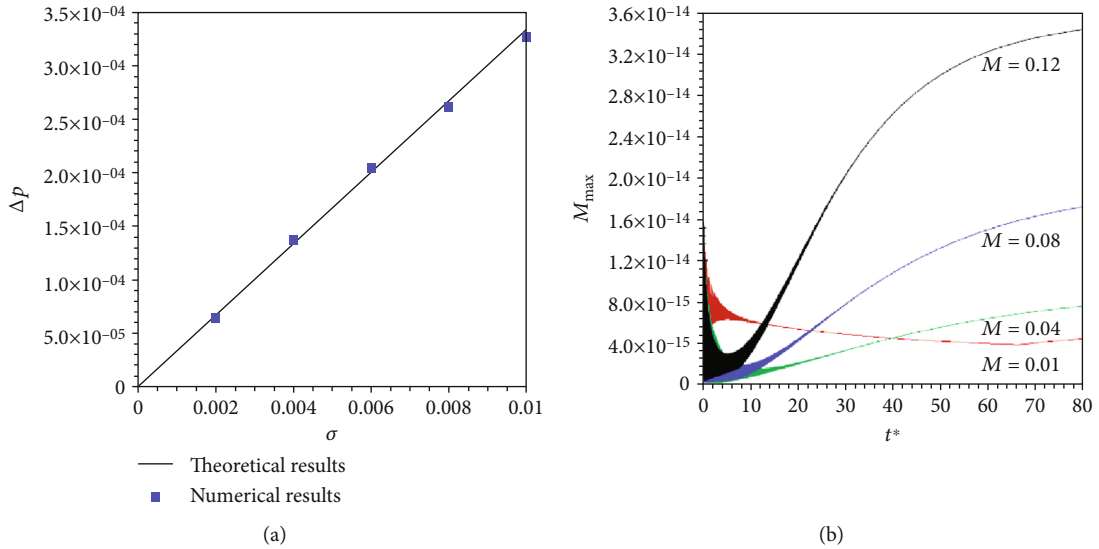

FIGURE 1: Validation and sensitivity study. (a) Comparison of the pressure difference between theoretical and numerical results. (b) Maximum kinetic energy for various mobility.

static droplet with the radius $R = 25$ surrounded by the gas phase is placed at the center of a periodic domain with 150×150 grid points. To mimic the challenging condition of the large density ratio and high Reynolds number, the density ratio and kinematic viscosity of liquid and gas are set as $\rho_A/\rho_B = 1000$ and $\nu_A = \nu_B = 0.002$, respectively. According to Laplace's law, the theoretical pressure difference between liquid and gas is $\Delta p = \sigma/R$ at steady-state. Figure 1(a) compares the theoretical and numerical values of pressure difference for various surface tension coefficients, which are in good agreement. In the simulation, we fix $s_0^f = s_7^f = s_8^f = 1.0$, $s_1^f = s_2^f$, and $s_4^f = s_6^f$ as usual. It is found out that $0.75 \le s_1^f (= s_2^f) \le 1.2$ and $0.6 \le s_4^f (= s_6^f) \le 1.3$ all can give satisfying results. For simplicity, $s_1^f (= s_2^f = s_4^f = s_6^f) = 1.1$ is set. Regarding the relaxation elements in $\mathbf{S}^g$, similar values are adopted as those in Ref. [22], except $s_0^g = s_3^g = s_5^g = 1.0$ and $s_7^g = s_8^g$ related to kinematic viscosity.

For the importance of mobility in the present model, a sensitivity study to its values is necessary. Figure 1(b) depicts the maximum kinetic energy $E_{\max}$ in the system for various mobilities. Here, the kinetic energy and the dimensionless time are defined as $E = \rho|u|^2/2$ and $t^* = t\sigma/(\rho_B \nu_B R)$, respectively. It is noteworthy that the present MRT model can successfully damp high-frequency oscillations of the kinetic energy at the early stages. Besides, the undervalue of mobility allows less damping time and lower kinetic energy, which also means smaller spurious currents (10^{-9}) in the system. Taking the numerical stability into account as well, the mobility is selected as a reasonable value of $M = 0.01$ in the following study.

3.2. Kelvin-Helmholtz Instability. In this section, KHI in a two-phase incompressible flow system is considered with the schematic diagram depicted in Figure 2. The shear flow of two immiscible fluids with densities ρ_A and ρ_B takes place in a 2D channel of size $(\lambda \times 2\lambda)$, whose top and bottom walls move in opposite directions. Four dimensionless groups are chosen to regulate the present issue: density ratio, viscosity ratio, Weber number $\mathrm{We} = 4U_0^2\lambda/\nu_A$, and Reynolds number $\mathrm{Re} = 2U_0\lambda/\nu_A$, where U_0 is the streaming velocity of the top and bottom walls. To minimize the compressibility effects, the Mach number is set to satisfy $\mathrm{Ma} = U_0/c_s \le 0.05$. Besides, the dimensionless time is measured as $t^* = 2U_0 t/\lambda$.

As specified in Ref. [12], we prescribed a vortex sheet in the computational domain that the interface is initially perturbed by a uniformly concentrated vorticity distribution $\omega_0(x, y)$ in the form of the Dirac δ function as

$$\omega_0(x, y) = \delta_h[h(x, y)], \tag{21}$$

with

$$h(x, y) = \frac{y}{\lambda} + 0.01 \sin\left(\frac{2\pi(x + y)}{\lambda}\right), \tag{22}$$

where $h(x, y)$ is the interface location in the dimensionless form at $t^* = 0$, and the Dirac δ function is approximated with the following smoothed 4-point cosine function [41],

$$\delta_h(h) = \begin{cases} [\pi + 2\sin(\pi(2h+1)/4) - 2\sin(\pi(2h-1)/4)]/4\pi, & |h| < 1.5, \\ [5\pi - 2\pi\,|\,h| - 4\sin(\pi(2\,|\,h| - 1)/4)]/8\pi, & 1.5 \le |h| \le 2.5, \\ 0, & |h| > 2.5. \end{cases} \tag{23}$$

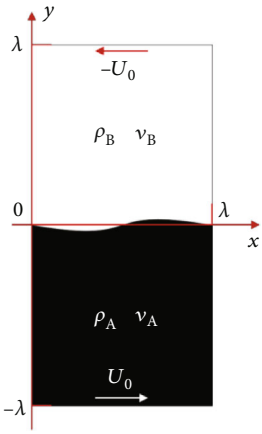

Figure 2: Schematic diagram for Kelvin-Helmholtz instability.

Based on the vorticity distribution in the whole domain, we can find the streaming function $\Delta\psi$ by solving the Poisson equation $\Delta\psi = -\omega_0$, and subsequently, obtain the initial velocity field via $u_0 = \nabla \times \psi$. In the simulation, the periodic boundary conditions are applied in the streamwise direction, while the top and bottom walls with a streaming velocity are implemented by the general bounce-back scheme [42]. The distribution profile of the order parameter is initialized by

$$\phi(x, y) = 0.5 - 0.5 \tanh\left(\frac{2(y - (\lambda - 0.01\lambda \sin(2\pi x/\lambda)))}{W}\right), \quad (24)$$

which enables the value of the order parameter to be smooth across the interface. First, the density- and viscosity-matched fluids are considered for grid resolution study by comparing the results with those of the AMR scheme [12]. As shown in Figure 3, a symmetric interface roll-up is gradually formed with Re = 10000 and We = 400, and both vorticity contours and interface locations agree well with the AMR results based on the grids of 512×1024.

The further study focuses on the shear-layer instability of fluids with a fixed density contrast but different viscosity ratios ($r_\nu = \nu_B/\nu_A$ =1, 2, 4, and 8). The Reynolds number is fixed at Re = 10000 with Weber number being We = 400. Figure 4 shows the corresponding results of temporal interface evolutions. As it can be seen, the interface roll-ups are no longer symmetric compared to those of the density-matched fluids, and such interface asymmetry caused by density contrast was also reported in the work of Tauber et al. [43]. Besides, by increasing the viscosity ratio from 1 to 8, the roll-ups of the growing mixing layer are suppressed. This phenomenon can be reflected by the time-varying kinetic energy in the system. Here, the kinetic energy along x- and y-directions are defined as $E_x = \rho u_x^2/2$ and $E_y = \rho u_y^2/2$, respectively, and their peak values ($E_{x|\max}$ and $E_{y|\max}$) versus the dimensionless time t^* are portrayed in Figure 5. It is observed that both $E_{x|\max}$ and $E_{y|\max}$, which represent the interacting strength of two different fluids [44], reduce with the increasing of the viscosity ratio, thus leading to the weakened interface roll-ups.

We continue with our investigations by taking the effects of the density ratio and Reynolds number into account. In this part, three density ratios ($r_\rho = \rho_A/\rho_B$ =10, 100, and 1000) are examined at different Reynolds numbers varying from 2000 to 10000, which intends to mimic the operating condition in prefilming primary atomization. As shown in Figure 6, a thick tip of the heavy fluid is stretched into a narrow ligament at the interface under low or moderate density ratios ($r_\rho \le 100$). When the Reynolds number is high enough (Re =10000), the ligament tends to detach from the heavy fluid. However, such a breakup pattern is not observed in the density-matched fluid system. This is due to that the inertial force of the heavy fluid comes to dominate the viscous force with the increasing density ratio and Reynolds number, causing a distorted interface and its subsequent disintegration. On the other hand, once the density ratio and Reynolds number both reach a high level, small Kelvin-Helmholtz wavelets are formed on large-scale waves of the perturbed interface, which trigger the chaotic interface evolution as shown in Figure 6(b) [45]. These severe topological changes at the interface are quite in line with those observed in the primary breakup of liquid sheets [1, 46].

From a different perspective, the effects of the density ratio and Reynolds number on the interface disturbance are quantitatively assessed by the averaged order parameter (ϕ_{avg}) with its definition given by $\phi_{\text{avg}} = \int_0^\lambda \phi(x, y)dx/\lambda$. Taking the case of Re = 2000 and $r_\rho = 10$ as an example, Figure 7 depicts the profiles of ϕ_{avg} against the y-direction at different times, in which the y-coordinate is measured by $y^* = (y + \lambda)/(2\lambda)$. As seen, the profile keeps to be smooth at the initial time, and then, it oscillates due to the mixing of two different fluids. Therefore, the symbol d_{mix} marked in Figure 7 can be roughly regarded as the width of the mixing layer. We then record the values of d_{mix} under different density ratios and Reynolds numbers in Table 1. Evidently, the width of the mixing layer increases with the Reynolds number, yet a reversed trend is observed by increasing the density ratio. These results are consistent with those displayed in Figure 6. Furthermore, a linear analysis has been carried out for KHI in wide ranges of the density ratio and Reynolds number. It is found out that the interface perturbation has an exponential growth at the initial linear increasing stage of KHI, which greatly depends on the density ratio and the Reynolds number. To be specific, the perturbation growth is accelerated by increasing the Reynolds number but it is suppressed by increasing the density ratio, which is in line with the numerical results. However, especially in the case of the large density ratio and high Reynolds number, the perturbation grows nonlinearly to form small Kelvin-Helmholtz wavelets at the later stage of KHI. The linear theory fails in this nonlinear regime, and the numerical results in this paper become useful alternatives.

3.3. Rayleigh-Taylor Instability. Figure 8 sketches the other incompressible two-phase flow system involved in this paper, where a layer of heavy fluid with density ρ_A is located on top

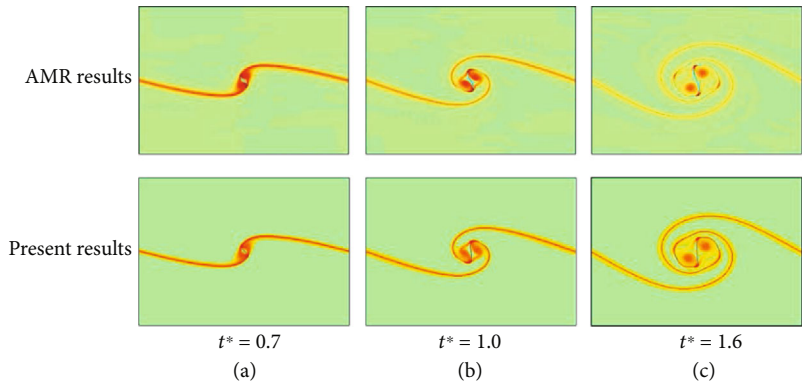

FIGURE 3: Vorticity contours (color) and interface locations (red line) of AMR scheme [12] and present model with Re = 10000, We = 400, $\rho_A = \rho_B$, and $\nu_A = \nu_B$.

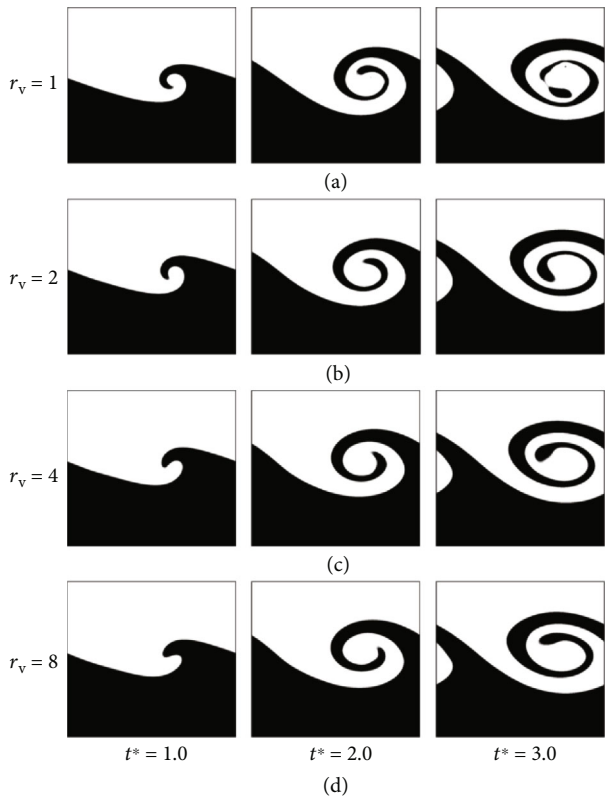

FIGURE 4: Snapshots of interface evolutions for different viscosity ratios (Re = 10000, We = 400, and $\rho_A/\rho_B = 2$).

of the light one with density ρ_B. As stated in Ref. [21], any disturbance at the interface will be accelerated by gravity to produce downward-moving spikes of heavy fluid and upward-moving bubbles of light fluid. This is the so-called RTI, a crucial type of instability that is responsible for the interface destabilization. In this section, we pay special attention to RTI regarding fluids with different viscosity ratios and density ratios in a wide range of the Reynolds number. The simulation is implemented in a 2D domain of size $d \times 4d$ with periodic and no-slip boundary conditions in the streamwise and normal-wall directions, respectively. The numerical results are presented in terms of dimensionless parameters, including the viscosity ratio, Atwood number $\mathrm{At} = (\rho_A - \rho_B)/(\rho_A + \rho_B)$, and Reynolds number $\mathrm{Re} = \sqrt{dg}d/\nu_A$. Here, g is the gravity acceleration. The time is normalized as $t^* = t/\sqrt{d/g}$.

Numerical study is started with two benchmark cases for grid resolution study and further verification. In the first case of viscosity-matched fluids, the initial order parameter profile, that smoothly across the interface with an amplitude of $0.1d$, is given as

$$\phi(x, y) = 0.5 + 0.5 \tanh\left(\frac{2(y - (2d - 0.1d\cos(2\pi x/d)))}{W}\right). \quad (25)$$

As specified in Ref. [21], the key parameters are fixed as Re = 2048, At = 0.5, and $\sqrt{gd} = 0.04$. After that, the temporal evolution of the perturbed interface is shown in Figure 9 based on the grids of 512×2048. It is observed that the heavy fluid is downward accelerated by gravity, and it gradually penetrates into the light fluid. At $t^* = 2.0$, the front-end of the heavy fluid evolves to be an umbrella-like shape. As the light fluid is upward pressured, the velocity difference between two fluids triggers KHI, leading to the counter-rotating vortices of the heavy fluid ($t^* = 3.0$). At a later time ($t^* = 5.0$), these two unstable vortices arouse a pair of secondary vortices at the tips of the roll-ups. The obtained interface evolution compares well with those reported in Refs. [21, 24]. Front-positions of the spike (h_s) and bubble (h_b) measured in units of d also agree with the results of He et al. [21], as shown in Figure 10.

The first test confirms the grid resolution and ability of the present model in capturing the feature of RTI under a low density ratio, but the reliability for those with large density ratios at high Reynolds numbers is not sufficiently verified. Thus, in the second benchmark case, we intend to collect more evidence by comparing our simulation with the analytical data [47]. It is argued in Refs. [21, 47] that

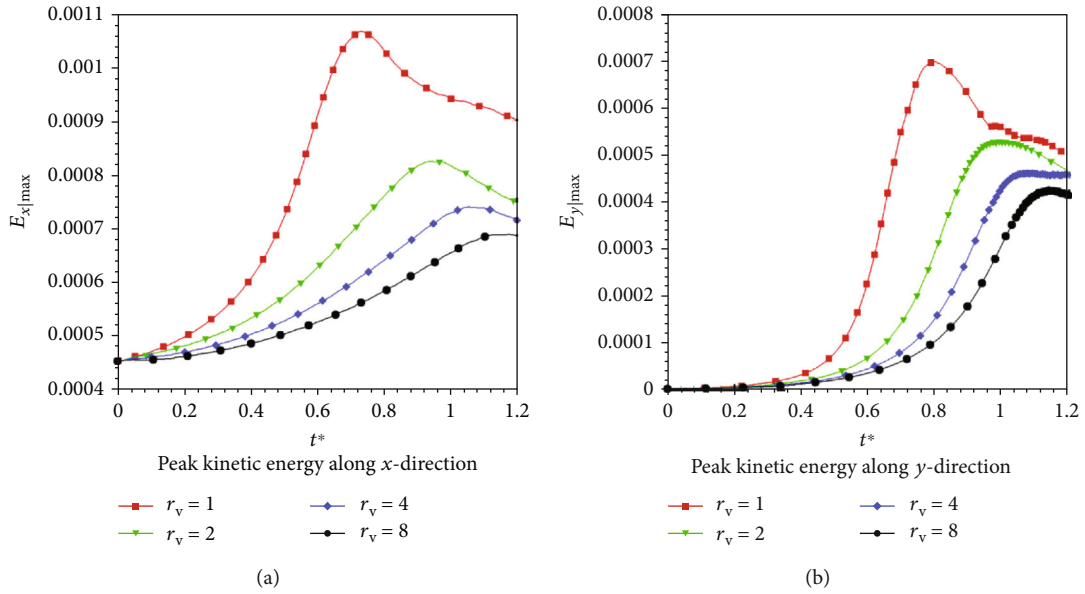

Figure 5: Temporal evolutions of the peak kinetic energy for different viscosity ratios.

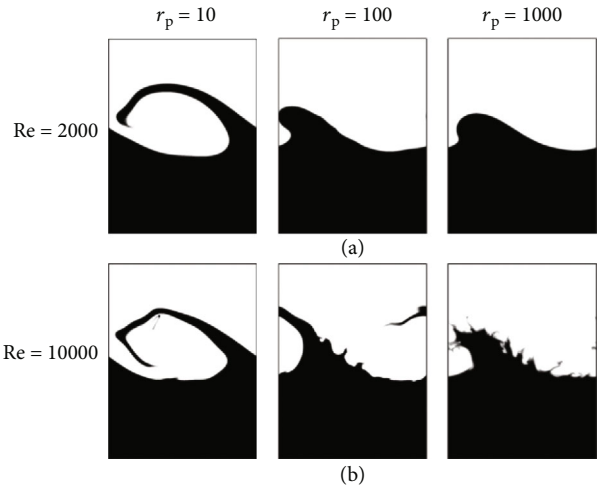

Figure 6: Snapshots of KHI for various density ratios and Reynolds numbers (We = 400, $\nu_A = \nu_B$, and $t^* = 4.0$).

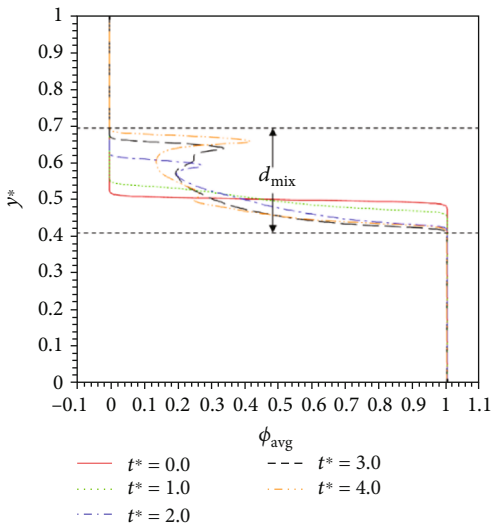

Figure 7: Averaged order parameter profiles against the y-direction at different dimensionless times (Re = 2000, We = 400, and $r_\rho = 10$).

the slightly perturbed interface has an exponential growth in the early stage,

$$a = a_0 e^{\alpha t}, \tag{26}$$

where α is the growth rate, and a is the temporal interface amplitude with its initial value of a_0. For the viscosity-matched fluids with negligible surface tension, the growth rate will be a function of Atwood number and wavenumber ($k = 2\pi/d$). For presenting the results, the dimensionless growth rate and wavenumber are defined as $\alpha^* = \alpha/\sqrt[3]{g^2/\nu}$ and $k^* = k/\sqrt[3]{g/\nu^2}$, respectively. Figure 11 depicts the results of α^* obtained from the present model at At = 0.998 with $0.01 \le k^* \le 2.0$, as well as those predicted by linear theory [47]. In this case, the grids are 512×2048 as well, but the initial interface amplitude is set with a much small value of $a_0 = 0.01d$. Noting that in this case, At = 0.998 represents a

Table 1: Widths of the mixing layer for different density ratios and Reynolds numbers.

Re	d_{mix}			
	$r_\rho = 10$	$r_\rho = 50$	$r_\rho = 100$	$r_\rho = 1000$
2000	0.280	0.250	0.203	0.162
5000	0.427	0.392	0.307	0.266
10000	0.478	0.467	0.341	0.269

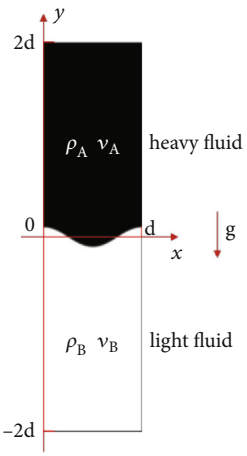

Figure 8: Schematic diagram for Rayleigh-Taylor instability.

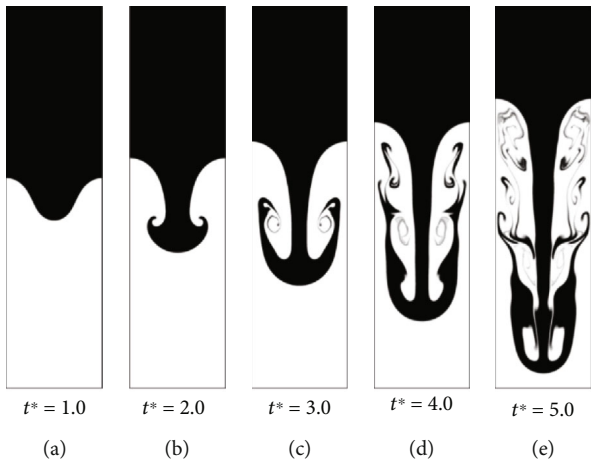

Figure 9: Snapshots of interface evolution for Re = 2048 and At = 0.5.

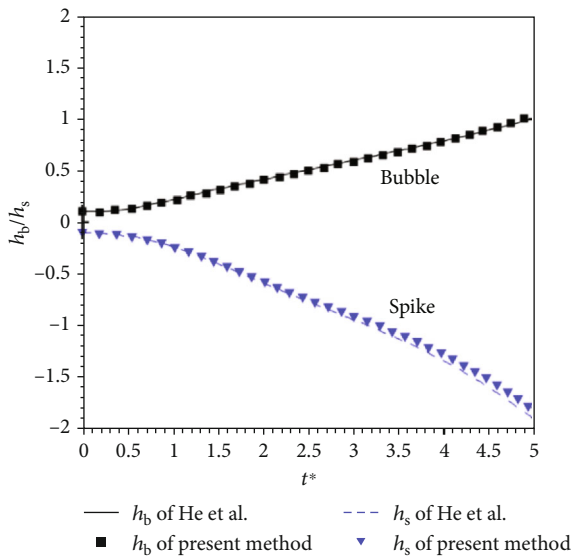

Figure 10: Comparison of the bubble and spike front-positions between present results and those of He et al. [21].

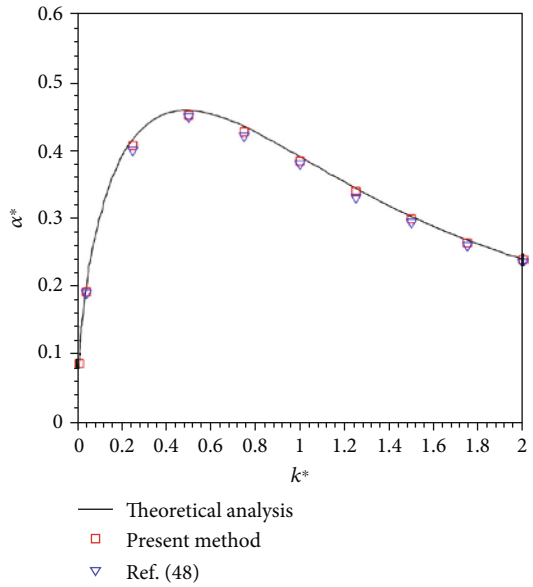

Figure 11: Comparison of the dimensionless growth rate obtained from the numerical methods (symbol) with those predicted by linear theory [47] (solid line).

large density ratio of $\rho_A/\rho_B = 1000$, and $0.01 \le k^* \le 2.0$ indicates the Reynolds number varying in the range of $5.6 \le \mathrm{Re} \le 15749.6$. Compared with the numerical results in Ref. [48], our results are in better agreement with the analytical data [47]. The above results once more demonstrate the ability of the present model in dealing with challenging conditions and also affirm the grid resolution for the following study.

In the above two benchmark cases, the simulation focuses on viscosity-matched fluids. However, the actual fluids generally own a viscosity contrast. Hence, we assess the effects of viscosity ratio ($r_\nu = \nu_B/\nu_A$) on the interface evolution of RTI in this part. To reduce the influence of density ratio, the Atwood number is fixed at At = 0.5. The numerical study then considers four viscosity ratios, including r_ν =1, 2, 4, and 8 at Re = 256 and Re = 2048, respectively.

Figure 12 shows the snapshots of the interface shape of different viscosity ratios for Re = 256 at $t^* = 5.0$. Compared with those in Figure 13 for Re = 2048, the heavy fluid at a low Reynolds number still rolls up as two side spikes, but the spiral vortices are not observed. By increasing the viscosity ratio, it is found out that roll-ups of the heavy fluid and the subsequent spiral vortices are all suppressed. This is due to the enhanced viscous force of the light fluid that reduces the strength of KHI, which is consistent with the results reported in Section 3.2. As plotted in Figures 14 and 15, the viscosity ratio also demonstrates distinct impacts on bubble position and velocity. Here, the bubble velocity u_b is measured in units of $\sqrt{\mathrm{At}gd/(1+\mathrm{At})}$. As seen, the motion of the bubble is restrained with the increasing viscosity ratio and such effects are more evident at a low Reynolds number. The possible reason is that the decrease of vortical effects stemmed from KHI results in a poor acceleration of bubbles.

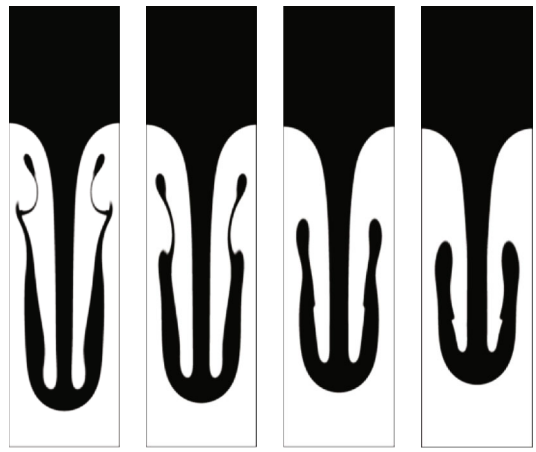

Figure 12: Snapshots of interface shape for different viscosity ratios (Re = 256, At = 0.5, and $t^* = 5.0$).

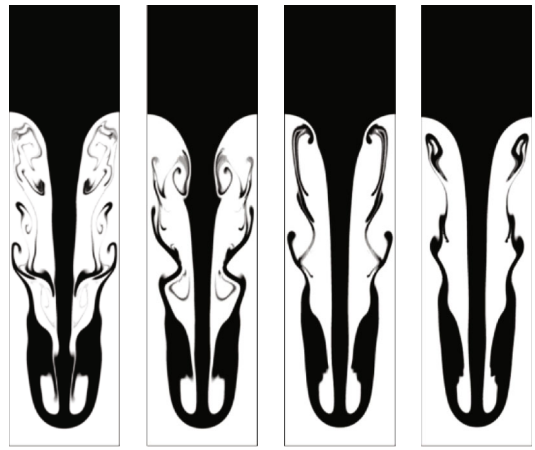

Figure 13: Snapshots of interface shape for different viscosity ratios (Re = 2048, At = 0.5, and $t^* = 5.0$).

Such an adverse impact on the bubble motion happens to be more remarkable when the viscous force dominates the inertia force at a low Reynolds number (Re = 256).

Ultimately, the effects of density ratio ($r_\rho = \rho_A/\rho_B$) on the interface evolution of RTI are investigated with the viscosity ratio fixed at $r_v = 2$. The following study examines four different density ratios (r_ρ =3, 10, 100, and 1000) at Re = 2048 and Re = 10000. As shown in Figure 16, the snapshots of interface at Re = 2048 for different density ratios are captured when the spike-front is close to the bottom wall. For the low density ratios (r_ρ =3 and 10), we can observe the umbrella-like spikes with spiral vortices appearing at the tails of the side roll-ups. By increasing the density ratio to r_ρ =, the roll-ups of heavy fluid shrink to be small fingers, which is in line with the evolving trend predicted in Ref. [21] and the behavior of KHI at moderate density ratios [22]. Once the density ratio reaches a sufficiently large value ($r_\rho = 1000$), the umbrella-like spike-front evolve to be a rocket-like configuration with small serrated waves growing on the spike sides. These small serrated waves are born out of Kelvin-Helmholtz wavelets, which are exactly the characteristics of KHI at large density ratios [45]. Such topological interface deformations are more pronounced at a higher Reynolds number (Re = 10000). As depicted in Figures 17(c) and 17(d), the small-scale ligaments are stretched and then tend to detach from the spikes due to the dominated effects of inertia force under present challenging conditions. This kind of severe breakup pattern is generally observed in the liquid jet at the large density ratio and high Reynolds number [1, 48]. Likewise, we compare the temporal variations of the normalized bubble position and velocity for different

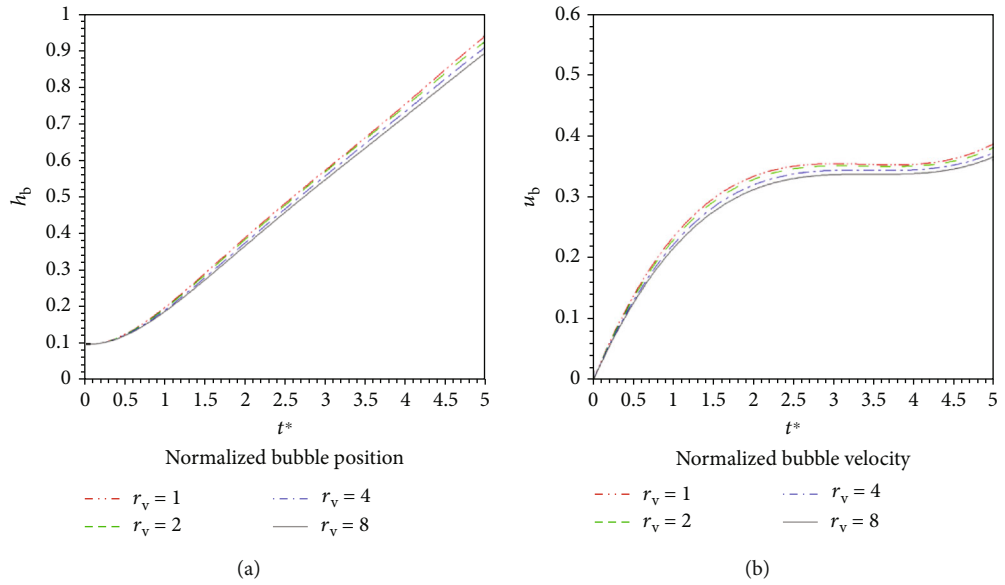

FIGURE 14: Temporal variations of the normalized bubble position and velocity for different viscosity ratios (Re = 256 and At = 0.5).

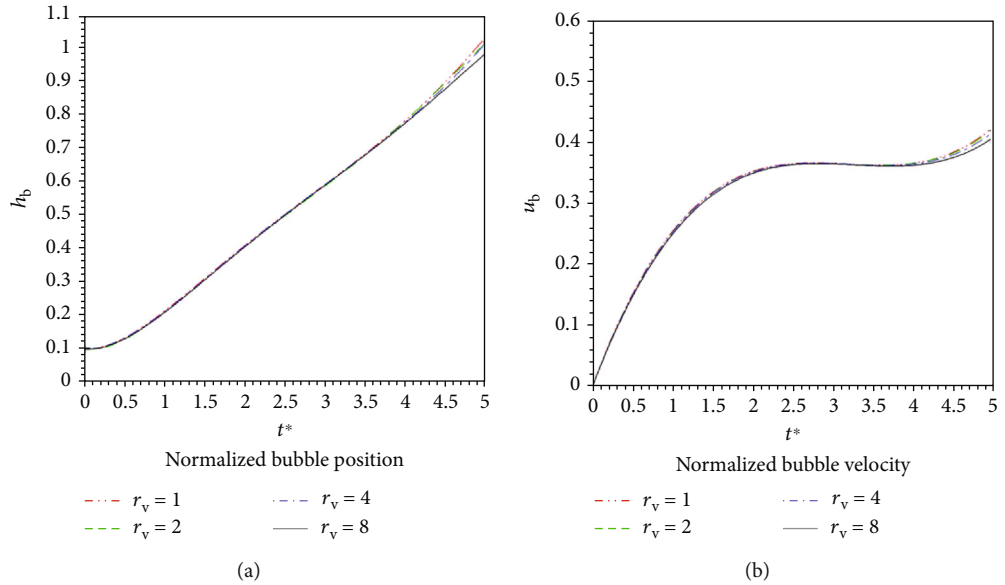

FIGURE 15: Temporal variations of the normalized bubble position and velocity for different viscosity ratios (Re = 2048 and At = 0.5).

density ratios in Figure 18. Apparently, the bubble of light fluid under a larger density ratio grows much faster than those under lower density ratios.

4. Conclusions

Recent studies have revealed that KHI and RTI dominate the processes of liquid sheet breakup and primary atomization. Generally, the liquid and gas own a large density contrast and high Reynolds number in these applications. Hence, the investigations of KHI and RTI by considering the effects of the large density contrast and high Reynolds number have great significance in better understanding the destabilizing mechanism of the liquid layer. Unfortunately, the related investigations of KHI and RTI are rarely conducted in such challenging conditions. To this end, the morphological characteristics of KHI and RTI are inspected in wide ranges of the density ratio, Reynolds number, and viscosity ratio in this paper. First, a lattice Boltzmann MRT model based on the conservative AC equation is reconstructed with necessary modifications, and its numerical ability at challenging conditions is well verified together with sensitive study to the values of mobility. Afterward, the numerical simulations are implemented, and the corresponding results indicate that

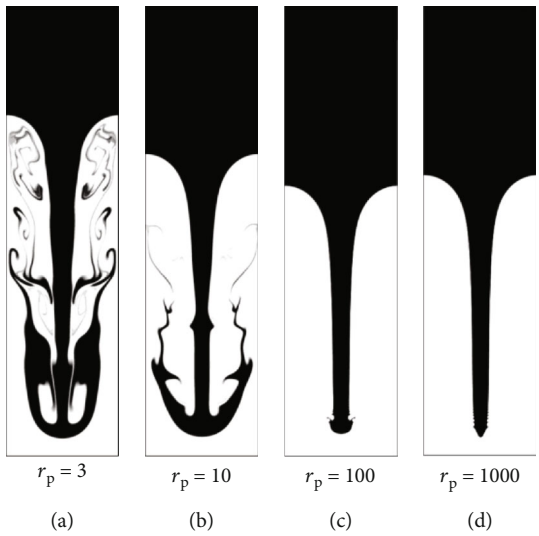

FIGURE 16: Snapshots of interface shape for different density ratios (Re = 2048 and $r_\nu = 2$).

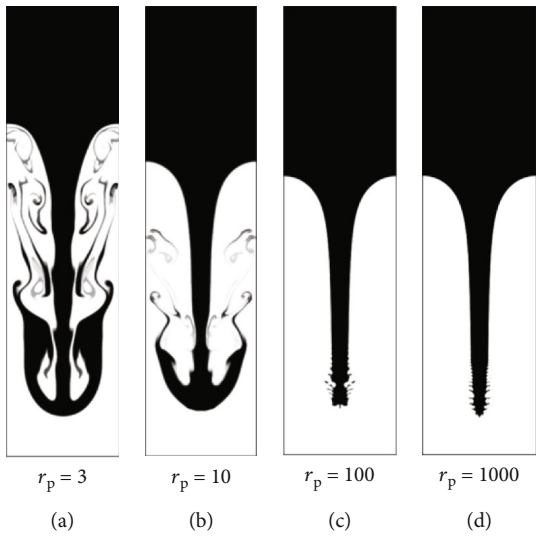

FIGURE 17: Snapshots of interface shape for different density ratios (Re = 10000 and $r_\nu = 2$).

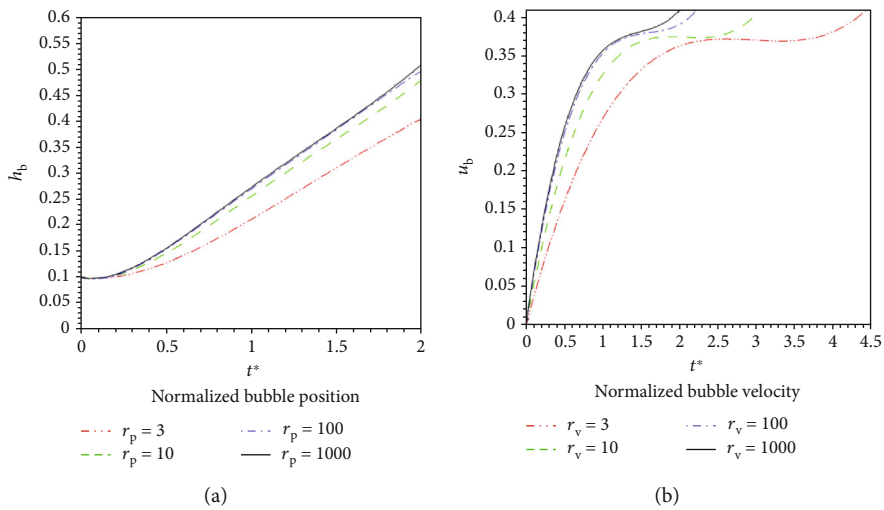

FIGURE 18: Temporal variations of the normalized bubble position and velocity for different density ratios (Re = 10000 and $r_\nu = 2$).

the viscosity ratio and density ratio tend to suppress the interface disturbance, while the Reynolds number favors the fluids interpenetrating. Nonetheless, when the density ratio and the Reynolds number are both increased to large values, the aroused Kelvin-Helmholtz wavelets trigger severe interface evolutions due to the dominated inertia force of heavy fluid. Noting that the aforementioned results of KHI and RTI, particularly, under a large density ratio and high Reynolds number greatly support the typical mechanisms observed in the primary atomization process.

Data Availability

The data used to support the findings of this study are available from the corresponding author upon request.

Conflicts of Interest

The authors declare that they have no conflicts of interest.

Acknowledgments

One of the authors gratefully acknowledges insightful discussions with Dr. Hong Liang. This work was supported by the National Natural Science Foundation of China under Grant No. (51776031) and the Key Project of National Science Foundation of Liaoning Province of China under Grant No. (20170540182).

References

[1] T. Zhang, B. Dong, X. Zhou, L. Guan, W. Li, and S. Zhou, "Experimental study of spray characteristics of kerosene-ethanol blends from a pressure-swirl nozzle," *International Journal of Aerospace Engineering*, vol. 2018, no. 2, pp. 1–14, 2018.

[2] L. Rayleigh, "Investigation of the character of the equilibrium of an incompressible heavy fluid of variable density," *Proceedings of the London Mathematical Society*, vol. s1-14, no. 1, pp. 170–177, 1882.

[3] G. I. Taylor, "The instability of liquid surfaces when accelerated in a direction perpendicular to their planes. I," *Proceedings of the Royal Society of Londo Series A*, vol. 201, no. 1065, pp. 192–196, 1950.

[4] J. C. Lasheras and E. Hopfinger, "Liquid jet instability and atomization in a coaxial gas stream," *Annual Review of Fluid Mechanics*, vol. 32, no. 1, pp. 275–308, 2000.

[5] V. P. Zhukov and M. Feil, "Numerical simulations of the flame of a single coaxial injector," *International Journal of Aerospace Engineering*, vol. 2017, no. 6, pp. 1–11, 2017.

[6] V. Sarychev, S. Nevskii, S. Konovalov, and A. Granovskii, "Modeling of the initial stages of the formation of heterogeneous plasma flows in the electric explosion of conductors," *Current Applied Physics*, vol. 18, no. 10, pp. 1101–1107, 2018.

[7] L. F. Wang, W. H. Ye, Z. F. Fan, Y. J. Li, X. T. He, and M. Y. Yu, "Weakly nonlinear analysis on the Kelvin-Helmholtz instability," *EPL*, vol. 86, no. 1, p. 15002, 2009.

[8] L. Wang, W. Ye, and Y. Li, "Combined effect of the density and velocity gradients in the combination of Kelvin-Helmholtz and Rayleigh-Taylor instabilities," *Physics of Plasmas*, vol. 17, no. 4, p. 042103, 2010.

[9] W. C. Wan, G. Malamud, A. Shimony et al., "Observation of single-mode, Kelvin-Helmholtz instability in a supersonic flow," *Physical Review Letters*, vol. 115, no. 14, p. 145001, 2015.

[10] D. Lewis, "The instability of liquid surfaces when accelerated in a direction perpendicular to their planes. II," *Proceedings of the Royal Society of London Series A*, vol. 202, no. 1068, pp. 81–96, 1950.

[11] H. G. Lee and J. Kim, "Two-dimensional kelvin-Helmholtz instabilities of multi-component fluids," *European Journal of Mechanics-B/Fluids*, vol. 49, pp. 77–88, 2015.

[12] H. D. Ceniceros and A. M. Roma, "Study of the long-time dynamics of a viscous vortex sheet with a fully adaptive non-stiff method," *Physics of Fluids*, vol. 16, no. 12, pp. 4285–4318, 2004.

[13] T. Wei and D. Livescu, "Late-time quadratic growth in single-mode Rayleigh-Taylor instability," *Physical Review E*, vol. 86, no. 4, p. 046405, 2012.

[14] R. Rangel and W. Sirignano, "Nonlinear growth of kelvin-Helmholtz instability: effect of surface tension and density ratio," *Physics of Fluids*, vol. 31, no. 7, pp. 1845–1855, 1988.

[15] J. Fontane and L. Joly, "The stability of the variable-density Kelvin-Helmholtz billow," *Journal of Fluid Mechanics*, vol. 612, pp. 237–260, 2008.

[16] S. Konovalov, X. Chen, V. Sarychev, S. Nevskii, V. Gromov, and M. Trtica, "Mathematical modeling of the concentrated energy flow effect on metallic materials," *Metals*, vol. 7, no. 1, p. 4, 2017.

[17] V. N. Goncharov, "Analytical model of nonlinear, single-mode, classical Rayleigh-Taylor instability at arbitrary Atwood numbers," *Physical Review Letters*, vol. 88, no. 13, p. 134502, 2002.

[18] Y. Yan and Y. Zu, "A lattice Boltzmann method for incompressible two-phase flows on partial wetting surface with large density ratio," *Journal of Computational Physics*, vol. 227, no. 1, pp. 763–775, 2007.

[19] Y. Zu and S. He, "Phase-field-based lattice Boltzmann model for incompressible binary fluid systems with density and viscosity contrasts," *Physical Review E*, vol. 87, no. 4, p. 043301, 2013.

[20] R. Zhang, X. He, G. Doolen, and S. Chen, "Surface tension effects on two-dimensional two-phase kelvin-Helmholtz instabilities," *Advances in Water Resources*, vol. 24, no. 3-4, pp. 461–478, 2001.

[21] X. He, S. Chen, and R. Zhang, "A Lattice Boltzmann Scheme for Incompressible Multiphase Flow and Its Application in Simulation of Rayleigh-Taylor Instability," *Journal of Computational Physics*, vol. 152, no. 2, pp. 642–663, 1999.

[22] A. Fakhari and T. Lee, "Multiple-relaxation-time lattice Boltzmann method for immiscible fluids at high Reynolds numbers," *Physical Review E*, vol. 87, no. 2, p. 023304, 2013.

[23] Y.-B. Gan, A.-G. Xu, G.-C. Zhang, C.-D. Lin, H.-L. Lai, and Z.-P. Liu, "Nonequilibrium and morphological characterizations of Kelvin-Helmholtz instability in compressible flows," *Frontiers of Physics*, vol. 14, no. 4, p. 43602, 2019.

[24] H. Liang, B. C. Shi, Z. L. Guo, and Z. H. Chai, "Phase-field-based multiple-relaxation-time lattice Boltzmann model for incompressible multiphase flows," *Physical Review E*, vol. 89, no. 5, p. 053320, 2014.

[25] Q. Li, K. Luo, and X. Li, "Lattice Boltzmann modeling of multiphase flows at large density ratio with an improved pseudopotential model," *Physical Review E*, vol. 87, no. 5, p. 053301, 2013.

[26] A. Xu, T. S. Zhao, L. An, and L. Shi, "A three-dimensional pseudo-potential-based lattice Boltzmann model for multiphase flows with large density ratio and variable surface tension," *International Journal of Heat and Fluid Flow*, vol. 56, pp. 261–271, 2015.

[27] H. Liang, J. Xu, J. Chen, H. Wang, Z. Chai, and B. Shi, "Phase-field-based lattice Boltzmann modeling of large-density-ratio two-phase flows," *Physical Review E*, vol. 97, no. 3, p. 033309, 2018.

[28] A. Fakhari and D. Bolster, "Diffuse interface modeling of three-phase contact line dynamics on curved boundaries: a lattice Boltzmann model for large density and viscosity ratios," *Journal of Computational Physics*, vol. 334, pp. 620–638, 2017.

[29] Z. Chai, D. Sun, H. Wang, and B. Shi, "A comparative study of local and nonlocal Allen-Cahn equations with mass conservation," *International Journal of Heat and Mass Transfer*, vol. 122, pp. 631–642, 2018.

[30] H. L. Wang, Z. H. Chai, B. C. Shi, and H. Liang, "Comparative study of the lattice Boltzmann models for Allen-Cahn and Cahn-Hilliard equations," *Physical Review E*, vol. 94, no. 3, p. 033304, 2016.

[31] P. Chiu and Y. Lin, "A conservative phase field method for solving incompressible two-phase flows," *Journal of Computational Physics*, vol. 230, no. 1, pp. 185–204, 2011.

[32] H. Liang, H. Liu, Z. Chai, and B. Shi, "Lattice Boltzmann method for contact-line motion of binary fluids with high density ratio," *Physical Review E*, vol. 99, no. 6, p. 063306, 2019.

[33] Z. Guo and C. Zheng, "Analysis of lattice Boltzmann equation for microscale gas flows: relaxation times, boundary conditions and the Knudsen layer," *International Journal of Computational Fluid Dynamics*, vol. 22, no. 7, pp. 465–473, 2008.

[34] Q. Li, Y. L. He, G. H. Tang, and W. Q. Tao, "Improved Axisymmetric Lattice Boltzmann Scheme," *Physical Review E*, vol. 81, no. 5, p. 056707, 2010.

[35] M. Zhang, W. Zhao, and P. Lin, "Lattice Boltzmann method for general convection-diffusion equations: MRT model and boundary schemes," *Journal of Computational Physics*, vol. 389, pp. 147–163, 2019.

[36] J. Kim, "A continuous surface tension force formulation for diffuse-Interface models," *Journal of Computational Physics*, vol. 204, no. 2, pp. 784–804, 2005.

[37] F. Ren, B. Song, M. C. Sukop, and H. Hu, "Improved lattice Boltzmann modeling of binary flow based on the conservative Allen-Cahn equation," *Physical Review E*, vol. 94, no. 2, p. 023311, 2016.

[38] Q. Li, K. H. Luo, Y. J. Gao, and Y. L. He, "Additional interfacial force in lattice Boltzmann models for incompressible multiphase flows," *Physical Review E*, vol. 85, no. 2, p. 026704, 2012.

[39] T. Lee and L. Liu, "Lattice Boltzmann simulations of micron-scale drop impact on dry surfaces," *Journal of Computational Physics*, vol. 229, no. 20, pp. 8045–8063, 2010.

[40] B. Shi and Z. Guo, "Lattice Boltzmann model for nonlinear convection-diffusion equations," *Physical Review E*, vol. 79, no. 1, p. 016701, 2009.

[41] X. Yang, X. Zhang, Z. Li, and G. W. He, "A smoothing technique for discrete delta functions with application to immersed boundary method in moving boundary simulations," *Journal of Computational Physics*, vol. 228, no. 20, pp. 7821–7836, 2009.

[42] T. Zhang, B. Shi, Z. Guo, Z. Chai, and J. Lu, "General bounce-back scheme for concentration boundary condition in the Lattice-Boltzmann method," *Physical Review E*, vol. 85, no. 1, p. 016701, 2012.

[43] W. Tauber, S. O. Unverdi, and G. Tryggvason, "The nonlinear behavior of a sheared immiscible fluid interface," *Physics of Fluids*, vol. 14, no. 8, pp. 2871–2885, 2002.

[44] Y. Gan, A. Xu, G. Zhang, and Y. Li, "Lattice Boltzmann study on Kelvin-Helmholtz instability: roles of velocity and density gradients," *Physical Review E*, vol. 83, no. 5, p. 056704, 2011.

[45] A. Fakhari, M. Geier, and T. Lee, "A mass-conserving lattice Boltzmann method with dynamic grid refinement for immiscible two-phase flows," *Journal of Computational Physics*, vol. 315, pp. 434–457, 2016.

[46] T. Deng, W. Chen, X. Ren, S. Jiang, and C. H. Yuan, "Experiment on the breakup of liquid jets in different cross-airflows," *International Journal of Aerospace Engineering*, vol. 2019, no. 7, pp. 1–13, 2019.

[47] B. Schott, U. Rasthofer, V. Gravemeier, and W. A. Wall, "A face-oriented stabilized Nitsche-type extended variational multiscale method for incompressible two-phase flow," *International Journal for Numerical Methods in Engineering*, vol. 104, no. 7, pp. 721–748, 2015.

[48] H. Amirshaghaghi, M. H. Rahimian, H. Safari, and M. Krafczyk, "Large Eddy simulation of liquid sheet breakup using a two-phase lattice Boltzmann method," *Computers & Fluids*, vol. 160, pp. 93–107, 2018.

Hindawi
International Journal of Aerospace Engineering
Volume 2020, Article ID 3945463, 12 pages
https://doi.org/10.1155/2020/3945463

Research Article

A CFD-Compatible Amplification Factor Transport Equation for Oblique Tollmien-Schlichting Waves in Supersonic Boundary Layers

JiaKuan Xu,[1] **Lei Qiao**,[2] **and Junqiang Bai**[2]

[1]*Department of Mathematics, Imperial College London, SW7 2AZ, UK*
[2]*School of Aeronautics, Northwestern Polytechnical University, 710072, China*

Correspondence should be addressed to Junqiang Bai; junqiang@nwpu.edu.cn

Received 28 November 2019; Revised 12 February 2020; Accepted 18 February 2020; Published 14 March 2020

Academic Editor: Antonio Viviani

Boundary layer transition is a hot research topic in fluid mechanics and aerospace engineering. In low-speed flows, two-dimensional Tollmien-Schlichting (T-S) waves always dominate the flow instability, which has been modeled by Coder and Maughmer from 2013. However, in supersonic flows, three-dimensional oblique Tollmien-Schlichting waves become dominant in flow instability. Inspired by Coder and Maughmer's N_{TS} amplification factor transport equation for two-dimensional Tollmien-Schlichting waves in low-speed flows and Kroo and Sturdza's linear stability theory (LST) analysis results for oblique Tollmien-Schlichting waves in supersonic flows, a new amplification factor transport equation for oblique Tollmien-Schlichting waves has been developed based on LST. The compressible Falkner-Skan similarity equations are introduced to build the relationships between nonlocal variables and local variables so that all the variables used in the present model can be calculated using local variables. Applications of this new transport equation to the flows over supersonic flat plate, 3% thick biconvex airfoil, and one modified supersonic laminar airfoil show promising results compared with the standard LST analysis results.

1. Introduction

Since laminar flow has less drag than turbulent flow, laminar flow design technology has been a research hotspot in energy conservation of the green aviation [1]. In the process of laminar flow design, the accuracy of transition prediction plays a crucial role on the design effect. Therefore, it is very important and meaningful for aircraft designers to pay close attention to smart and efficient transition prediction methods. In recent years, there are two main routes to predict transition for airplanes and other complex aerodynamic configurations. One is the local transition models established by experimental data and stability analysis results, such as Menter et al.'s $\gamma - \overline{\mathrm{Re}_{\theta t}}$ correlation-based transition model [2–4], Walters et al.'s k-k_L-ω model based on laminar kinetic energy mechanism [5, 6], Fu and Wang's k-ω-γ transition model for high-speed flows [7], and Xu et al.'s physical mode-based transition models [8–11]. These models play an important role to predict transition for three-dimensional complex aerodynamic flows. The advantages of these transition models are local, convenient, efficient, and compatible with CFD parallel computations. The disadvantage is relying too much on experimental data and empirical parameters.

Compared with the local transition models mentioned above, in the 1950s, a semiempirical method named e^N based on linear stability theory, proposed by Smith and Gamberoni [12] and Van Ingen [13], is widely used to predict transition in industry aerodynamic applications [14]. This LST-based method has been chosen for transition prediction in subsonic and transonic boundary layers by Boeing Inc., Airbus Inc., German Aerospace Center (DLR), National Aeronautics and Space Administration (NASA), France Aerospace Center (ONERA), etc. Subsequently, the e^N

method was simplified by Drela and Giles [15] based on LST analysis results of similarity solutions for laminar flow. This simplified method built the functions between the most unstable amplification factor and the streamwise boundary layer shape factor H_{12}, which has been implemented into the famous airfoil design soft "*X-foil*" [16]. With the development of CFD technique, Krimmelbein and Krumbein [17], Bégou et al. [18], Pascal et al. [19], and Shi et al. [20] coupled the LST-based e^N method with Reynolds-averaged Navier-Stokes (RANS) code. This kind of coupling is reliable, but it is still complex because it also needs to solve boundary layer equations and linear stability theory equations, to integrate the eigenvalues, and to search nonlocal flow variables at the edge of boundary layers.

Based on Drela's idea, Coder and Maughmer [21] established an amplification factor transport equation to solve the amplification factor based on the approximate envelope method, which was extended using new local pressure gradient parameters [22, 23] recently. This transition model can predict the two-dimensional Tollmien-Schlichting (T-S) instabilities and laminar separation bubble- (LSB-) induced transition in low-speed flows. It is worth mentioning that this transport equation for N_{TS} factor combines the advantages of e^N method and local transition models. All the variables in Coder and Maughmer's transport equation can be calculated using local flow variables so that it can be compatible with modern CFD codes conveniently, especially for unstructured codes.

In 2016, Xu et al. [24] constructed a transport equation for amplification factor of crossflow waves, which is restricted to winglike geometries. In 2019, Xu et al. [25] established a local amplification factor transport equation for crossflow instability in low-speed boundary layers, which performs well in several classical transition prediction cases. Hence, it is time to develop this modeling idea to high-speed flows. As known, in subsonic and low-transonic flows, two-dimensional T-S waves dominate the T-S instabilities. However, in supersonic boundary layers, oblique T-S waves play a dominant role [25]. In this paper, we are trying to build a brand new amplification factor transport equation for the oblique T-S waves in supersonic flows. Because the instability mechanism of two-dimensional T-S waves and oblique T-S waves is different, the present transport equation only has the similar form but different content compared with Coder's transport equation. Note that all the nonlocal variables are fitted using the solution database of compressible Falkner-Skan similarity equations. Since a suitable critical value of amplification factor can be found in the flows below Mach number 3.0 using Mack's relations [14, 26, 27] with freestream turbulence intensity, the present work is very valuable and meaningful for natural laminar flow (NLF) optimizations of supersonic airfoils and wings.

2. Modeling of the Transport Equation

2.1. Compressible Falkner-Skan Similarity Equations. In order to localize the nonlocal variables, two-dimensional compressible similarity equations are introduced to build the relation functions.

$$\begin{cases} \xi = \displaystyle\int_0^x \rho_{\mathrm{e}} U_{\mathrm{e}} \mu_{\mathrm{e}} dx, \\ \eta = \dfrac{U_{\mathrm{e}}}{\sqrt{2\xi}} \displaystyle\int_0^y \rho dy = \sqrt{\dfrac{\rho_{\mathrm{e}} U_{\mathrm{e}}}{2\mu_{\mathrm{e}} x}} \int_0^y \dfrac{\rho}{\rho_{\mathrm{e}}} dy. \end{cases} \tag{1}$$

With Illingworth transformation, the two-dimensional boundary equations can be written as [28]

$$\begin{aligned} &\left(\frac{\rho\mu}{\rho_{\mathrm{e}}\mu_{\mathrm{e}}} f''\right)' + ff'' + \beta_{\mathrm{H}}\left(\frac{\rho_{\mathrm{e}}}{\rho} - f'^2\right) = 0, \\ &\left(\frac{1}{\mathrm{Pr}} \frac{\rho\mu}{\rho_{\mathrm{e}}\mu_{\mathrm{e}}} g'\right)' + fg' + (\gamma_{\mathrm{H}} - 1) M_{\mathrm{e}}^2 \frac{\rho\mu}{\rho_{\mathrm{e}}\mu_{\mathrm{e}}} f''^2 \\ &\qquad + (\gamma_{\mathrm{H}} - 1) M_{\mathrm{e}}^2 f' \beta\left(f'^2 - g\right) = 0, \end{aligned} \tag{2}$$

subject to the boundary conditions

$$\begin{aligned} &\eta = 0 \longrightarrow f = f' = 0,\ g = g_{\mathrm{w}} \left(\text{or } g' = 0 \text{ for adiabatic wall}\right), \\ &\eta = \infty \longrightarrow f' = 1,\ g = 1. \end{aligned} \tag{3}$$

In the equations above, $f' = u/U_{\mathrm{e}}$ and $g = T/T_{\mathrm{e}}$ indicate the velocity profile and temperature profile, respectively. $\beta_{\mathrm{H}} = (2\xi/U_{\mathrm{e}})(dU_{\mathrm{e}}/d\xi)$ is the Falkner-Skan pressure gradient parameter, Pr is the Prandtl number, γ_{H} is the ratio of specific heats, M is the Mach number, ρ is the density, and μ is the dynamic viscosity. Note that the subscript "e" means the variables at the edge of boundary layer.

2.2. Transport Equation Description for Oblique T-S Waves. Firstly, the transport equation takes the form

$$\begin{aligned} \frac{\partial(\rho N_{\mathrm{TS}})}{\partial t} + \frac{\partial(\rho u_i N_{\mathrm{TS}})}{\partial x_i} &= \rho S F_{\mathrm{crit}} F_{\mathrm{growth}} \frac{dN_{\mathrm{TS}}}{d\,\mathrm{Re}_\theta} \\ &\quad + \frac{\partial}{\partial x_i}\left[(\mu + \mu_t)\frac{\partial N_{\mathrm{TS}}}{\partial x_i}\right], \end{aligned} \tag{4}$$

where S is the strain rate magnitude, F_{crit} indicates the onset function, F_{growth} stands for the development function of growth rate, and $dN_{\mathrm{TS}}/d\,\mathrm{Re}_\theta$ represents the slop of the amplification factor N_{TS} and momentum thickness Reynolds number Re_θ. The source term is mainly established based on the extensive linear stability analysis results by Kroo and Sturdza [29] for oblique T-S waves in supersonic flows. The details can be found in Ref. [29].

Secondly, the onset function, F_{crit}, is given by

$$F_{\mathrm{crit}} = \begin{cases} 0, & \mathrm{Re}_\theta < \mathrm{Re}_{\theta,\mathrm{crit}}, \\ 1, & \mathrm{Re}_\theta \geq \mathrm{Re}_{\theta,\mathrm{crit}}, \end{cases} \tag{5}$$

where $\mathrm{Re}_{\theta,\mathrm{crit}}$ is the critical momentum thickness Reynolds number with the following expressions [29]:

$$\log_{10}\left(\frac{\mathrm{Re}_{\theta,\mathrm{crit}}}{K_0^{0.7}}\right) = \left(\frac{1.415}{H_\mathrm{k}-1} - 0.489\right)\tanh\left(\frac{20}{H_\mathrm{k}-1} - 12.9\right) + \frac{3.295}{H_\mathrm{k}-1} + 0.44,$$
$$K_0 = \frac{2}{\pi}\tan^{-1}\left(10\frac{T_\mathrm{w}}{T_\mathrm{e}} - 10\right) + 1,$$
$$\frac{T_\mathrm{w}}{T_\mathrm{e}} = \left(1 + \frac{\gamma_\mathrm{H}-1}{2}\sqrt{\mathrm{Pr}}M_\mathrm{e}^2\right). \quad (6)$$

Here, H_k, proposed by Drela and Giles [15] and defined as $H_\mathrm{k} = \int(1-u/U_\mathrm{e})dy/\int(1-u/U_\mathrm{e})u/U_\mathrm{e}dy$, means the kinematic shape parameter.

Thirdly, the function F_growth is similar to Drela and Giles's [15] and Coder and Maughmer's [21] formulations:

$$F_\mathrm{growth} = D(H_\mathrm{k})\frac{[1+m(H_\mathrm{k})l(H_\mathrm{k})]}{2}, \quad (7)$$

where

$$D(H_\mathrm{k}) = \frac{2.775H_\mathrm{k} - 2.083}{H_\mathrm{k} - 1.948},$$
$$l(H_\mathrm{k}) = \frac{6.54H_\mathrm{k} - 14.07}{H_\mathrm{k}^2}, \quad (8)$$
$$m(H_\mathrm{k}) = \left[0.058\frac{(H_\mathrm{k}-4)^2}{H_\mathrm{k}-1} - 0.068\right]\frac{1}{l(H_\mathrm{k})}.$$

The functions $l(H_\mathrm{k})$ and $m(H_\mathrm{k})$ have the same expressions with Drela and Giles's formulations. The $D(H_\mathrm{k})$ correlation is developed to modify the behavior of the source term at various kinematic shape parameters through lots of calibrations.

Fourthly, the slope function is modeled as

$$\frac{dN_\mathrm{TS}}{d\,\mathrm{Re}_\theta} = \frac{0.01K_1}{K_\mathrm{b}}\{[2.4H_\mathrm{k}K_\mathrm{a} - 3.7 + 2.5K_\mathrm{c}\tanh(1.5H_\mathrm{k} - 4.65)]^2 + 0.125 + K_\mathrm{d} - K_\mathrm{m}\},$$
$$K_1 = 0.5463\left(0.4811\frac{T_\mathrm{w}}{T_\mathrm{e}} + 1\right),$$
$$K_\mathrm{a} = 1 + 0.2(H_\mathrm{k} - 2.5918)\left(1 - \frac{T_\mathrm{e}}{T_\mathrm{w}}\right),$$
$$K_\mathrm{b} = 4.7\left(\frac{T_\mathrm{w}}{T_\mathrm{e}} - 1\right) + 1,$$
$$K_\mathrm{c} = \frac{T_\mathrm{w}}{T_\mathrm{e}},$$
$$K_\mathrm{d} = 1.2\left(\frac{T_\mathrm{w}}{T_\mathrm{e}} - 1\right)^{3/2}, \quad (9)$$

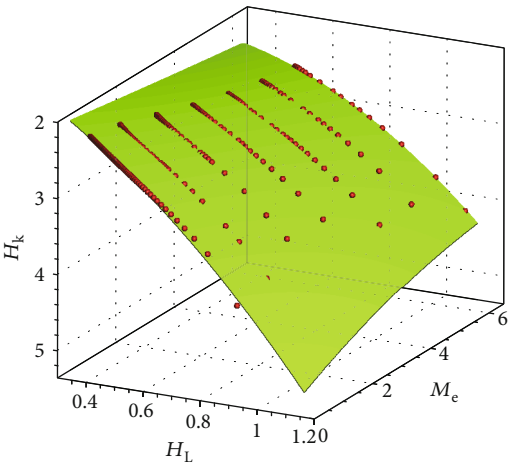

Figure 1: Relations among M_e, H_L, and H_k.

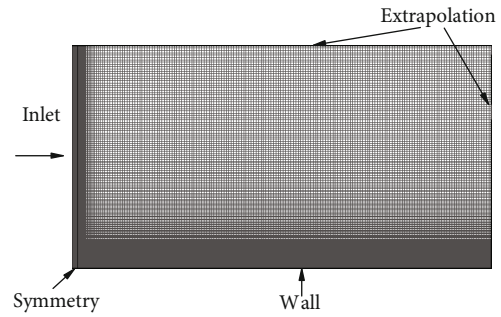

Figure 2: CFD mesh and boundary conditions.

where K_1, K_a, K_b, K_c, and K_d are all the compressibility correction coefficients and T_w is the wall temperature. It is worth mentioning that K_m means the history effect. Kroo and Sturdza use $K_\mathrm{m} = 11.5\sqrt{T_\mathrm{w}/T_\mathrm{e}}(H_\mathrm{k_avg} - H_\mathrm{k})$and $H_\mathrm{k\_avg} = (1/s - s_0)\int_{s_0}^{s} H_\mathrm{k}ds$ to calculate K_m, which is very difficult to compute using local variables. For the integral, transport equation with additional source term can be applied. However, it seems very difficult to compute the average of upstream parameter H_k using local variables. Therefore, in this paper, the history effect term is set as zero temporarily and this term will be developed in the next step.

Not only two-dimensional T-S waves but also three-dimensional oblique T-S waves are stabilized by favorable pressure gradient and increase near the adverse pressure gradient region. It should be mentioned that the H_k ranges from 2.5 to 3.0 for these formulations above, which means this transport equation can only be used to describe the development of pure oblique T-S waves in the supersonic flows with moderate favorable pressure gradient and adverse pressure gradient. For the flows with strong favorable pressure gradient, like the stagnation point flows around blunt leading edge, subsonic regions always appear so that H_k exceeds the current modeling scope. The present model cannot predict the two-dimensional T-S waves which are different from the oblique T-S waves.

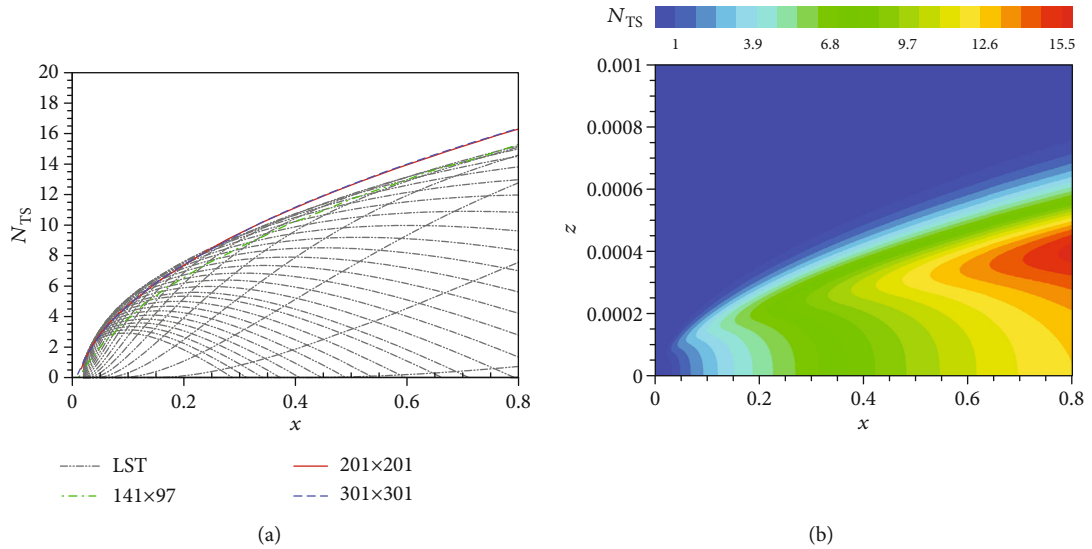

FIGURE 3: Predicted results of amplification factor. (a) Comparison with standard LST analysis results. (b) Contour at Mach number = 2.2 and Reynolds number = 5.6×10^7/m.

Fifthly, after filtering the existing parameters to describe the pressure gradient, the local parameter $H_L = Sy/U_e$, proposed by Coder and Maughmer [21], was adopted to calculate the kinematic shape parameter H_k. In the definition, y is the distance to the nearest wall. Figure 1 plots the function among Mach number M_e, H_L, and H_k, which is obtained by similarity solutions and can be formulated as

$$\begin{aligned} H_k = {} & 1.261 + 0.2083M_e - 0.006437M_e^2 - 0.00006606M_e^3 \\ & + 0.0184M_e^2H_L + 0.06087M_eH_L^2 - 0.449M_eH_L \\ & + 1.407H_L^2 + 1.658H_L. \end{aligned} \tag{10}$$

Sixthly, Xu et al.'s engineering estimation method [9] for Mach number at the edge of boundary layer is chosen, which has the expressions as follows:

$$\left(\frac{\gamma_H}{\gamma_H - 1}\right)\frac{P_\infty}{\rho_\infty} + \frac{U_\infty^2}{2} = \left(\frac{\gamma_H}{\gamma_H - 1}\right)\frac{P}{\rho_e} + \frac{U_e^2}{2}, \tag{11}$$

$$\frac{a_\infty^2}{\gamma_H - 1} + \frac{U_\infty^2}{2} = \frac{a_e^2}{\gamma_H - 1} + \frac{U_e^2}{2}, \tag{12}$$

where a stands for the sound speed, P is the pressure, and the subscript ∞ denotes variables in freestream. Furthermore, ρ_e could be given by $\rho_e = [(\rho_\infty^{\gamma_H}/P_\infty)P]^{1/\gamma_H}$ and the Mach number at the edge of boundary layer is determined as $M_e = U_e/a_e$. In some nonlocal models, M_e can be obtained through searching operations. However, through the aerodynamic equations (11) and (12), it can get a relatively accurate estimation of M_e, which is much more accurate than using the freestream Mach number M_∞ directly. It should point out that the prediction of M_e is a CFD issue, which can be computed by the aerodynamic formulations and CFD variables. This part does not belong to the transition modeling content.

Finally, the last unknown parameter is the local momentum thickness Reynolds number $\mathrm{Re}_\theta = \rho U_e\theta/\mu$. From the similarity solution database, the relationship between Re_θ and the vorticity Reynolds number $\mathrm{Re}_V = \rho Sy^2/\mu$ is described as

$$\Theta(M_e) = \frac{\mathrm{Re}_V}{2.193\ \mathrm{Re}_\theta} = 1 + \frac{(\gamma_H - 1)}{2}M_e^2. \tag{13}$$

Since there is a small height difference between the maximum value of Re_V and H_L in favorable pressure gradient boundary layers, a minor height correction is introduced:

$$\mathrm{Re}_\theta = \mathrm{Re}_\theta\left[1.086\exp\left(0.3455\lambda_\theta'\right) + 0.01279\exp\left(18.28\lambda_\theta'\right)\right], \tag{14}$$

where $\lambda_\theta = (\rho\theta^2/\mu)(dU_e/ds)$ is the Thwaites pressure gradient factor and λ_θ' can be computed using the following equations [25, 30]:

$$\begin{aligned} \theta &= \frac{\max\left(d^2S\right)}{2.2U_e\Theta(M_e)}, \\ \frac{dU_e}{ds} &= \frac{u}{U}\frac{dU_e}{dx} + \frac{v}{U}\frac{dU_e}{dy} + \frac{w}{U}\frac{dU_e}{dz}, \\ \frac{dU_e}{dx_i} &= \frac{1}{U_e\rho_\infty}\left(\frac{P}{P_\infty}\right)^{-1/\gamma_H}\frac{dP}{dx_i}, \\ \lambda_\theta' &= \lambda_\theta\left(1 + \frac{(\gamma_H - 1)}{2}M_e^2\right). \end{aligned} \tag{15}$$

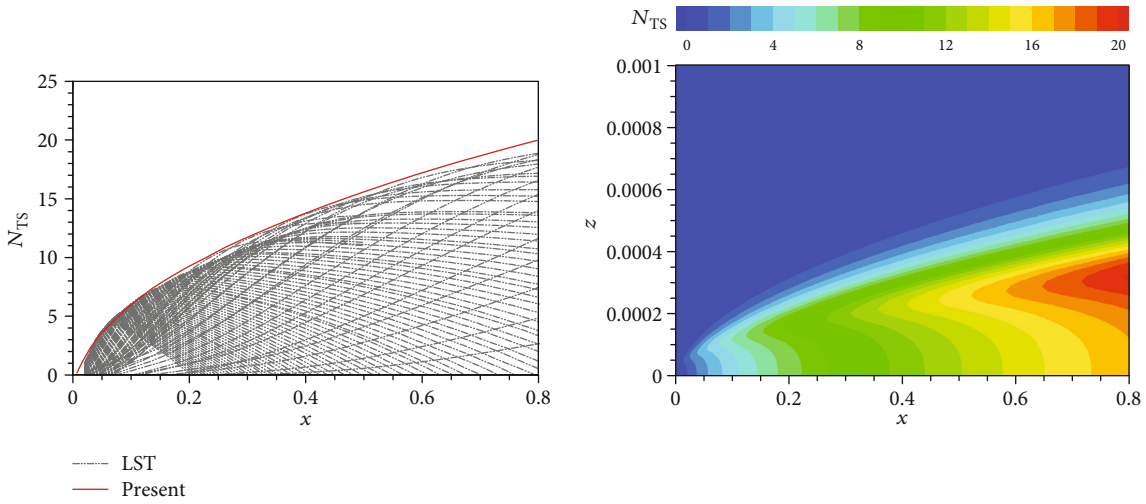

FIGURE 4: Predicted results of amplification factor. (a) Comparison with standard LST analysis results. (b) Contour at Mach number = 1.5 and Reynolds number = 5.4×10^7/m.

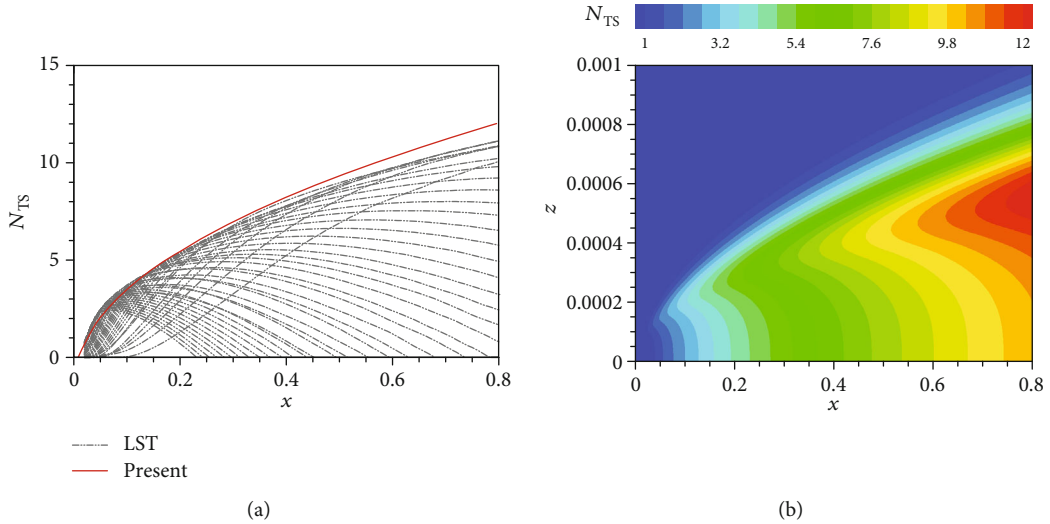

FIGURE 5: Predicted results of amplification factor. (a) Comparison with standard LST analysis results. (b) Contour at Mach number = 2.2 and Reynolds number = 3.0×10^7/m.

Note that the incompressibility correction for λ_θ comes from Ref. [31] and λ_θ' corresponds to the modified Thwaites pressure gradient factor.

Finally, the effective intermittency factor takes the form

$$\gamma_{\text{eff}} = \max\left\{\gamma, \exp\left[2 \max\left(N_{\text{TS}} - N_{\text{TS,crit}}\right)\right]\right\}, \tag{16}$$

where γ is the intermittency factor and the effective intermittency factor γ_{eff} is used to trigger transition in the turbulence model. The coupling way between the transition model and the Menter's Shear Stress Transport (SST) turbulence model from Coder and Maughmer's paper [32] in 2013 is selected in this paper, which is given by

$$\begin{aligned}\frac{\partial(\rho k)}{\partial t} + \frac{\partial(\rho u_i k)}{\partial x_i} &= \gamma_{\text{eff}} P_{k,\text{original}} \\ &\quad - \min\left(\max\left(\gamma_{\text{eff}}, 0.1\right), 1.0\right) D_{k,\text{original}} \\ &\quad + \frac{\partial}{\partial x_i}\left[\left(\mu + \sigma_k \mu_t\right)\frac{\partial k}{\partial x_i}\right].\end{aligned} \tag{17}$$

Note that γ_{eff} is the switch function for the generation of turbulent kinetic energy by the production term $P_{k,\text{original}}$ and the destruction term $D_{k,\text{original}}$ in the SST turbulence model. For comparison, the saddle point method, proposed by Cebeci and Stewartson [33], is adopted for the standard LST analysis.

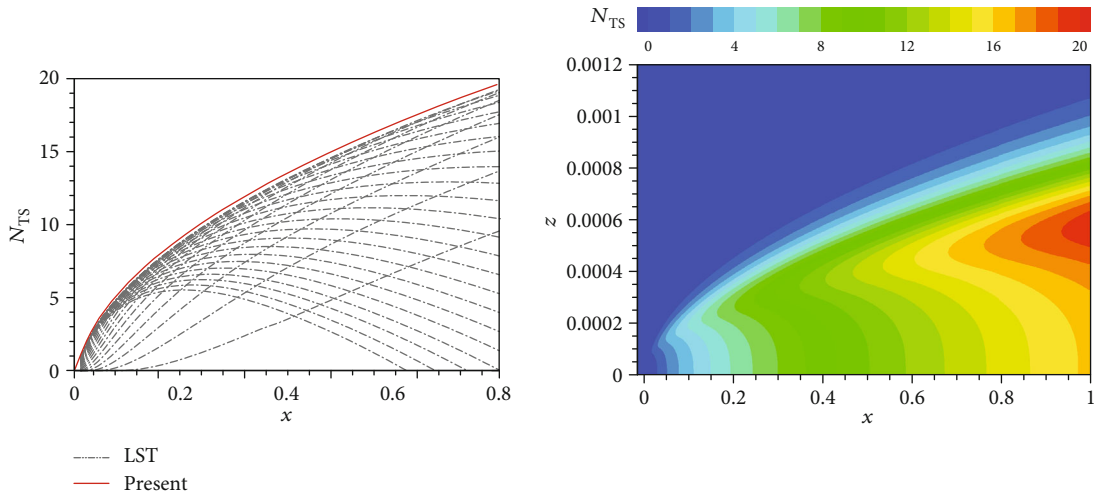

Figure 6: Predicted results of amplification factor. (a) Comparison with standard LST analysis results. (b) Contour at Mach number = 3.0 and Reynolds number = 5.6×10^7/m.

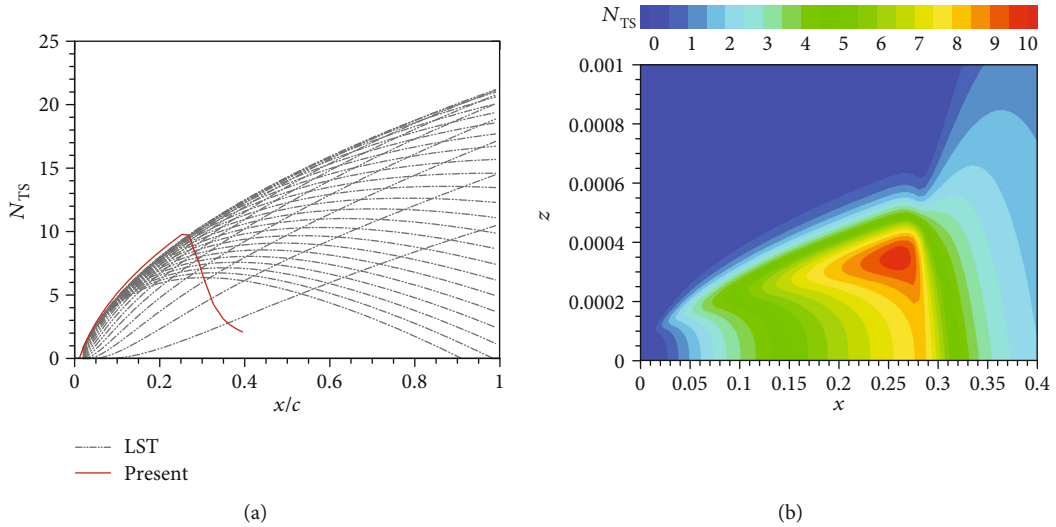

Figure 7: Predicted results of amplification factor (a) Comparison with standard LST analysis results; (b) contour at Mach number = 3.5 and Reynolds number = 5.89×10^7/m.

3. Results and Discussion

In the present work, the open-source structured Reynolds-averaged Navier-Stokes solver named CFL3D was used as the basic flow solver. Details of this solver could be found in NASA's website (data available online at https://cfl3d.larc.nasa.gov/) and documents [34]. In this work, all of the transition prediction results were obtained by the present transport equation coupling with Menter's k-ω SST turbulence model.

3.1. Validation Test Case 1: Supersonic Flat Plate. The first case is the zero-pressure-gradient supersonic flat plate. The basic mesh with boundary conditions for the following computations is shown in Figure 2. At first, the 149×97-point mesh, 201×201-point mesh, and 301×301-point mesh are

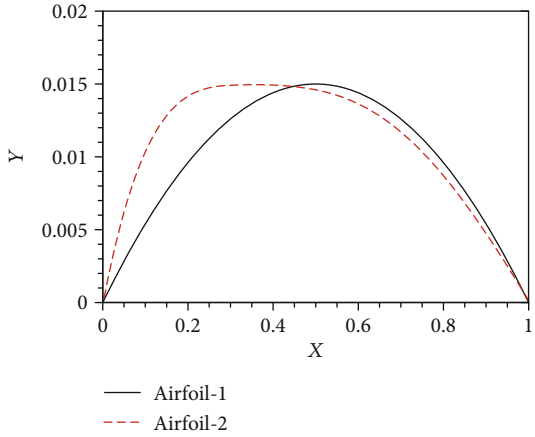

Figure 8: Supersonic airfoils.

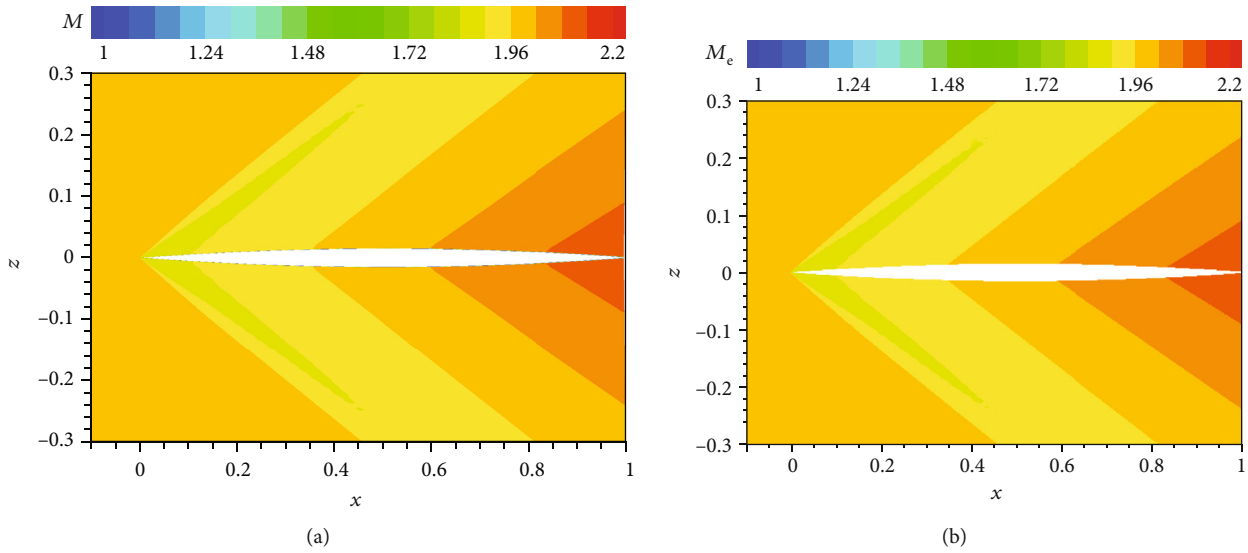

Figure 9: Comparison between (a) local Mach number and (b) predicted M_e with angle of attack of 0°.

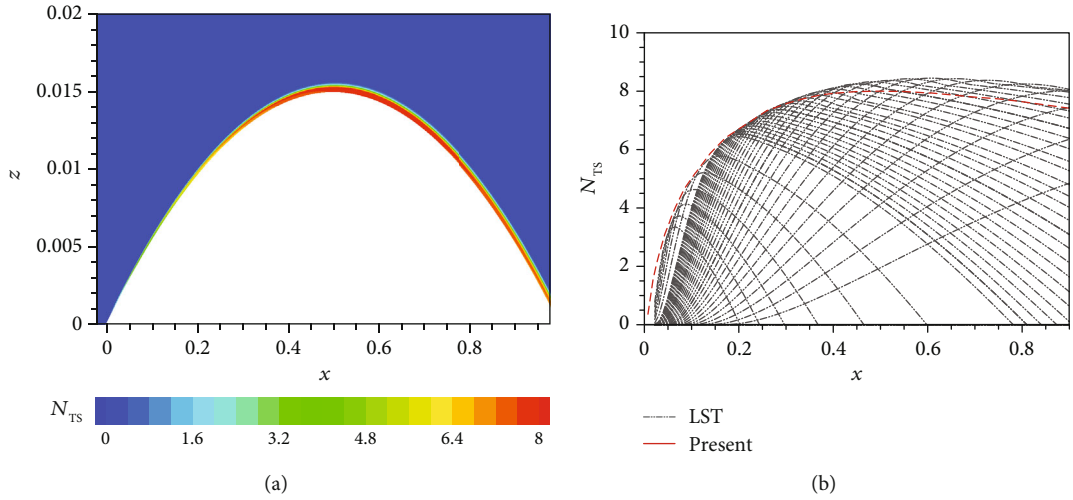

Figure 10: The predicted (a) N_{TS} contour and (b) comparison with standard LST analysis results when angle of attack is 0°.

employed to conduct the mesh sensitive test, and the results are illustrated in Figure 3(a). The Mach number is 2.2 and Reynolds number is 5.6×10^7/m. The near-wall mesh is fine enough so that $y^+(1)$ of the cell next to the wall is smaller than 1.0. It can be seen that as the amount of the grid increases, the results converge gradually, demonstrating the robustness of the new transport equation. Figure 3(b) displays the contour of N_{TS} factor calculated by the present transport equation. Note that the predicted maximum value of N_{TS} factor is extracted from the N_{TS} contour at each streamwise location. With further validations, various freestream conditions were considered. Figure 4 displays the contour of predicted N_{TS} factor and the comparison with the standard LST analysis results under the conditions of $M_\infty = 1.5$ and $\mathrm{Re} = 5.4 \times 10^7$/m. Meanwhile, the Mach number is 2.2 in Figure 5 and 3.0 in Figure 6. Moreover, the unit Reynolds number in Figure 5 is 3.0×10^7/m and 5.6×10^7/m in Figure 6. Although the Mach numbers and Reynolds numbers change, the predicted results of N_{TS} factor seem robust and accurate. When a critical value of N_{TS} factor was set as 10.0, the results in the case with $M_\infty = 3.5$ and $\mathrm{Re} = 5.89 \times 10^7$/m are plotted in Figure 7. Before the threshold value of N_{TS} factor, the development of N_{TS} factor is described accurate and transition occurs near the threshold. Subsequently, in the turbulent region, N_{TS} factor will be quickly dissipated. As a result, the whole process of oblique T-S wave-induced transition is simulated reasonably.

3.2. Validation Test Case 2: Biconvex Laminar Airfoil. Secondly, the 3% thick biconvex airfoil, i.e., the "Airfoil-1" as plotted in Figure 8, is chosen for validations. Note that the coordinates of this classical airfoil are formulated as $z/c = 0.06x/c(1 - x/c)$. The following airfoil cases use the same topology structure of mesh with the flat plate cases. The freestream conditions are set as $M_\infty = 2.0$ and $\mathrm{Re} = 5.4 \times 10^7$/m. When the angle of attack (AoA) is zero, the

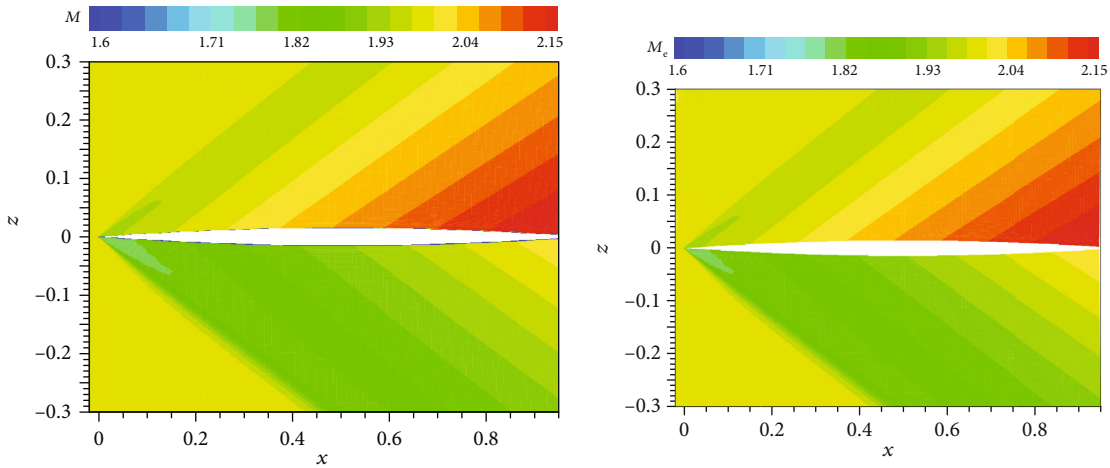

Figure 11: Comparison between (a) local Mach number and (b) predicted M_e with angle of attack of 2°.

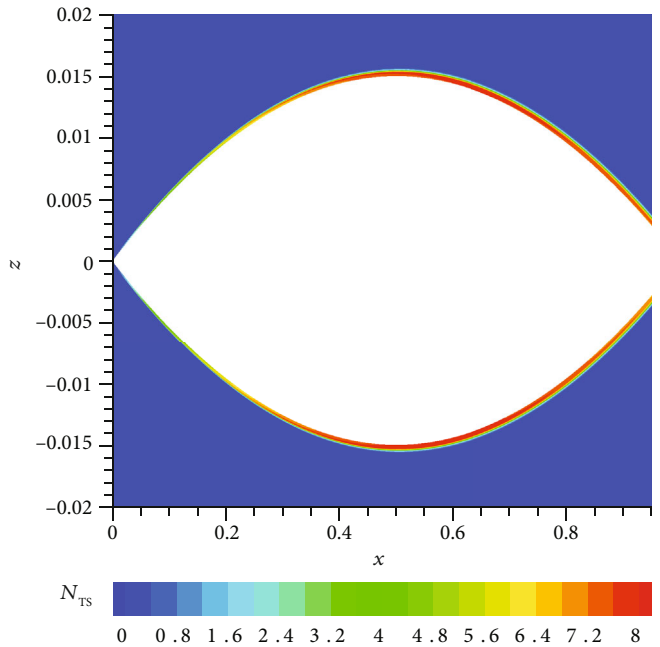

Figure 12: The predicted N_{TS} contour with angle of attack of 2°.

predicted Mach number at the edge of boundary layer is shown in Figure 9, compared with the contour of local Mach number. The predicted value of M_e agrees well with the contour of local Mach number. The calculated N_{TS} contour and the maximum value at each streamwise location are sketched in Figure 10.

When the angle of attack is 2 degrees, Figure 11 demonstrates the predicted Mach number at the edge of boundary layer which is in accord with the value at the outer edge of the boundary layer in the local Mach number contour. The predicted N_{TS} contour is displayed in Figure 12. Furthermore, the extracted data on the upper surface and lower surface are plotted in Figures 13(a) and 13(b), respectively. It can be seen that most of the N_{TS} factor are simulated accurately. It is worth noting that the defects without history effect term gradually appear downstream. This is the main reason of the deviations between the predicted value and the standard LST results in the downstream region. Certainly, even though the nonlocal methods are used, there are still deviations compared with the standard LST analysis data [18]. Consequently, the small deviations predicted here can be accepted.

3.3. Validation Test Case 3: Modified Laminar Airfoil. The third case for validation is the "Airfoil-2" as shown in Figure 8, which has a larger radius of curvature near the leading edge. The freestream Mach number is 1.8 and the unit Reynolds numbers contain $\mathrm{Re} = 3.5 \times 10^7/\mathrm{m}$, $5.4 \times 10^7/\mathrm{m}$, and $8.0 \times 10^7/\mathrm{m}$. The estimated M_e is still in good agreement with the reference data

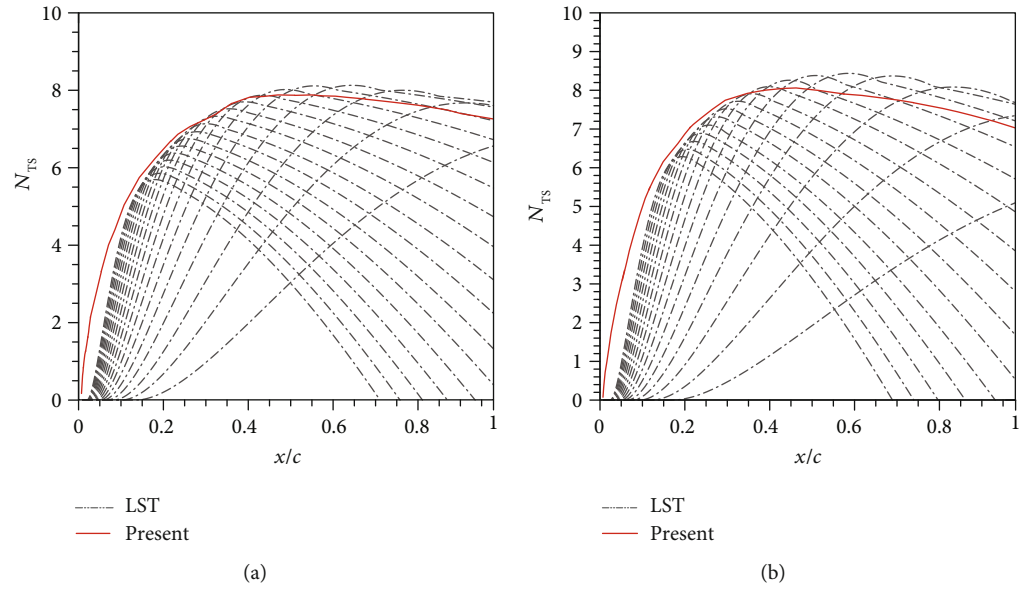

FIGURE 13: The predicted N_{TS} factor on the (a) upper surface and (b) lower surface with angle of attack of 2°.

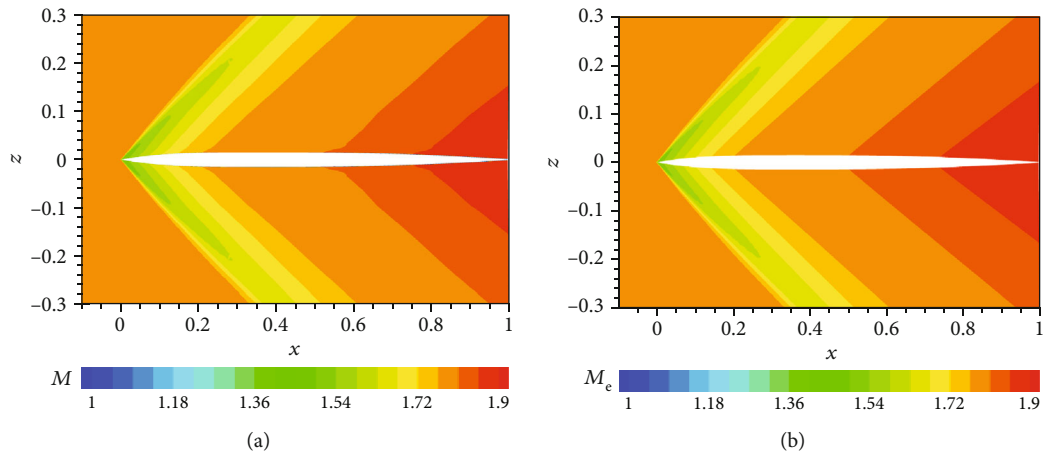

FIGURE 14: Comparison between (a) local Mach number and (b) predicted M_e with Mach number of 1.8.

shown in Figure 14. In addition, Figures 15–17 illustrate the computed N_{TS} factor contour and the comparison with standard LST analysis results. Overall, the present transport equation works well. However, due to the lack of history effect term, there are obvious deviations between the predicted value of N_{TS} and the standard LST results. Therefore, for the computations in moderate or strong favorable pressure gradient flows, it seems quite difficult to compute the average of upstream integrated variables using local variables. This problem will be solved in the future research.

4. Conclusions

In summary, a new amplification factor transport equation for the oblique T-S waves in supersonic flows has been developed based on linear stability analysis results and validated in several typical two-dimensional supersonic flows. The good agreement between the present transport equation and the standard LST analysis results in two-dimensional supersonic airfoils which show that the present transport equation is very promising and encouraging. Obviously, this model has the potential to be extended and applied to predict the oblique T-S waves on three-dimensional wings with sharp leading edge and cones with sharp nose. Moreover, crossflow instability, playing an important role in 3D boundary layers, should be taken into account in the future research.

It should be pointed out that the present model can only simulate the pure oblique T-S waves, which means it cannot predict the airfoils with blunt leading edge. Because there is a subsonic region near the blunt leading edge, the instability mechanism near the leading edge may start from two-dimensional T-S waves to oblique T-S waves. Hence, this complex process cannot be captured using the present model.

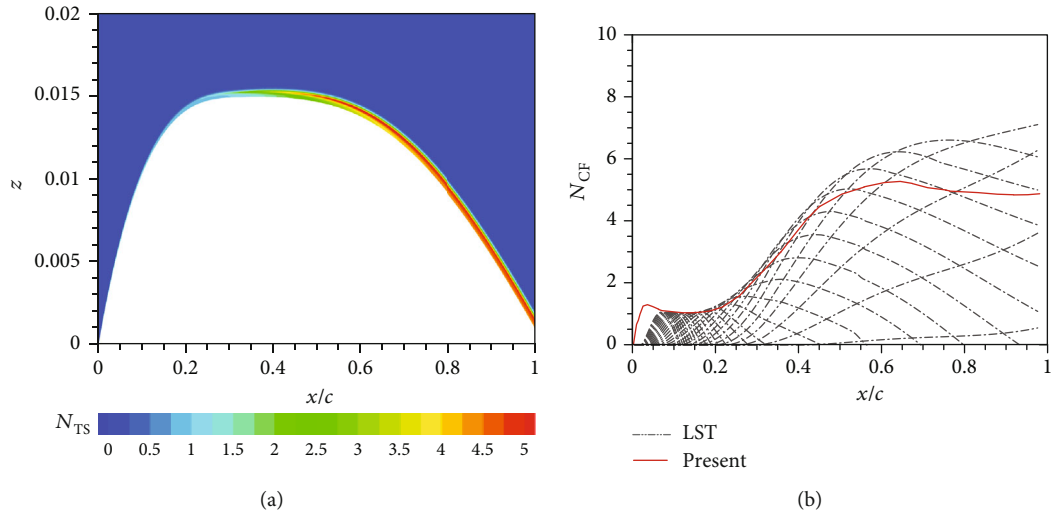

FIGURE 15: The predicted (a) N_{TS} contour and (b) comparison with standard LST analysis results at $Re = 3.5 \times 10^7$/m.

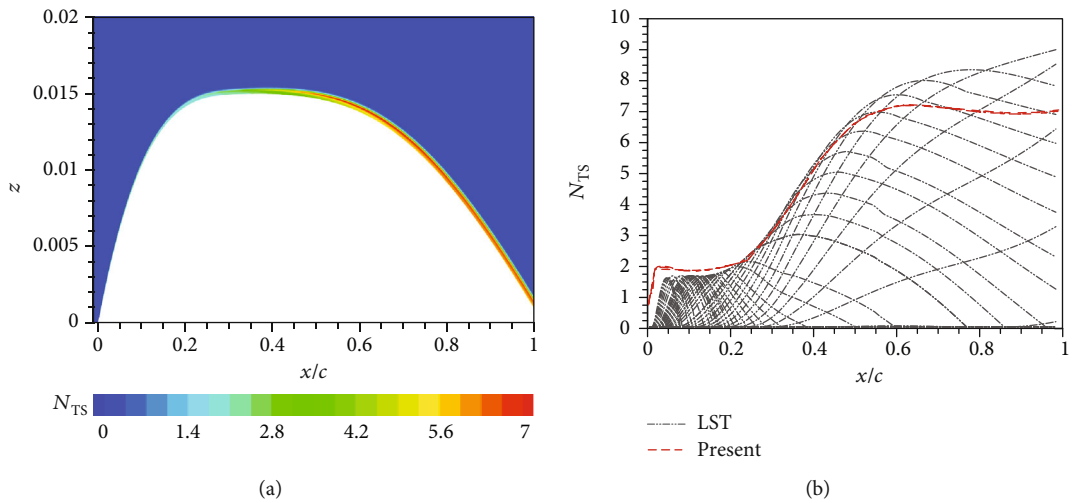

FIGURE 16: The predicted (a) N_{TS} contour and (b) comparison with standard LST analysis results at $Re = 5.4 \times 10^7$/m.

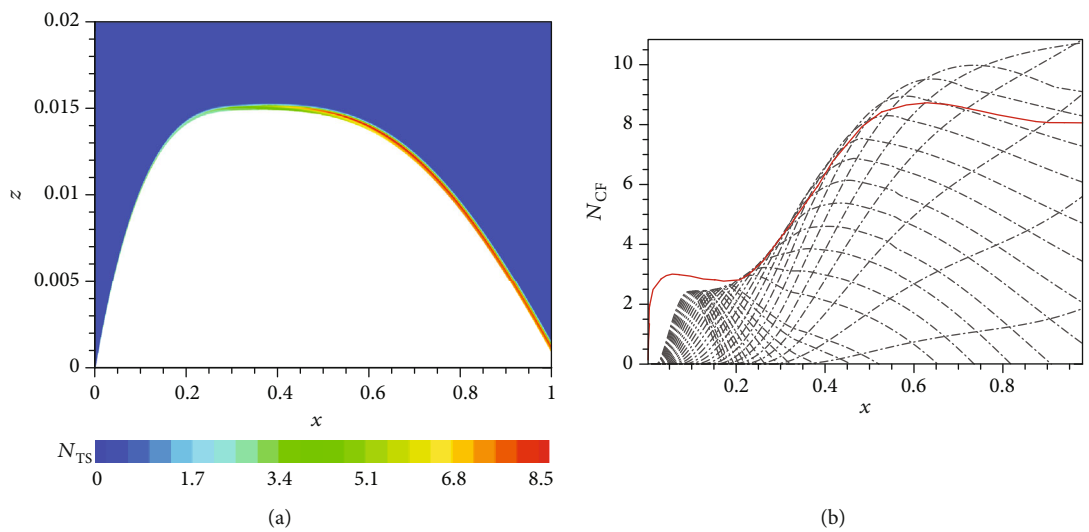

FIGURE 17: The predicted (a) N_{TS} contour and (b) comparison with standard LST analysis results at $Re = 8.0 \times 10^7$/m.

On the whole, although the application scope is limited to supersonic configurations with sharp leading edge, all the formulations established in this model provide a good idea and a reasonable fundamental framework for the modeling of oblique T-S waves in supersonic boundary layers. The extensive validations at various Mach numbers, Reynolds numbers, and angles of attack are all in accord with the standard LST analysis results, which has proven that the present transport equation is constructed reasonably and correctly. As for the history effect term, it should be taken into account by a new transport equation in the next step.

Data Availability

The data used to support the findings of this study are available from the corresponding author upon request.

Conflicts of Interest

The authors declare that there is no conflict of interest regarding the publication of this paper.

Acknowledgments

The authors would like to thank PhD candidates Runjie Song from Department of Mechanics of Tianjin University and Yu Zhang from School of Aeronautics of Northwestern Polytechnical University for their valuable suggestions and discussions. This work is supported by the National Natural Science Foundation for Young Scholar of China (grant numbers 11602199 and 11802245).

References

[1] J. Xu, Z. Fu, J. Bai, Y. Zhang, Z. Duan, and Y. Zhang, "Study of boundary layer transition on supercritical natural laminar flow wing at high Reynolds number through wind tunnel experiment," *Aerospace Science and Technology*, vol. 80, pp. 221–231, 2018.

[2] R. B. Langtry, F. R. Menter, S. R. Likki, Y. B. Suzen, P. G. Huang, and S. Völker, "A correlation-based transition model using local variables part I: model formulation," *Journal of Turbomachinery*, vol. 128, no. 3, pp. 413–422, 2004.

[3] R. B. Langtry, F. R. Menter, S. R. Likki, Y. B. Suzen, P. G. Huang, and S. Völker, "Correlation-based transition model using local variables part II: test cases and industrial applications," *Journal of Turbomachinery*, vol. 128, no. 3, pp. 423–434, 2004.

[4] R. B. Langtry and F. R. Menter, "Correlation-based transition modeling for unstructured parallelized computational fluid dynamics codes," *AIAA Journal*, vol. 47, no. 12, pp. 2894–2906, 2009.

[5] D. K. Walters and J. H. Leylek, "Computational fluid dynamics study of wake-induced transition on a compressor-like flat plate," *Journal of Turbomachinery*, vol. 127, no. 1, pp. 52–63, 2005.

[6] K. D. Walters and D. Cokljat, "A three-equation eddy-viscosity model for Reynolds-averaged Navier-Stokes simulations of transitional flow," *Journal of Fluids Engineering*, vol. 130, no. 12, 2008.

[7] S. Fu and L. Wang, "RANS modeling of high-speed aerodynamic flow transition with consideration of stability theory," *Progress in Aerospace Sciences*, vol. 58, no. 2, pp. 36–59, 2013.

[8] J. Xu, J. Bai, L. Qiao, Y. Zhang, and Z. Fu, "Fully local formulation of a transition closure model for transitional flow simulations," *AIAA Journal*, vol. 54, no. 10, pp. 3015–3023, 2016.

[9] J. Xu, J. Bai, Z. Fu, L. Qiao, Y. Zhang, and J. Xu, "Parallel compatible transition closure model for high-speed transitional flow," *AIAA Journal*, vol. 55, no. 9, pp. 3040–3050, 2017.

[10] J. Xu, J. Bai, L. Qiao, and Y. Zhang, "Development of a computational fluid dynamics compatible mathematical model for boundary layer transitional flows in low-disturbance environment," *Aerospace Science and Technology*, vol. 86, pp. 487–496, 2019.

[11] J. K. Xu, J. Q. Bai, L. Qiao, and Y. Zhang, "Correlation-based transition transport modeling for simulating crossflow instabilities," *Journal of Applied Fluid Mechanics*, vol. 9, no. 5, pp. 2435–2442, 2016.

[12] A. M. O. Smith and N. Gamberoni, "Transition, pressure gradient and stability theory," in *Douglas Aircraft Company Rept. ES-26388*, Douglas Aircraft Company, El Segundo Division, Long Beach, CA, 1956.

[13] J. L. Van Ingen, "A suggested semi-empirical method for the calculation of the boundary layer transition region," in *Technische Hogeschool Delft, Vliegtuigbouwkunde, Rapport VTH-74*, Delft University of Technology, Delft, The Netherlands, 1956.

[14] L. M. Mack, "Transition prediction and linear stability theory," *In AGARD Laminar-Turbulent Transition 22 p (SEE N78-14316 05-34)*, 1977.

[15] M. Drela and M. B. Giles, "Viscous-inviscid analysis of transonic and low Reynolds number airfoils," *AIAA Journal*, vol. 25, no. 10, pp. 1347–1355, 1987.

[16] M. Drela and H. Youngren, *XFOIL 6.9 User Primer*, Massachusetts Inst. of Technology, Cambridge, MA, 2001.

[17] N. Krimmelbein and A. Krumbein, "Automatic transition prediction for three-dimensional configurations with focus on industrial application," *Journal of Aircraft*, vol. 48, no. 6, pp. 1878–1887, 2011.

[18] G. Bégou, H. Deniau, O. Vermeersch, and G. Casalis, "Database approach for laminar-turbulent transition prediction: Navier–Stokes compatible reformulation," *AIAA Journal*, vol. 55, no. 11, pp. 3648–3660, 2017.

[19] L. Pascal, G. Delattre, H. Deniau, G. Bégou, and J. Cliquet, "Implementation of stability-based transition models by means of transport equations," in *AIAA Aviation 2019 Forum*, Dallas, Texas, June 2019.

[20] Y. Shi, R. Gross, C. A. Mader, and J. Martins, "Transition prediction in a RANS solver based on linear stability theory for complex three-dimensional configurations," in *2018 AIAA Aerospace Sciences Meeting*, Kissimmee, Florida, January 2018.

[21] J. G. Coder and M. D. Maughmer, "Computational fluid dynamics compatible transition modeling using an amplification factor transport equation," *AIAA Journal*, vol. 52, no. 11, pp. 2506–2512, 2014.

[22] J. G. Coder, *Enhancement of the amplification factor transport transition modeling framework*, 55th AIAA Aerospace Sciences Meeting, Grapevine, Texas, 2017.

[23] J. G. Coder, *Further development of the amplification factor transport transition model for aerodynamic flows*, AIAA SciTech 2019 Forum, San Diego, California, 2019.

[24] J. Xu, J. Bai, Y. Zhang, and L. Qiao, "Transition study of 3D aerodynamic configures using improved transport equations modeling," *Chinese Journal of Aeronautics*, vol. 29, no. 4, pp. 874–881, 2016.

[25] J. Xu, X. Han, L. Qiao, J. Bai, and Y. Zhang, "Fully local amplification factor transport equation for stationary crossflow instabilities," *AIAA Journal*, vol. 57, no. 7, pp. 2682–2693, 2019.

[26] L. M. Mack, "Boundary-layer linear stability theory," in *Special Course on Stability and Transition of Laminar Flow, AGARD Rept*, vol. 709, 1984.

[27] L. M. Mack, "Linear stability theory and the problem of supersonic boundary-layer transition," *AIAA Journal*, vol. 13, no. 3, pp. 278–289, 1975.

[28] T. Cebeci and J. Cousteix, *Modeling and Computation of Boundary-Layer Flows*, Springer, Berlin Heidelberg New York, 2005.

[29] I. Kroo and P. Sturdza, "Design-oriented aerodynamic analysis for supersonic laminar flow wings," in *41 st AIAA Aerospace Sciences Meeting & Exhibit, Reno, NV.*, 2003.

[30] C. Grabe, S. Nie, and A. Krumbein, "Transition transport modeling for the prediction of crossflow transition," in *34th AIAA applied aerodynamics conference*, 2016.

[31] G. Cheng, R. Nichols, K. Neroorkar, and P. Radhamony, "Validation and assessment of turbulence transition models," in *47th AIAA Aerospace Sciences Meeting including The New Horizons Forum and Aerospace Exposition*, Orlando, Florida, 2009.

[32] J. Coder and M. Maughmer, "A CFD-compatible transition model using an amplification factor transport equation," in *51st AIAA Aerospace Sciences Meeting including the New Horizons Forum and Aerospace Exposition*, 2013.

[33] T. Cebeci and K. Stewartson, "On stability and transition in three-dimensional flows," *AIAA Journal*, vol. 18, no. 4, pp. 398–405, 1980.

[34] S. L. Krist, R. T. Biedron, and C. L. Rumsey, *CFL3D User's Manual (Version 5.0)*, NASA TM-1998-208444, 1998.